Modeling the effects of channel refraction on wave propagation and sediment transport

A comparative study using phase-averaged and phase-resolving models

L.P. Nederstigt

Delft University of Technology

TU Delft

SVASEK HYDRAULICS
COASTAL, HARBOUR AND RIVER CONSULTANTS

Modeling the effects of channel refraction on wave propagation and sediment transport

A comparative study using phase-averaged and phase-resolving models

by

L.P. (Luc) Nederstigt

in partial fulfillment of the requirements for the degree of

Master of Science
Civil Engineering

at Delft University of Technology
to be defended publicly on Tuesday July 22nd 2025 at 13:00

Student number:	4953037	
Project duration:	February, 2025 – July, 2025	
Thesis committee:	Prof. dr. ir. J.A. Álvarez Antolínez,	TU Delft, responsible supervisor
	Prof. dr. ir. A.J.H.M. Reniers,	TU Delft, supervisor
	Dr. ir. F. de Wit,	Svašek Hydraulics, supervisor

Cover: Waves refracted by channel geometry – a visualization of wave behavior in XBeach non-hydrostatic.

Preface

This thesis marks the final step in completing my Master's degree in Civil Engineering at Delft University of Technology. The work presented here was carried out at the Svašek Hydraulics office in Rotterdam and presents the results of my graduation research on the effects of channel refraction on wave propagation and sediment transport.

First of all, I would like to thank my academic supervisors, José Álvarez Antolínez and Ad Reniers, for their critical insights and support during the research. José, I want to thank you for the thoughtful guidance throughout the project, nudging me in the right direction and helping me manage my project effectively. Ad, thank you for your sharp questions and remarks, and the valuable feedback, which often led to new insights (or even more questions).

At Svašek Hydraulics' office, I had the privilege of working alongside experienced engineers. I want to thank all colleagues for the great time I had working with you and all the activities together. I am especially grateful to Floris de Wit for the amazing guidance, your great ideas, and the feedback on my work. Whenever new results came in, you were always at least as curious and enthusiastic as myself, sometimes even more so.

Special thanks go to my girlfriend, family, and friends who supported me during all phases of the project. Your encouragement helped me stay focused and motivated.

Looking back, this project not only improved my understanding of coastal processes and numerical modeling but also shaped my skills in critical thinking and research. I hope that the outcomes of this work contribute to the ongoing efforts in coastal modeling and improving the design of coastal infrastructure.

L.P. Nederstigt
Delft, July 2025

Abstract

Channel refraction, a process in which obliquely incident waves are turned by navigation channel slopes and effectively reflected away from the channel, can significantly influence nearshore hydrodynamics and sediment transport. This thesis investigates how well phase-averaged and phase-resolving numerical models capture these effects. A comparative study was conducted using SWAN-FINEL (phase-averaged) and XBeach non-hydrostatic (phase-resolving). First, model performance in simulating wave transformation was assessed using a physical model of Taman Port. Both models reproduced general wave patterns and showed comparable performance based on the wave measurements. XBeach offered slightly improved accuracy in energetic conditions and on the lee side of the channel. Second, an idealized numerical experiment was used to explore sediment transport differences. Offline sediment transport calculations using an intra-wave and phase-averaged model based on the Meyer-Peter-Müller formulations revealed very similar longshore transport gradients and infilling patterns, but notable differences in cross-shore transport due to the inclusion of wave skewness, asymmetry, and swash-zone processes in XBeach. The findings highlight that while SWAN-FINEL performs well in longshore-dominated systems at low computational cost, phase-resolving models offer added value for short-term cross-shore-dominated settings, albeit at higher computational demand. Model choice should therefore depend on the dominant transport direction and project scope.

Contents

1

Introduction

1.1. Background and Context

As a result of the growth of the global economy and overseas trade between countries and continents, the marine environment has become an important part of our economy. Coasts have always been attractive locations for city expansion for many reasons (Neumann et al., 2015). The maritime industry has seen rapid growth in the last few decades and is expected to keep growing at a yearly rate of 2.4% per year (UNCTAD, 2024). Ports are scattered along the coasts, functioning as hubs for global trade, with increased dredging being necessary to facilitate the growth in the maritime trade and larger ships entering the ports through navigation channels (Yap & Lam, 2013).

Navigation channels are dynamic systems influenced by complex hydrodynamic and sedimentary interactions. They lie in an environment where waves interact with the bathymetry, currents, wind, and ships. One of these interactions that can occur is channel refraction (Zwamborn & Grieve, 1974). Channel refraction is an effect that occurs when waves arrive at a channel at a near-parallel angle. Refraction then causes the wave to turn and effectively reflect over the channel slope. Because the waves don't pass the channel, it creates a sheltered zone inside and on the opposite side of the channel. Channel refraction thus reduces wave energy on one side while increasing wave energy on the refracted side. Channel refraction has been shown to influence wave propagation (Li et al., 2000), and is expected also to have an impact on sediment transport and the morphology of the coastal system.

To address this complexity, numerical models have become essential tools in coastal engineering. They allow researchers and engineers to simulate the behavior of coastal systems by applying mathematical representations of physical processes. Channel refraction is one such process that can be investigated through numerical modeling. However, each model is based on specific assumptions, simplifications, and governing equations, which influence its ability to represent reality accurately. As a result, it is important to understand the foundations of different models, their strengths and limitations, and the uncertainties associated with their predictions.

1.2. Problem Statement and Research Gap

Wave refraction over navigation channels is known to significantly affect the distribution of wave energy (Li et al., 2000; Zwamborn & Grieve, 1974). Svasek Hydraulics (2016) have found that channel refraction could also impact coastal morphology. However, predicting these effects remains a challenge due to the complexity of coastal systems. Processes such as wave transformation, wave–current interaction, sediment transport, and morphological change occur simultaneously and influence one another.

A common way to predict the effect of a channel on the harbor and the surrounding coast is through the use of a numerical model. Phase-averaged spectral wave models are generally the preferred option for a first assessment of the wave conditions at a harbor (Dusseljee et al., 2014). These models are easy to set up and are fast to run. Refraction is often properly represented in these models (the SWAN team, 2024).

Previous studies have investigated wave propagation in a situation with channel refraction with numerical models like SWAN in a case study (Groeneweg et al., 2014; van der Reijden, 2020). Other studies emphasized the comparison of different numerical models (SWASH (Zijlema et al., 2011), SWAN (Booij et al., 1999), and HARES (B. J. O. Eikema et al., 2018)) and found that SWAN underestimates the wave heights inside and on the lee-side of the channel (Adema et al., 2009; Dusseljee et al., 2014; Groeneweg et al., 2014). SWASH performs better in this regard, but at a higher computational cost to achieve a good accuracy (Dusseljee et al., 2014).

While previous research has evaluated how different wave models perform in simulating channel refraction, most of these studies have focused primarily on wave heights and hydrodynamic behavior. However, channel refraction can also have a substantial impact on sediment dynamics and coastal morphology (Svasek Hydraulics, 2016). These processes can be very relevant near harbors, where channel infilling can affect navigability or increase maintenance dredging requirements, and longshore transport gradients can lead to unexpected and unwanted morphological changes in adjacent coastal areas. Failing to accurately predict sediment transport in such settings may result in design inefficiencies, increased maintenance costs, or damage to the coastline.

This underlines the need for a better understanding of the level of modeling detail required to simulate sediment transport patterns near channel refraction. The added value of phase-resolving models over faster, computationally efficient phase-averaged models has not been systematically assessed for this application.

1.3. Scope and Focus

This research focuses on wave propagation, current patterns, and sediment transport in and around engineered navigation channels. It aims to compare the predictive capabilities of a phase-averaged and a phase-resolving numerical model. The following two modeling approaches are employed:

- A phase-averaged model, consisting of the wave model SWAN (Booij et al., 1999) coupled with the flow model FINEL (Svašek Hydraulics, 2020), which simulates wave spectra and depth-averaged current fields without resolving individual wave motions.
- A phase-resolving model, XBeach in non-hydrostatic mode (Smit et al., 2010), which resolves individual wave phases.

The research consists of two parts. First, a comparison of modeled hydrodynamics is made using a physical model case study. This is the same physical model used in earlier studies (Dusseljee et al., 2014; Eikema et al., 2018; Riezebos, 2014). This allows for a validation of the accuracy of the model's wave predictions. Second, an idealized channel configuration is used to compare sediment transport patterns predicted by the two models. The results from this case are not validated with measurements; instead, this case is a numerical experiment focusing on the differences between the two models.

The main emphasis lies in understanding how different modeling approaches capture the effects of channel refraction on wave transformation and sediment transport. Although long-term morphological evolution is not simulated, the results provide insight into how channel refraction may influence coastal erosion and sedimentation.

The sediment transport computations are performed offline, meaning that the model results are post-processed separately to obtain sediment fluxes. This is done to retain control over the transport formulations that are used and to allow for a fair comparison between two very different models.

Because the XBeach non-hydrostatic model requires high spatial and temporal resolution to remain numerically stable, simulations are limited to short timeframes (on the order of one hour). No tidal forcing or morphodynamic feedbacks are included. This ensures that the study remains focused on short-term hydrodynamic behavior induced by channel refraction, while still allowing for reasoned speculation on potential longer-term sediment transport trends.

1.4. Research Questions and Objectives

This research aims to improve the understanding of the hydrodynamic processes associated with wave refraction in engineered navigation channels and their implications for sediment transport. The ultimate goal is to support more informed decisions in the design and maintenance of such channels by evaluating the effectiveness of different numerical modeling approaches.

The first objective is to assess how wave refraction influences wave propagation and sediment transport indicators in and around navigation channels. The second objective is to evaluate the level of modeling detail required to accurately simulate these effects. This is achieved by comparing a phase-averaged and a phase-resolving model, using both a validated physical model case and an idealized numerical experiment. This approach allows for both validation of wave propagation against measurements and controlled comparison of model behavior regarding sediment transport under refractive conditions.

The central research question is:

How does channel refraction influence wave propagation and sediment transport, and what level of modeling detail is required to accurately predict its effects?

To answer this, the following sub-questions are investigated:

RQ1. How does channel refraction impact wave propagation and sediment dynamics?

RQ2. What are the strengths and limitations of phase-averaged models (e.g., SWAN-FINEL) in representing channel refraction and its influence on sediment transport?

RQ3. To what extent does a phase-resolving model (e.g., XBeach non-hydrostatic) improve the accuracy of wave propagation and sediment transport predictions under channel refraction conditions?

RQ4. What insights can be derived from the model comparison to guide the design of navigation channels?

1.5. Structure of the Thesis

This thesis is structured as follows.

Chapter 2 provides a literature review covering the theoretical background on ocean waves, wave propagation, wave refraction (including channel refraction), and sediment transport processes. It also discusses relevant modeling techniques.

Chapter 3 describes the numerical models used in this study: SWAN, XBeach in non-hydrostatic mode, and FINEL2D. The chapter includes their governing equations, physical assumptions, and implementation of relevant processes.

Chapter 4 presents the setup, calibration, and validation of the hydrodynamic model results using a physical model experiment (the Taman case). This includes sensitivity analysis and comparison to observations.

Chapter 5 focuses on sediment transport, using an idealized channel case to compare the performance of SWAN-FINEL and XBeach-nh. Model setups, sediment transport formulations, and the resulting hydrodynamic and transport predictions are discussed.

Chapter 6 discusses the key findings, limitations, and implications for future modeling work.

Finally, Chapter 7 summarizes the main conclusions and provides recommendations for the application of numerical models in the design and assessment of navigation channels affected by wave refraction.

2

Background and literature review

This chapter provides the background information and a review of the state-of-the-art regarding the subjects of channel refraction, wave propagation, and sediment modeling. The chapter begins with a review of ocean waves and their statistical representation using spectral theory. Next, the principles of wave propagation in both deep and shallow water are introduced, with a focus on refraction. The behavior of waves in coastal zones is further examined by discussing hydrodynamic processes such as skewness, asymmetry, and wave-induced mass transport. Special attention is then given to channel refraction and its impact on wave propagation. The final sections of this chapter cover sediment transport theory, from bed shear stress and initiation of motion to transport formulations used in numerical modeling. Together, these components form the foundation for the modeling approaches and analyses presented in later chapters.

2.1. Ocean waves

Wind-generated ocean waves are a very complex and random process. A single wave record contains waves with many different wave heights (H) and wave periods (T). To simplify this complex process, the surface elevation of the ocean is described as a statistical process.

2.1.1. Definition of a wave

There is an important difference between surface elevation and waves. Surface elevation is the instantaneous elevation of the sea surface. This is something that can be directly observed and is something that is measured in, for example, a wave record, where the surface elevation is measured in one location during a certain time. A wave can be defined as the surface elevation profile between two downward (or upward) zero-crossings of the mean surface elevation (Goda, 1986; Holthuijsen, 2007).

The most often used metric for the wave height of an ocean wave record is the *significant wave height* ($H_{1/3}$). The highest 1/3 of waves within a wave record were seen as the ”most significant” (Sverdrup & Munk, 1947), and the mean of those highest 1/3 of waves is the significant wave height.

2.1.2. The wave spectrum

Because of their random character, wind-generated ocean waves can be described as a statistical process. Treating ocean waves in this way makes the computation of wave propagation processes (for example, in a spectral model like SWAN (Booij et al., 1999)) very efficient. A wave record - an observation of the sea surface elevation - is seen as the realization of a stochastic process (Barber & Ursell, 1948). Any wave record can then be reproduced as a Fourier series of harmonic wave components (Holthuijsen, 2007):

$$\eta(t) = \sum_{i=1}^{N} a_i cos(2\pi f_i t + \alpha_i) \tag{2.1}$$

Where a_i is the amplitude and α_i is the phase of each frequency. From any wave record, the amplitude and phase of each frequency are obtained using a Fourier analysis.

A wave spectrum is usually not presented using the amplitude itself $E\{\underline{a_i}\}$, but with the variance of the sea surface elevation $E\left\{\frac{1}{2}\underline{a_i}^2\right\}$. Taking the limit as $\Delta f \to 0$ yields the equation for the variance density spectrum $E(f)$:

$$E(f) = \lim_{\Delta f \to 0} \frac{1}{\Delta f} E\left\{\frac{1}{2}\underline{a}^2\right\} \tag{2.2}$$

The unit of spectral density is m^2/Hz. An example of a variance density spectrum is visualized in Figure 2.1.

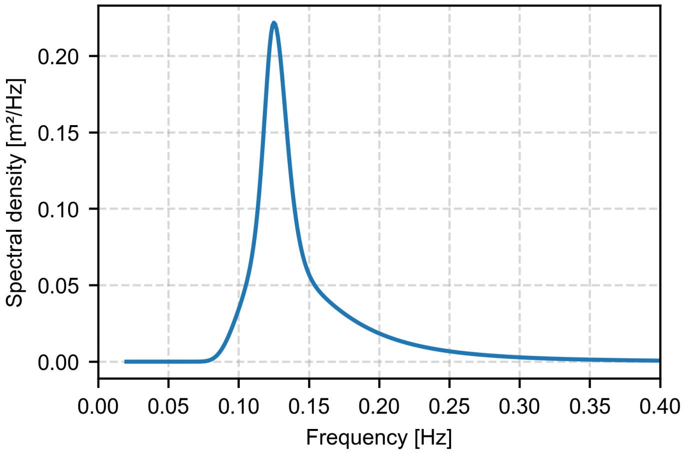

Figure 2.1: Example variance density spectrum (standard JONSWAP)

From the wave spectrum, certain statistics can be derived. They are usually expressed in terms of an n-th order spectral moment, which is defined as:

$$m_n = \int_0^\infty f^n E(f) df \tag{2.3}$$

The zeroth-order spectral moment can also be obtained with the variance of surface elevation $m_0 = Var(\eta^2)$. The significant wave height can be calculated using m_0, and some often-used wave periods to describe a wave spectrum can also be obtained using spectral moments:

$$H_s \approx H_{m0} = 4\sqrt{m_0}$$

$$T_{m01} = \frac{m_0}{m_1},\ T_{m02} = \sqrt{\frac{m_0}{m_2}},\ T_{m-1,0} = \frac{m_{-1}}{m_0}$$

2.2. Linear wave theory

This section introduces the theoretical background of wave propagation based on linear wave theory. It describes the underlying assumptions and governing equations, and the dispersion relationship that links wave frequency, wavelength, and depth. Subsequently, the section discusses how waves evolve in coastal waters with processes such as shoaling, refraction, and diffraction.

2.2.1. Governing equations and assumptions

Linear wave theory forms the basis for describing the characteristics of surface gravity waves. It relies mainly on two equations and some boundary conditions. Freely propagating harmonic waves are the solution to these equations when they are linearized; this means that the waves don't interact with each other. An important assumption for linear wave theory is that the amplitude of waves is small compared to the wavelength and water depth ($ak \ll 2\pi$ and $a \ll d$). This is known as the *small-amplitude* assumption, or the Airy wave theory (Airy, 1845; Holthuijsen, 2007).

As a basis for linear wave theory, water is considered an ideal fluid, and some assumptions are made (Holthuijsen, 2007).

- Water is incompressible, has a constant density, and has no viscosity.
- The body of water is continuous.
- Water particles may not leave the surface or penetrate the bottom.
- The water is subjected to only one external force: gravity.

The two balance equations that govern linear wave theory are the mass balance equation and the momentum balance equation. Waves are assumed to be infinitely long along the crest, meaning there is no variation in the y-direction, and the lateral boundaries don't have to be solved. At the water surface, the kinematic boundary condition is that water particles can not leave the surface. At the bottom, the kinematic boundary condition is that water particles can not penetrate the bottom (Holthuijsen, 2007).

2.2.2. Harmonic waves

When these equations are combined with boundary conditions at the water surface and bottom, one of the solutions that can be found is the description of a propagating harmonic wave in Equation (2.4), where the surface elevation η is described as a function of space and time.

$$\eta\,(x,t) = a\sin(\omega t - kx) \tag{2.4}$$

The particle velocities of harmonic waves in space and time can also be described. The velocities in the y-direction are zero because the wave propagates in the x-direction. The water particles in a harmonic wave follow an orbital motion, which can be described with the following equations:

$$u_x = \hat{u}_x \sin(\omega t - kx), \quad \text{with} \quad \hat{u}_x = \omega a \frac{\cosh[k(d+z)]}{\sinh(kd)} \tag{2.5}$$

$$u_z = \hat{u}_z \cos(\omega t - kx), \quad \text{with} \quad \hat{u}_z = \omega a \frac{\sinh[k(d+z)]}{\sinh(kd)} \tag{2.6}$$

When the equation for the surface elevation harmonic wave (Equation (2.4)) is combined with a zero-pressure boundary condition at the surface, the dispersion relationship is obtained. This relates the angular frequency ω and wave number k.

$$\omega^2 = gk\tanh kd \tag{2.7}$$

From the dispersion relationship follows the phase speed of a harmonic wave, using $c = L/T = \omega/k$, see Equation (2.8). The depth dependency of the phase speed will be important for refraction later.

$$c = \frac{g}{\omega}\tanh kd = \sqrt{\frac{g}{k}\tanh kd} \tag{2.8}$$

2.3. Wave propagation in coastal waters

Waves behave differently when they enter coastal waters compared to how they behave in the open ocean. The waves are affected by the change in water depth; it influences them in multiple ways. This section describes three key wave processes in coastal waters.

2.3.1. Shoaling

Shoaling is one of the most important processes in coastal waters (e.g. Eckart, 1952), and it occurs when the waves are affected by a decreasing depth; they begin interacting with the bottom. According to Equation (2.8), the phase speed decreases when the depth decreases. The group velocity initially increases, and later decreases as well. As the waves propagate into shallower water, their phase speed becomes less dependent on their frequency and more dependent on the water depth.

2.3.2. Refraction

Another process that can occur in coastal waters is wave refraction. Wave refraction is best explained with an example: a harmonic wave approaching a coast at an angle. In this case, the wave will change direction because there is a depth gradient along the crest of the wave. And, according to Equation (2.8), a wave travels faster in deeper water than in shallow water. In practice, this means that a wave will turn towards an area with a lower propagation speed - an area with shallower water. This example is visualized in Figure 2.2.

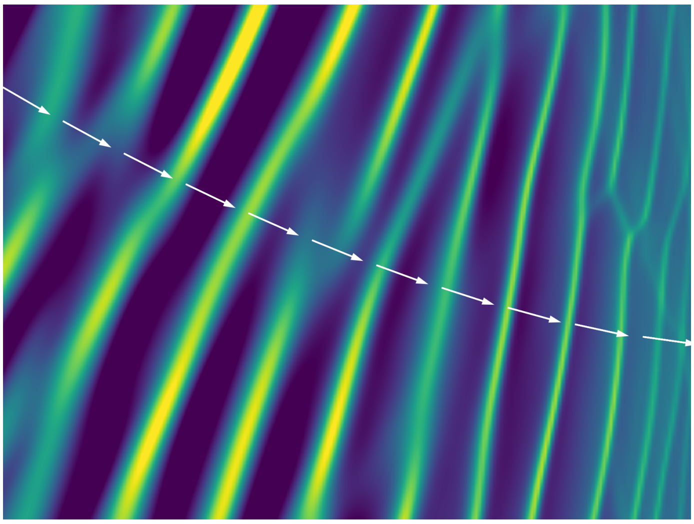

Figure 2.2: Refraction occurring when waves approach a straight coast at an angle.

Wave refraction plays an important role in shaping wave propagation patterns, especially around regions with large relative variations in bathymetry, such as navigation channels, which is discussed in Section 2.6.

2.3.3. Diffraction

Diffraction is present when waves travel around an obstacle, like a breakwater, in waters with constant depth (which means that this process is different from refraction, which is a depth-dependent process). The waves will bend around the obstacle into the so-called shadow zone. Wave energy is transferred along the crest of the wave, which means that wave energy is also present in the shadow zone, see Figure 2.3.

2.4. Coastal Hydrodynamics

As waves propagate into coastal waters, their interaction with the seabed and nonlinear processes causes transformations in wave shape and flow structure. In this section, two important features of wave transformation are discussed, followed by an overview of the resulting wave-induced mass flux and return currents.

2.4.1. Wave asymmetry and skewness

As waves propagate from deep to shallow water, they undergo nonlinear transformations, gradually deviating from the sinusoidal shapes in deeper water as described by linear wave theory. As waves reach shallower water, the shoaling process is typically (apart from changes in wave height) characterized by

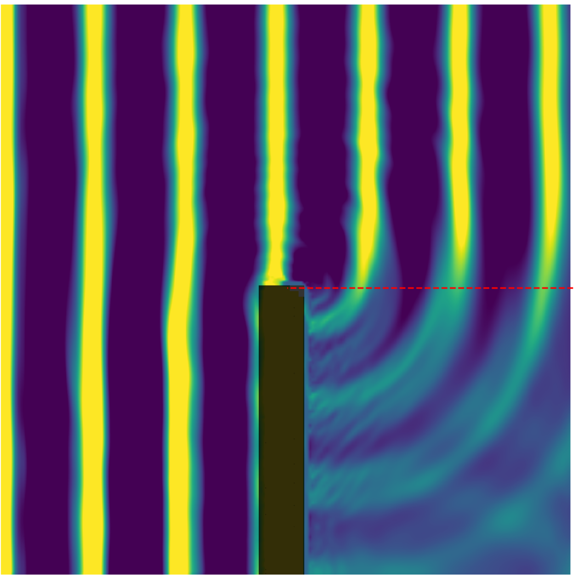

Figure 2.3: Diffraction around a breakwater

skewness and asymmetry.

Skewness refers to the horizontal asymmetry of the orbital velocity and surface elevation. As waves shoal, the wave crest becomes sharper and the trough flatter, resulting in a time-averaged velocity profile with enhanced onshore velocities during the crest phase. This effect can be described using higher-order wave theories, such as Stokes theory, where a phase-locked harmonic component is introduced that increases the peaking of the wave crest. The skewness is often quantified statistically as the normalized third moment of the surface elevation, $\langle \eta^3 \rangle / \sigma^3$, where a positive value indicates more peaked wave crests.

Asymmetry refers to the pitched-forward shape of the wave. In shallow water, this occurs because the crest propagates over a relatively higher water depth than the trough. The crest, therefore, travels faster than the trough, and the result is a steep wave front and a more gradual rear face, giving the wave a sawtooth-like appearance.

Waves traveling into coastal waters first become more skewed, where, closer to the surf zone, phase shifting of the higher harmonics causes an increase in asymmetry. The waves will gradually steepen until they break (Svendsen et al., 1979).

2.4.2. Wave-induced mass flux

As orbital motion becomes increasingly asymmetric with decreasing depth, net mass transport in the direction of wave propagation develops. This phenomenon, known as Stokes drift, results from the non-closed nature of water particle orbits. It gives rise to an onshore-directed wave-induced mass flux above the wave trough level. To conserve mass, a compensating offshore-directed return flow (commonly referred to as the undertow) develops below the wave trough (e.g. Longuet-Higgins, 1953; Phillips, 1977).

This wave-induced mass transport becomes particularly significant in the surf zone, where waves break and generate additional turbulence. Here, the formation of a surface roller further increases the onshore mass flux (Svendsen, 1984). These effects modify the cross-shore velocity structure and influence nearshore circulation patterns.

The depth-integrated wave-induced mass flux per unit width in the direction of wave propagation can be expressed as

$$q = \int_{-h}^{\eta} \rho u \, dz, \tag{2.9}$$

Where ρ is the water density, u the horizontal orbital velocity in the direction of wave propagation, h the local water depth, and η the instantaneous free surface elevation.

In the surf zone, the total wave-driven mass flux q_{drift} is typically modeled as a combination of non-breaking and roller-induced components:

$$q_{\text{drift}} = q_{\text{non-breaking}} + q_{\text{roller}} = \frac{E}{c} + \frac{\alpha E_r}{c}, \tag{2.10}$$

where E is the wave energy, E_r is the roller energy, c is the phase speed of the wave, and α is an empirical factor typically in the range of 0.22 to 2.0 (Nairn et al., 1990; Roelvink & Stive, 1989).

To conserve mass, the onshore mass flux above the trough must be balanced by a return current below the trough. This offshore-directed return velocity (undertow) is given as:

$$U_{\text{below trough}} = -\frac{q_{\text{drift},x}}{\rho h} = -\frac{q_{\text{drift}} \cos \phi}{\rho h}, \tag{2.11}$$

where $q_{\text{drift},x}$ is the cross-shore component of the mass flux, ϕ is the wave angle, and h the local depth.

2.5. Fundamentals of refraction

Refraction was already briefly introduced in Section 2.3 but will be discussed in further detail in this section. First, Snell's law is introduced, and then the effect of refraction on amplitude is explained.

2.5.1. Wave rays and Snell's law

The main principle for refraction is that a wave changes its direction because of a gradient in water depth along the crest, which causes a gradient of phase speed along the crest according to Equation (2.8). The corresponding rate of turning of the waves can be derived by looking at wave crests as iso-phase-lines and their orthogonals as wave rays (Arthur et al., 1952; Munk & Arthur, 1952). The rate of turning of the wave can then be derived to be:

$$\frac{d\phi}{dn} = -\frac{1}{c}\frac{\partial c}{\partial m}$$

Where m is the direction of the wave crest, and n is the direction of the wave ray.

This expression can be simplified using Snell's law, which is valid for a coast with parallel depth contours. All derivatives in the y-direction are now zero, and after some rewriting, the rate of turning can be expressed as:

$$\frac{\mathrm{d}(\sin \phi / c)}{\mathrm{d}n} = 0 \quad \text{or} \quad \sin \phi / c = \text{constant} \tag{2.12}$$

2.5.2. Effect on wave amplitude

This formula for the rate of turning can be useful when the deep water angle is known, and the angle of the waves in any other place around the coast is required. Refraction not only affects wave direction but also affects wave amplitude. The influence of wave refraction on amplitude can be derived by looking at the wave energy entering through planes at different locations along the wave rays (Dorrestein, 1960). The amplitude at one point can be determined using the group velocities c_g in the different locations and the width between two wave rays b:

$$a_2 = \sqrt{\frac{c_{g,1}}{c_{g,2}}} \sqrt{\frac{b_1}{b_2}} a_1 \tag{2.13}$$

When one boundary is taken in deep water and index 2 is dropped, the refraction coefficient $K_{ref} = \sqrt{b'/b}$ is obtained (Dorrestein, 1960), where b' is the width between two wave rays in deep water.

2.6. Channel refraction

A special case for refraction is channel refraction - when waves refract over the slope of a (dredged) channel. When the waves enter the channel at a certain *critical angle*, the waves do not cross the channel. Instead, the waves are focused on the slope of the channel, creating a shadow zone inside and on the other side of the channel.

2.6.1. Critical wave angle

Channel refraction was first treated and investigated by Zwamborn and Grieve (1974). In this paper, it was described how diffraction and refraction can have a large effect on the wave hydrodynamics in a harbor and that they are the most important wave transformations for a harbor entrance design. They found that waves that approach a deep channel at a critical angle (a mean angle relative to the channel axis of approximately 25°) will cause a concentration of wave energy on the channel slope, which may lead to serious problems. This concentration of wave energy could be explained through refraction theory.

Yu et al. (2000) performed a physical model study to assess the combined effects of the refraction and diffraction of waves through a breakwater gap and a navigation channel. In this paper, a combined refraction-diffraction coefficient $K_d = H_d/H_i$ was used, where H_d is the combined refraction-diffraction wave height, and H_i is the incident wave height. They found that the shape of the frequency and direction spectrum has an influence on K_d, but the shape of the direction spectrum has a larger effect than the shape of the frequency spectrum. They warn that the combined effect of refraction and diffraction in deep navigation channels may cause an uneven distribution of waves over the channel.

As was found by the previously mentioned studies, whether the waves cross the channel or are refracted and concentrate on the channel slope is determined by the so-called critical angle ϕ_c. The critical wave angle can be derived using Snell's law (Equation (2.12)):

$$\frac{\sin\phi_c}{c_1} = \frac{\sin 90^\circ}{c_2}$$

Here, c_1 is the incident phase speed of the wave, and c_2 is the phase speed of the wave inside the channel. Rewriting this equation gives an expression for the critical wave angle ϕ_c (Dusseljee et al., 2014; Riezebos, 2014; van der Reijden, 2020):

$$\phi_c = \arccos\frac{c_1}{c_2} \tag{2.14}$$

The critical angle theoretically ranges from 0° for no change in propagation speed up to 90° for a very large change in propagation speed. In reality, however, channels are not infinitely deep, which means that in practice, the upper limit of the critical angle is around 50° (Riezebos, 2014). The critical angle is plotted in Figure 2.4 as a function of the dimensionless wave period outside the channel ($T_0\sqrt{g/d_1}$) and depth ratio inside and outside the channel (d_2/d_1)

$$\phi_c = \arccos\frac{\tanh k_1 d_1}{\tanh k_2 d_2}$$

, where kd can be approximated with the method by Eckart (1952) and is a function of the dimensionless period and depth ratio. Note that, in this theoretical expression of ϕ_c, it is not dependent on channel slope or channel width.

When the incident angle ϕ_i is larger than the critical wave angle ($\phi_i > \phi_c$), the wave will be able to cross the channel. As shown in Figure 2.5, the waves do still feel the effect of the slopes and refract, but they don't remain focused on the channel slope. When the incident angle is smaller than the critical wave angle ($\phi_i < \phi_c$), the waves will not cross the channel. Instead, the waves will focus on the channel, and some waves could reflect into the channel (Riezebos, 2014).

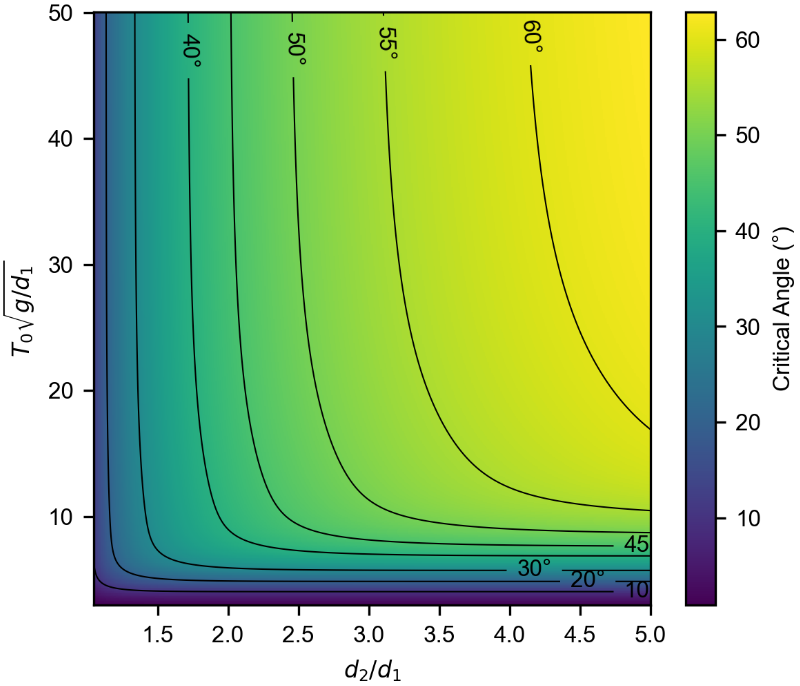

Figure 2.4: The critical angle ϕ_c for channel refraction as a function of dimensionless wave period outside the channel and depth ratio inside and outside the channel (inspired by Dusseljee et al. (2014)).

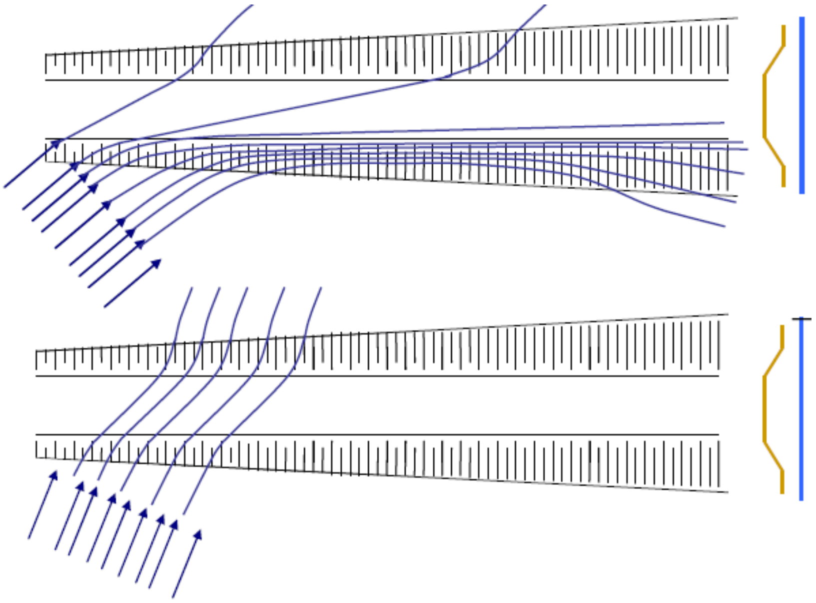

Figure 2.5: Waves crossing the channel and waves focusing on the channel slope (Guzmán Mardones, 2011)

2.6.2. Effect of spectral spreading and bathymetry

Because the critical angle depends on the phase speed of the waves (Equation (2.8)), the critical angle depends on the depth of the channel, the depth of the ambient bathymetry, and the wave number of the waves k, which is related to the wave length or frequency of the waves. This also means that the situation can become quite complex when the incident waves are defined by a wave spectrum with different frequencies. Because of the dependence of ϕ_c on the frequency of the wave, shorter waves within the spectrum might be able to cross the spectrum, while the longer waves within the spectrum will be refracted.

Directional spreading in a wave spectrum will also contribute to more complexity in the situation. Because waves in a wind-generated wind field generally come from different directions (Pierson, 1955), some incident waves might have an incident angle larger than ϕ_c and cross the channel, whilst others might have an incident angle smaller than ϕ_c and refract over the channel slope.

The bathymetry surrounding the channel and inside the channel also changes the way that waves refract over the channel slopes. If the bathymetry outside or inside the channel varies over the length, ϕ_c also varies over the length. This will cause some waves to cross the channel again while others won't. Previous research has also found that the channel slope and shape can affect how waves refract and reflect over a channel (P. A. Madsen et al., 2006; Magne et al., 2007; Misra et al., 2009).

2.6.3. Modeling of channel refraction

One of the first instances where a numerical model was applied to a channel refraction case was performed by Li et al. (2000). The case that was studied was the physical model by Yu et al. (2000). The case was investigated using a numerical model developed by Li et al. (1999), which was based on the Boussinesq equations. The numerical results were compared with the laboratory results. The results from the numerical tests agreed with the laboratory tests; a navigation channel has a large effect on wave propagation. One of the findings was that the critical angle (the angle at which waves don't cross the channel anymore but are refracted on the channel slope) is dependent on wave propagation distance and channel length. Also, wave directional spreading was found to have a smoothing effect on wave concentration on the channel slope.

An intercomparison between a SWAN and SWASH model and laboratory experiments for a navigation channel was made by Dusseljee et al. (2014). SWAN (Booij et al., 1999) is a phase-averaged model, whereas SWASH (Zijlema et al., 2011) is a phase-resolving model. The influence of the channel on wave propagation was investigated and compared between the two methods. The paper also includes a modeling guideline. The results show that SWAN underestimates the wave conditions in the channel and at the lee side due to the neglect of wave tunneling. SWASH does include these effects and performs better than SWAN, but is computationally more expensive.

The laboratory experiment conditions discussed in Dusseljee et al. (2014) were remodeled using the model HARES by Eikema et al. (2018). HARES is a stationary phase-resolving 2D model based on the mild-slope equation. The wave heights between the results using HARES and the results from SWAN and SWASH (Dusseljee et al., 2014) were compared. HARES performed the best, with much less computational cost compared to SWASH and about the same as SWAN.

The underestimation of the wave penetration in SWAN that was found by Dusseljee et al. (2014) was further investigated in the paper by Groeneweg et al. (2015). Because of nonlinear interactions, the direction spectrum is changed when waves refract over the channel slope. This causes more waves to have a larger angle than the critical angle compared to what SWAN predicts, causing more waves to pass the channel. SWAN simulations were compared to simulations with the Boussinesq-type model TRITON, which performed better but at a computational cost such that it was unrealistic to be used in a real project.

2.7. Sediment transport fundamentals

Sediment transport plays a key role in shaping coasts and influencing the navigability and stability of engineered structures such as harbors and navigational channels. The movement of sediment is driven by a complex interaction of hydrodynamic forces generated by waves, currents, and tides, and is further influenced by local bathymetry and sediment characteristics. Understanding sediment dynamics is essential in coastal engineering to be able to predict the long-term response of the system to an intervention that the engineer has designed.

Some important processes that govern sediment transport and need to be taken into account when modeling sediment transport are (Roelvink & Reniers, 2011):

- Sediment transport predominantly follows the direction of the near-bed current.
- An increase in current velocity results in a non-linear amplification of sediment transport, typically exceeding a first-order relationship.

- On sloping beds, gravitational effects tend to redirect sediment transport downhill.
- Orbital wave motions enhance sediment resuspension, thereby increasing the overall transport magnitude.
- In shallow water, wave asymmetry introduces a net sediment transport component that can be aligned with or opposed to the direction of wave propagation.

2.7.1. Bed shear stress

The bed shear stress τ_b represents the shear force per unit area exerted by the fluid on the seabed and is an important factor for sediment transport modeling. It is induced by the interaction between the moving water and the bed surface and reflects the intensity of near-bed hydrodynamic forcing. Accurately estimating the bed shear stress is essential for predicting sediment entrainment and for input into transport formulations. A general expression for bed shear stress is:

$$\tau_b = \rho u_* |u_*| \tag{2.15}$$

where u_* is the shear velocity and ρ is the fluid density (e.g. Bosboom & Stive, 2023; Pokrajac et al., 2006). Since shear velocity scales with the flow velocity, the bed shear stress is proportional to the square of the flow velocity; $\tau_b \propto u^2$.

In sediment transport modeling, the bed shear stresses induced by waves and currents are typically treated separately, where the total bed shear stress is assumed to consist of a mean current component and an oscillatory wave component. This is particularly done in cases where only wave-averaged data are available (as is the case in phase-averaged models). The bed shear stresses due to currents, waves, and combined waves and currents are discussed below.

Currents

The bed shear stress due to currents can be related to the depth-averaged current velocity U and the drag coefficient C_D through (e.g. Soulsby, 1997):

$$\tau_c = \rho C_D U^2 \tag{2.16}$$

The drag coefficient C_D can be related to the Chézy coefficient C and Manning's coefficient n through:

$$C_D = \frac{g}{C^2} = \frac{gn^2}{h^{1/3}}$$

Waves

The bed-shear stress that is induced by waves can be seen as an oscillatory motion with an amplitude τ_w. The shear stress can be computed with the orbital velocity amplitude of the waves at the bed U_w and with a wave friction factor f_w (e.g. Soulsby, 1997), this is assuming a smooth bed (no ripples):

$$\tau_w = \frac{1}{2}\rho f_w U_w^2 \tag{2.17}$$

An often used formulation for the bed friction factor f_w is the one by Swart (1974) which uses the relative roughness r:

$$r = \frac{A}{k_s}$$

Where $A = U_w/\omega$ is the orbital excursion and $k_s \approx 2.5 D_{50}$ the Nikuradse sand grain roughness. Then, the skin friction due to waves is given by (Swart, 1974):

$$f_{wr} = \begin{cases} 0.3 & \text{for } r \leq 1.57 \\ 0.00251 \exp\left(5.21 r^{-0.19}\right) & \text{for } r > 1.57 \end{cases} \tag{2.18}$$

Combined waves and currents

When waves and currents are both present, they cannot simply be added together to obtain a total shear stress due to the non-linear interactions between wave and current boundary layers. Many different models have been proposed describing this interaction (Davies et al., 1988; Fredsøe, 1984; Grant & Madsen, 1979; Huynh-Thanh & Temperville, 1991). A common way to express the bed shear stresses during the wave-current cycle is with the mean τ_m and maximum τ_{max} bed shear stress during the wave cycle. In Soulsby et al. (1993), a general algebraic approximation for these models is derived with a high ($\pm 5\%$) accuracy.

In the research by Soulsby (1995), a method for computing τ_m and τ_{max} was developed based on data. This reduces the algebraic formulations to the following relatively simple expressions (Soulsby, 1997):

$$\tau_m = \tau_c \left[1 + 1.2 \left(\frac{\tau_w}{\tau_c + \tau_w}\right)^{3.2}\right] \tag{2.19}$$

$$\tau_{max} = \left[(\tau_m + \tau_w \cos\phi)^2 + (\tau_w \sin\phi)^2\right]^{1/2} \tag{2.20}$$

Where τ_c and τ_w are the bed shear-stresses due to waves and currents, if they were to occur separately (Equations (2.16) and (2.17)).

2.7.2. Initiation of Motion

The initiation of motion of a sediment particle marks the moment when the particle is dislodged from the bed and begins to move under the influence of water motion. This process is governed by a balance between the *driving forces*, primarily the drag force exerted by the flow, and the *resisting forces*, mainly gravity and friction between grains. When the bed shear stress τ_b exceeds a critical threshold $\tau_{b,cr}$, the grain is mobilized and entrained into the flow.

To generalize the initiation of motion across different sediment sizes and flow conditions, the *Shields parameter* θ is often used (Shields, 1936). This dimensionless parameter expresses the ratio of bed shear stress to the submerged weight of the particle, and is defined as:

$$\theta = \frac{\tau_b}{(\rho_s - \rho) g D} \tag{2.21}$$

where ρ_s is the sediment density, D is the grain diameter, and g is gravitational acceleration. The *critical Shields parameter* θ_c corresponds to the threshold at which sediment motion begins and is typically determined empirically. Its value depends on the dimensionless grain size and flow regime, with typical values ranging from 0.03 to 0.06 for natural sands in steady flows.

The value of the critical Shields parameter θ_c is not constant, but depends on several factors, most notably the grain Reynolds number, which characterizes the relative importance of viscous and inertial forces acting on a sediment grain. This dependency is often visualized using the Shields diagram (Figure 2.6), which shows θ_c as a function of the dimensionless grain size or particle Reynolds number.

For very fine particles (e.g., silts and clays), cohesive forces between grains become significant, leading to higher critical values. For coarse sediments (e.g., gravels), the critical Shields parameter increases again due to increasing flow turbulence and grain protrusion effects. In the range of medium to coarse sands typically encountered in coastal environments, θ_c tends to remain relatively stable, with values around 0.03 to 0.06.

Various empirical formulations exist to estimate θ_c more precisely based on grain size and flow conditions. A commonly used algebraic expression for non-cohesive sediments under steady flow is proposed by Soulsby and Whitehouse (1997):

$$\theta_c = \frac{0.30}{1 + 1.2 D_*} + 0.055 \left[1 - \exp\left(-0.020 D_*\right)\right] \tag{2.22}$$

Where D_* is the dimensionless grain size, defined as:

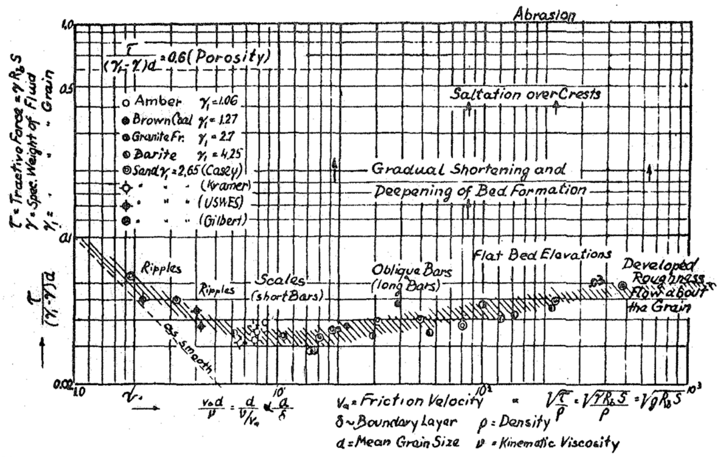

Figure 2.6: Shields diagram (Shields, 1936)

$$D_* = D_{50}\left(\frac{(s-1)g}{\nu^2}\right)^{1/3} \tag{2.23}$$

with $s = \rho_s/\rho$ the relative density, ν the kinematic viscosity of water, and D_{50} the median grain diameter of the sediment. For medium, non-cohesive sand typically found in coastal environments, the critical Shields parameter θ_c is commonly taken as 0.047.

2.7.3. Sediment transport modeling

Once sediment particles are mobilized, their subsequent transport depends on the prevailing hydrodynamic conditions. Sediment transport modeling aims to predict the rate and direction of sediment movement as a function of water flow characteristics, sediment properties, and bed morphology. Accurate modeling of sediment transport is essential for understanding coastal morphodynamics, assessing erosion and deposition patterns, and designing sustainable engineering interventions.

Sediment transport is typically divided into two primary modes: *bed load transport* and *suspended load transport*. Bed load transport refers to the movement of particles along the bed (Figure 2.7a), while suspended load transport involves particles being lifted into the water column and carried by the flow turbulence (Figure 2.7b). The relative importance of these modes depends on factors such as grain size, flow strength, and turbulence intensity. Some sediment transport formulations consider the sum of bed and suspended load transport, called *total load* sediment transport.

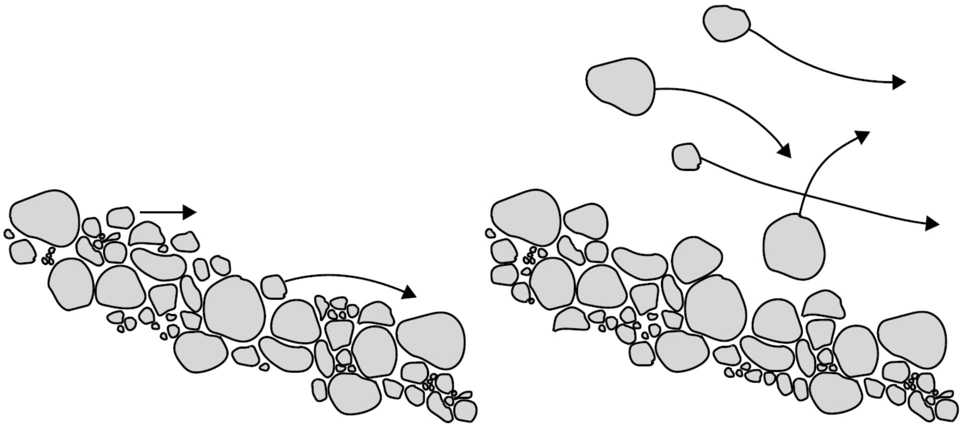

(a) Bed load **(b)** Suspended load

Figure 2.7: Visualization of the different transport modes (Bosboom & Stive, 2023)

The prediction of sediment transport rates relies on a range of approaches, from empirical formulations based on laboratory and field observations to more complex process-based models that resolve the underlying physical mechanisms. In coastal environments, where waves and currents interact, the transport processes are particularly dynamic and variable over space and time, requiring careful representation in numerical models.

Many different formulations exist for bed load and total load sediment transport. Some of these formulations are discussed in the subsections below. These formulations are based on different principles, and they model different sediment modes (bed load, total load, suspended load, or a combination of them). An important remark to make here is that in comparisons that were made between different formulations for sediment transport (Bayram et al., 2001; Breusers, 1983), large differences are found in the results that these formulations give. This underlines the importance of calibration of the transport model.

2.7.4. Bed load transport

As discussed in Section 2.7.3, bed load transport occurs within a thin layer near the bed, where grain-grain interactions are dominant. The initiation of sediment motion is typically governed by the condition that the bed shear stress exceeds a critical threshold. It is generally assumed that bed load transport responds instantaneously to the hydrodynamic forcing, i.e., the applied bed shear stresses (e.g. Bosboom & Stive, 2023).

To quantify the initiation of motion, the bed shear stress is commonly expressed using the dimensionless Shields parameter (Equation (2.21)). In nearshore environments, where both waves and currents influence sediment dynamics, their combined effect must be accounted for in the evaluation of the Shields parameter. This can be achieved either through a time-averaged representation of wave-current interaction or by resolving the instantaneous (intra-wave) variations in bed shear stress.

A dimensionless expression for *instantaneous* bed load transport under waves and currents is the following:

$$\Phi_b(t) = \frac{S_b(t)}{\sqrt{(s-1)gD_{50}}} \tag{2.24}$$

Where S_b is the volume of bed load transport per unit time and width. The denominator represents the specific underwater weight of the sand grains.

A general form of bed load transport is the following (Roelvink & Reniers, 2011):

$$S_b \sim \sqrt{\Delta g D_{50}^3}\,\theta^{b/2}(m\theta - n\theta_{cr})^{c/2}\left(1 - \alpha\frac{\partial z_b}{\partial s}\right) \tag{2.25}$$

This general formulation of bed load transport contains all processes that can determine the transport rate. It contains the shields parameter and the critical shields parameter. It also includes bed slope effects and a bed ripple efficiency factor.

Accordingly, the instantaneous (or intra-wave) bed load transport can be expressed as a function of the instantaneous dimensionless bed shear stress (Shield's parameter) and the critical bed shear stress:

$$\Phi(t) = f(\theta(t), \theta_c) \tag{2.26}$$

Time-averaging the sediment flux can then be done in two ways. First, the time-average is taken of the whole function:

$$\langle\Phi(t)\rangle = \langle f(\theta(t), \theta_c)\rangle \tag{2.27}$$

Or the time average (or wave-average) of the shear stress $\theta(t)$ can be used:

$$\langle \Phi(t) \rangle = f(\langle \theta(t) \rangle, \theta_c) \tag{2.28}$$

A phase-resolving model like XBeach non-hydrostatic can employ an intra-wave sediment transport model with the form of Equation (2.27), whereas a phase-averaged model such as SWAN-FINEL uses wave-averaged transport models with the form of Equation (2.28) because it doesn't contain intra-wave information. These two methods will give different results.

2.8. Cross-shore sediment transport

Wave-driven sediment transport is most dominant in the cross-shore direction and can be very complex because of the many different processes that play important roles here. It can bring sediment both offshore and onshore. Some important processes which affect cross-shore sediment transport are:

- Undertow
- Streaming
- Breaking-induced turbulence
- Short-wave skewness and asymmetry
- Bound and free long waves

2.8.1. Velocity decomposition

Bowen (1980) discussed the importance of the combination of an oscillatory motion and a mean flow, skewed waves, or long waves. He decomposed the flow velocity u into a mean flow part and a symmetrical orbital velocity $u = U_0 + U_1$. His work forms the basis for many wave-related sediment transport models used today.

In the study by Roelvink and Stive (1989), the flow velocity u is decomposed into three parts (Bosboom & Stive, 2023); a time averaged mean-flow component $\overline{u}$, an oscillatory component at the wave-group scale u_{lo}, and an oscillatory motion at the short-wave scale u_{hi}. When it is assumed that sediment transport is proportional to the third power of the velocity, Roelvink and Stive (1989) found that the most important velocity moments for the cross-shore sediment transport are:

$$\langle u|u|^2 \rangle = 3\langle \overline{u}|u_s|^2 \rangle + \langle u_s|u_s|^2 \rangle + 3\langle u_L|u_s|^2 \rangle \tag{2.29}$$

The first term on the right-hand side explains the sediment transport stirred by the short waves $|u_{hi}|^2$, and transported by the mean current $\overline{u}$. The second term is related to transport by short-wave skewness u_{hi} (again stirred up by the short waves $|u_{hi}|^2$). The third term is related to the interaction between the long-wave velocity and the short-wave velocity variance.

2.8.2. Skewness, asymmetry, and long waves

The transport mechanisms introduced by velocity decomposition can now be further understood by examining the roles of wave skewness, asymmetry, and long-wave interactions on cross-shore sediment transport. Wave skewness arises due to higher harmonics that are generated during shoaling, which are in phase with the wave that is generating them. These higher harmonics in the same phase create waves with higher peaks and flatter troughs (Stokes, 1847). When the second harmonic is shifted in phase, an asymmetric wave with a sawtooth-like shape is the result. A skewed wave will result in transport in the direction of the wave, because $S \propto u^3$, amplifying the peaks and reducing the troughs. An asymmetric wave does not affect the third velocity moment when it is wave-averaged. These effects are shown in Figure 2.8.

The third term is associated with the correlation between the slowly varying short-wave velocity variance and the long-wave forced by the wave group. Outside the surfzone, a negative correlation is observed; the trough of the long wave (offshore velocity) is found under the larger amplitude waves in the group, resulting in a net offshore-directed transport. This effect is visualized in Figure 2.9. Inside the surf zone, when the bound long waves become free long waves, the correlation between the short-wave velocity variance and the long-wave elevation changes to positive, and the net transport is onshore.

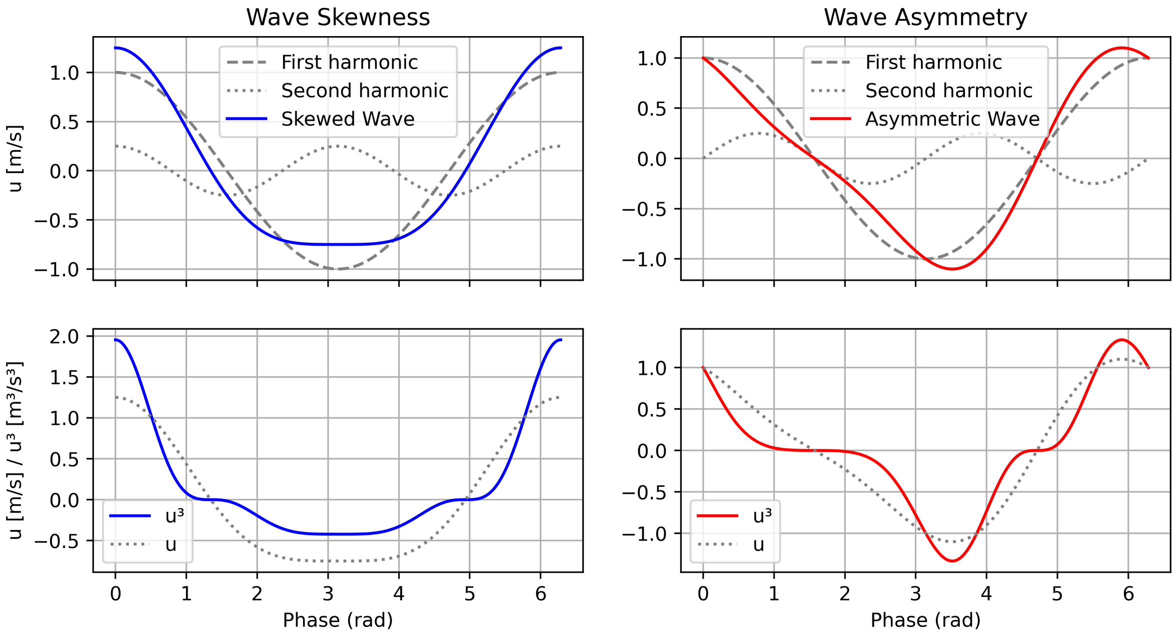

Figure 2.8: Wave skewness and asymmetry and its effect on the third velocity moment.

Many studies have found that long waves can be important to sediment transport (e.g. Bowen, 1980; Carter et al., 1973; Roelvink & Stive, 1989).

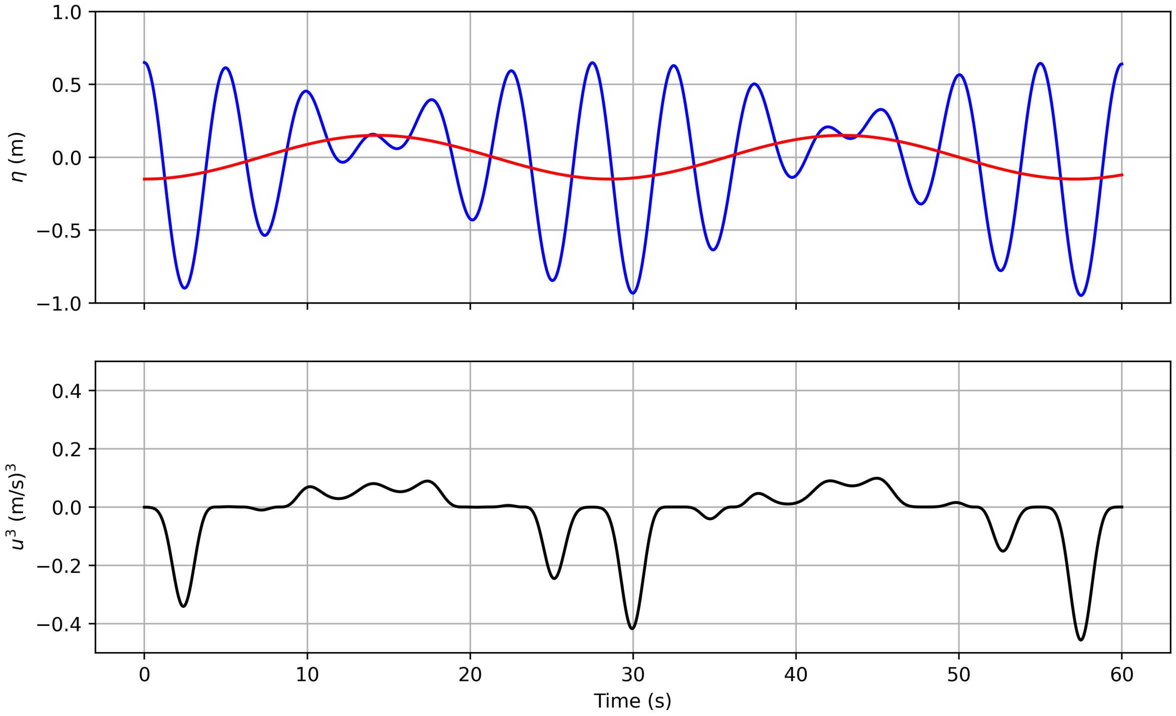

Figure 2.9: Effect of bound long waves on flow velocity. In this example, the third-order velocity moment will result in a net offshore transport.

2.9. Sediment transport formulations

This section reviews sediment transport formulations used in both intra-wave and wave-averaged numerical models, with a focus on their theoretical basis.

2.9.1. Meyer-Peter-Müller (1948) and variations

One of the earliest bed load transport formulations was developed by Meyer-Peter and Müller (1948). Their formulation for sediment transport was originally developed for rivers with a steady flow. The formulation is based on the shear stress exceeding a critical shear stress, which induces the initiation of motion. A general formulation for bed load transport based on the Shields stress is:

$$\Phi_b = \begin{cases} m\theta^P(\theta - \theta_c)^n & \text{for } \theta \geq \theta_c \\ 0 & \text{for } \theta < \theta_c \end{cases} \tag{2.30}$$

A large amount of research has been done on the constants m, n, and P in the formulation. Meyer-Peter and Müller (1948) were the first to look into this formulation, and they performed tests in a flume with coarse sand and low Shields stresses. They obtained values of $m = 8$ and $n = 1.5$. Results from different studies on the Shields-based transport formula are shown in Table 2.1 (Amoudry & Souza, 2011).

Study	m	n	P
Meyer-Peter and Müller, 1948	8	1.5	0
Wilson, 1966	12	1.5	0
Fernandez Luque and Van Beek, 1976	5.7	0	1.5
Ribberink, 1998	11	0	1.65
Soulsby and Damgaard, 2005	12	1	0.5

Table 2.1: Results from studies of Shields-based bed load transport formulations

The values for m vary the most, but there appears to be a consensus that $n + P \approx 1.5$. This means that bed load transport is proportional to the flow velocity to the third power - $S \propto u^3$.

Ribberink (1998) performed an extensive study on datasets of bed-load transport and validation of a Meyer-Peter-Müller based transport model. He investigated steady flows, oscillatory flows, and oscillatory flows with superimposed currents separately. For this study, oscillatory flow with a superimposed current is the most relevant due to the combined wave-current action. He investigated experiments performed in an Oscillatory Water Tunnel with sediment with a $D_{50} = 0.21$ and θ =0.20 to 1.10. Following his analysis, he proposes the following formulation for bed load transport in an oscillatory flow with a superimposed current:

$$\left\langle \vec{\Phi}_b(t) \right\rangle = m \left\langle \left(\left| \vec{\theta'}(t) \right| - \theta_c \right)^n \cdot \frac{\vec{\theta'}(t)}{\left| \vec{\theta'}(t) \right|} \right\rangle \tag{2.31}$$

with

$$|\theta(t)| = \sqrt{\theta_x(t)^2 + \theta_y(t)^2}, \quad m = 11,\ n = 1.65 \tag{2.32}$$

2.9.2. Soulsby (1997)

The book by Soulsby (1997) provides a sediment transport formulation for combined currents and waves. The formulation is based on the transport model by Meyer-Peter and Müller (1948) and is derived in the paper by Soulsby and Damgaard (2005).

A simplified approach to bed shear stress can be taken by assuming that the bed shear stress is the sum of a mean bed shear stress and a sinusoidally varying bed shear stress due to waves (O. S. Madsen, 1991; Soulsby & Damgaard, 2005):

$$\vec{\tau_0}(t) = \vec{\tau_m} + \vec{\tau_w} \cos \omega t \tag{2.33}$$

Where $\vec{\tau_0}(t)$ is the instantaneous bed shear stress, $\vec{\tau_m}$ is the mean current component of the bed shear stress, and $\vec{\tau_w}$ is the amplitude of the oscillatory component of the bed shear stress (wave-induced).

Soulsby and Damgaard (2005) propose an expression for bed load transport in vector form based on the formulation by Meyer-Peter and Müller (1948):

$$\vec{\Phi} = A_2 \theta^{1/2} \left(\theta - \theta_{cr}\right) \frac{\vec{\theta}}{\theta} \tag{2.34}$$

Where A_2 is an empirical constant for which Soulsby and Damgaard (2005) suggested $A_2 = 12$. $\vec{\theta}$ is the vector Shields parameter, and $\theta = |\vec{\theta}|$ is the magnitude of the Shields parameter. The time-averaged dimensionless transport rate is then obtained by taking the integral of the vectorized bed load transport over a wave cycle:

$$\langle \vec{\Phi} \rangle = \frac{A_2}{2\pi} \int_0^{2\pi} \theta^{1/2} (\theta - \theta_{cr}) \frac{\vec{\theta}}{\theta} d(\omega t) \tag{2.35}$$

This integral can be evaluated numerically, but Soulsby and Damgaard (2005) derived analytical expressions for this integral, making them less computationally demanding. There is an expression for a current-dominated situation and a wave-dominated situation, but they can be combined into a few expressions (Soulsby & Damgaard, 2005):

$$\Phi_{x1} = A_2 \theta_m^{1/2} (\theta_m - \theta_{cr}) \tag{2.36}$$

$$\Phi_{x2} = A_2 (0.9534 + 0.1907 \cos 2\phi) \theta_w^{1/2} \theta_m \tag{2.37}$$

$$\Phi_x = \max\left(\Phi_{x1}, \Phi_{x2}\right) \tag{2.38}$$

$$\Phi_y = \frac{A_2 (0.1907 \theta_m \theta_w^2 \sin 2\phi)}{\theta_w^{3/2} + (3/2)\theta_m^{3/2}} \tag{2.39}$$

$$\text{subject to:} \quad \Phi_x = \Phi_y = 0 \quad \text{if} \quad \theta_{\text{max}} \leq \theta_{\text{cr}} \tag{2.40}$$

$$\text{where:} \quad \theta_{\text{max}} = \left[\left(\theta_m + \theta_w \cos\phi\right)^2 + \left(\theta_w \sin\phi\right)^2 \right]^{1/2} \tag{2.41}$$

Where:

- θ_m is the Shields stress due to the mean current. Under currents and waves combined, the mean shear stress is higher than under currents alone (θ_c), see Section 2.7.1.
- θ_w is the Shields' stress *amplitude* due to waves.
- ϕ is the angle between the current and the waves.
- Φ_x is the dimensionless bed load transport in the current direction.
- Φ_y is the dimensionless bed load transport in the direction perpendicular to the current.

In general, the analytical solutions lie very close to the full solutions obtained by evaluating the integral. Only at times where both θ_w and θ_m are very close to the threshold θ_{cr}, can the analytical solution be a bit further off from the full solution (Soulsby & Damgaard, 2005).

3

Numerical Models

This study evaluates the performance of two numerical modeling approaches: SWAN-FINEL and XBeach in non-hydrostatic mode. The models' capability in predicting wave propagation, flows, and sediment transport patterns is compared in a situation with a navigation channel undergoing channel refraction.

SWAN-FINEL combines the phase-averaged wave model SWAN (Booij et al., 1999) with the depth-averaged flow model FINEL2D (Svašek Hydraulics, 2020). FINEL-SWAN is a general phase-averaged wave and flow model, comparable with often used Delft3D-Wave-Flow (Deltares, 2025a). Phase-averaged models do not resolve individual wave phases; instead, they represent waves in phase-averaged values. This makes them efficient and practical for simulating large-scale wave processes but limits their accuracy in phase-dependent phenomena such as wave diffraction (Adytia et al., 2012).

In contrast, XBeach non-hydrostatic (Smit et al., 2010) is a phase-resolving model that resolves individual waves. This improves the model's ability to accurately capture complex wave processes. However, resolving short-wave phases requires finer temporal and spatial grids, resulting in higher computational costs compared to phase-averaged models.

This chapter provides an overview of each of the three models used in this study: SWAN, FINEL, and XBeach non-hydrostatic. For each model, the governing equations, relevant physical processes, and specific implementation details are described.

3.1. SWAN

SWAN (Simulating WAves Nearshore) is a spectral numerical wave model used for coastal applications. It is used to compute random wind-generated short-crested waves in shallow coastal waters (Booij et al., 1999). Most of the information in the following section is obtained from SWAN's technical documentation (the SWAN team, 2024).

3.1.1. Governing equations

SWAN describes the wave field using the definition of a wave spectrum $E(\sigma,\theta)$ discussed in Section 2.1.2. All information about how wave energy is distributed over the different frequencies and directions is stored in this spectrum. The action density $N = E/\sigma$ is often used by spectral models because the action density is conserved when an ambient current is present (the SWAN team, 2024). The rate of change of action density N is described using the spectral balance equation (Holthuijsen, 2007; Komen et al., 1994; Mei, 1983):

$$\frac{\partial N}{\partial t} + \nabla_{\vec{x}} \cdot [(\vec{c}_g + \vec{u})N] + \frac{\partial c_\sigma N}{\partial \sigma} + \frac{\partial c_\theta N}{\partial \theta} = \frac{S_{\text{tot}}}{\sigma} \tag{3.1}$$

This equation contains shoaling, refraction, and shifting of frequencies due to bottom changes and currents. S_{tot} on the right-hand side contains all source and sink terms that generate and dissipate wave energy.

3.1.2. Sources and sinks

Six processes contribute to the total energy S_{tot} (the SWAN team, 2024):

$$S_{tot} = S_{in} + S_{nl3} + S_{nl4} + S_{ds,w} + S_{ds,b} + S_{ds,br} \tag{3.2}$$

Wave growth by wind S_{in} is implemented with a resonance mechanism (Phillips, 1957) and a feedback mechanism (Miles, 1957). The resonance component is linear, whereas the feedback component is exponential:

$$S_{in} = A + BE(\sigma, \theta)$$

where A and B depend on the frequency and direction of the waves.

There are three energy dissipation terms in the equation for all sink/source terms (Equation (3.2)): white capping $S_{ds,w}$, bottom friction $S_{ds,b}$, and depth-induced breaking $S_{ds,br}$. White capping is implemented based on the model by Hasselmann (1974). In this model, white capping is controlled mostly by wave steepness. For bottom friction, many different models have been developed (the SWAN team, 2024). The general expression for bottom friction is:

$$S_{ds,b} = -C_b \frac{\sigma^2}{g^2 \sinh^2 kd} E(\sigma, \theta)$$

In SWAN, three different options are implemented for modeling bottom friction, which are the models developed by Collins (1972), Hasselmann et al. (1973), and O. S. Madsen et al. (1988). Wave breaking in SWAN is implemented through a spectral version (Eldeberky & Battjes, 1995) of the wave-breaking model by Battjes and Janssen (1978). The expression for this sink term is:

$$S_{ds,br}(\sigma, \theta) = \frac{D_{tot}}{E_{tot}} E(\sigma, \theta)$$

The last two terms, S_{nl3} and S_{nl4}, are terms controlled by triad wave interactions and quadruplet wave interactions, which are both represented in SWAN (the SWAN team, 2024).

3.1.3. Implementation of refraction

Refraction is part of the spectral action balance equation (Equation (3.1)), which forms the basis for SWAN. When all non-conservative sink and source terms are ignored, an energy balance that contains *shoaling* and *refraction* is obtained:

$$\frac{dE}{dt} = -\left(\nabla_{\vec{x}} \cdot \vec{c_g} + \frac{\partial c_\theta}{\partial \theta} \right) E \tag{3.3}$$

where

$$\frac{d\vec{x}}{dt} = \vec{c_g}, \quad \frac{d\theta}{dt} = c_\theta \tag{3.4}$$

To accurately integrate Equation (3.3), the rate at which the energy changes along a characteristic is important. This is related to a relaxation time τ, a typical time scale for wave energy transport to reach a steady state again. The numerical accuracy is dependent on the time step, grid size, and directional bin size (the SWAN team, 2024), which are all denoted as ΔT. To ensure accurate numerical integration, Δ should be lower than the relaxation time τ. This condition resembles the Lipschitz criterion (Smolarkiewicz & Pudykiewicz, 1992; the SWAN team, 2024) and reads:

$$\left| \nabla \cdot \vec{c_g} + \frac{\partial c_\theta}{\partial \theta} \right| \Delta T < 1 \tag{3.5}$$

In practice, this means that when gradients in the rate of turning and group velocity are larger, the associated steps should be smaller to obtain good accuracy. In shallow water, variations in bathymetry are more impactful on the wave characteristics, meaning that the grid size and time steps should be smaller than in oceanic water, where very large grid sizes (10 - 50 km) usually suffice.

3.2. FINEL2D

FINEL2D is a depth-averaged hydrodynamic model developed by Svasek Hydraulics (Dam et al., 2018) and it is based on the Finite Element Method (FEM). It solves the shallow water equations and is designed to simulate flow in rivers, estuaries, lakes, and coastal areas. The model uses an unstructured triangular mesh, allowing flexible spatial resolution and detailed schematization of complex geometries such as tidal channels, harbour basins, and shorelines, without requiring nested grids. FINEL2D can be coupled to SWAN to account for waves.

3.2.1. Grid

Typical for models based on the Finite Element Method is that they use a triangular mesh rather than a rectangular one; this is also the case in FINEL2D. A triangular grid can be created using computer routines. The resolution of the triangular mesh can vary over the domain, ensuring higher resolution in more important areas.

3.2.2. Governing equations

The governing equations for the model are the depth-averaged shallow water equations, very similar to XBeach (Equations (3.16) to (3.18)). They differ in that the equations in FINEL2D don't contain a non-hydrostatic pressure term. The equations are given by (Dam et al., 2018):

$$\frac{\partial h}{\partial t} + \frac{\partial UH}{\partial x} + \frac{\partial VH}{\partial y} = 0 \tag{3.6}$$

$$\frac{\partial HU}{\partial t} + \frac{\partial HU^2}{\partial x} + \frac{\partial HUV}{\partial y} - fHV + gH\frac{\partial h}{\partial x} - \frac{1}{\rho}\tau_{x,b} + \frac{1}{\rho}\tau_{x,w} + \frac{1}{\rho}\tau_{x,r} = 0 \tag{3.7}$$

$$\frac{\partial HV}{\partial t} + \frac{\partial HUV}{\partial x} + \frac{\partial HV^2}{\partial y} + fHU + gH\frac{\partial h}{\partial y} - \frac{1}{\rho}\tau_{y,b} + \frac{1}{\rho}\tau_{y,w} + \frac{1}{\rho}\tau_{y,r} = 0 \tag{3.8}$$

Where f is a Coriolis coefficient, τ_w the wind shear stress, and τ_r the radiation stress.

The shallow water equations are solved with the discontinuous Galerkin method (T. Hughes, 1987). For the full numerical implementation of the shallow water equations, see the technical manual of FINEL (Dam et al., 2018).

3.2.3. Stresses

An option in FINEL is to account for wind shear stresses, requiring a wind speed, direction, and drag factor. The bottom roughness on the flow is assessed through bottom friction. The bed shear stress is computed as:

$$\frac{1}{\rho}\tau_{x,b} = -u\frac{g\sqrt{u^2+v^2}}{C^2H} \tag{3.9}$$

$$\frac{1}{\rho}\tau_{y,b} = -v\frac{g\sqrt{u^2+v^2}}{C^2H} \tag{3.10}$$

Where C is the Chézy coefficient. FINEL can also accept a bottom roughness of Nikuradse or Manning. The shear stresses due to waves can be computed using the orbital velocities of the waves U_w according to the method by Soulsby (1997):

$$\tau_w = \frac{1}{2}\rho f_w U_w^2 \tag{3.11}$$

With

$$f_w = \exp\left(5.213\left(\frac{U_w}{k_s}\right)^{-0194} - 5.977\right) \tag{3.12}$$

3.2.4. Sediment transport

FINEL2D also has a sediment transport module for bed load and suspended load transport. The formulations for sediment flux present in FINEL version 7.29 are given in Table 3.1 below.

Formulation	Transport mode
Bijker, 1971	Bed / Bed + Suspended
Engelund and Hansen, 1967	Total
Meyer-Peter and Müller, 1948	Bed
Van Rhee, 2007	Suspended
Bailard, 1981	Bed + Suspended
van Rijn, 1984	Bed + Suspended
Soulsby - van Rijn	Bed + Suspended load

Table 3.1: Transport flux formulations in FINEL 7.29

3.2.5. Hydrodynamics

Roller contribution and Stokes drift both result in onshore mass flux in the top part of the water column (see Section 2.4). To compensate for this, an offshore-directed return flow exists in the lower part of the water column. This compensation can be applied in FINEL version 8.0 to account for near-bed wave-induced currents. The mass flux contribution due to Stokes and wave roller is computed with the wave energy. Then, the additional flow compensation (offshore directed) due to Stokes and wave roller is computed with:

$$U_{stw} = \frac{E}{ch} \tag{3.13}$$

$$U_{rr} = \frac{2E_r}{ch} \tag{3.14}$$

The velocities with the compensation for roller and mass flux are added to the flow velocities computed by the shallow water equations and can be included in the output.

Note that in the SWE in FINEL (Equations (3.6) to (3.8)) the velocities and bed shear stresses don't contain mass flux compensation. Undertow induced through mass flux is simply computed as stated in Equations (3.13) and (3.14) above and added to the velocity computed in the SWE. In some other models, like XBeach (surfbeat), the bed shear stresses in the SWE are computed with the Eulerian flows with mass flux compensation included (Roelvink et al., 2009).

3.2.6. Coupling of SWAN and FINEL

Since waves can be of impact in shaping flow fields, SWAN can be used to include the wave fields in a FINEL2D computation. In the context of this study, the coupling with SWAN in FINEL2D is used in two separate ways (Dam et al., 2005):

- The wave forces F_x, F_y are obtained from SWAN. These wave forces are then used to include the wave-driven currents in the flow fields.
- The orbital wave motion at the bed U_{orb} is also obtained from SWAN. This can be used to obtain the total shear stresses for the sediment transport computations.

3.3. XBeach non-hydrostatic

XBeach (eXtreme Beach behavior model) is a wave model developed by Deltares (Deltares, 2025b). It is designed as a nearshore hydrodynamic and morphodynamic model, particularly for modeling the coastal response during storm conditions, including processes as dune erosion, overwash, and breaching. In the current version of XBeach, three different hydrodynamic modes can be selected:

1. Stationary mode: A fully phase-averaged model; neglects infragravity waves.
2. Surfbeat mode: In this mode, the short wave variations on the wave group scale and the associated long waves are resolved while the short waves are averaged.
3. Non-hydrostatic mode: A phase-resolving model; a pressure correction term allows the modeling of individual waves.

This section describes some of the governing equations, processes, and conditions for XBeach in non-hydrostatic mode. The other hydrodynamic modes are not used in this research and are, therefore, not discussed here. Most of the information in this section is obtained from the XBeach documentation (McCall et al., 2022).

3.3.1. Domain

The coordinate system in XBeach is implemented in such a way that the x-axis is always pointing towards the coast. The grid in XBeach should be curvilinear, but the grid step sizes over the domain may vary. When a rectangular grid is applied, the grid can be rotated about its origin (see Figure 3.1).

XBeach uses a staggered grid, where all scalar quantities (bed levels, water levels, concentrations) are defined at the cell centers, while velocities and transport are defined at the cell interfaces. The model solves a set of coupled two-dimensional horizontal (2DH) equations that govern wave propagation, flow, sediment transport, and bed level changes, and it can accommodate time-varying spectral wave and flow boundary conditions.

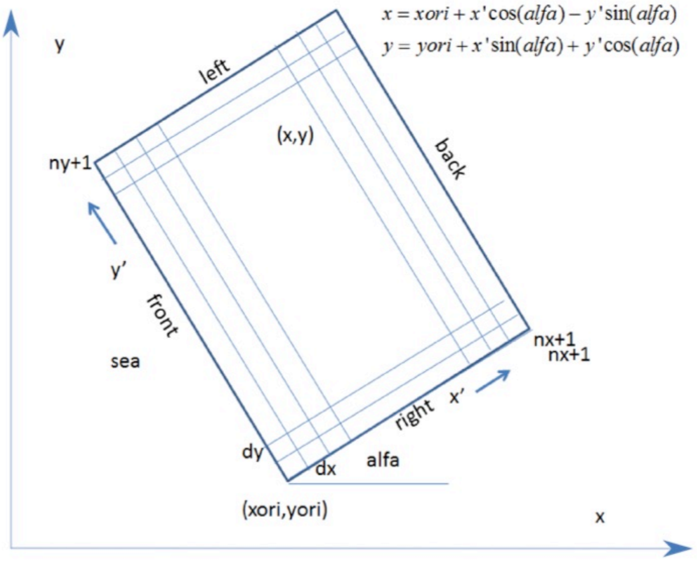

Figure 3.1: XBeach rectangular grid, rotated (McCall et al., 2022)

3.3.2. Governing equations

The non-hydrostatic mode of XBeach is based on the work by Zijlema and Stelling (2008) and solves the depth-averaged, incompressible Navier-Stokes equations, including non-hydrostatic pressure and turbulent stresses, to simulate the propagation and transformation of surface gravity waves in the nearshore zone. Most of the information in this section was obtained from the XBeach non-hydrostatic model description by Smit et al. (2010).

The global continuity equation is given by:

$$\frac{\partial \zeta}{\partial t}+\frac{\partial (UH)}{\partial x}+\frac{\partial (VH)}{\partial y}=0 \tag{3.15}$$

where ζ is the free surface elevation, $H=\zeta+d$ is the total water depth (with d being the bed level, positive downward), and U and V are the depth-averaged horizontal velocity components.

The depth-integrated momentum equations in the x, y, and the vertical direction are given in their conservative form by (Smit et al., 2010):

$$\frac{\partial (HU)}{\partial t}+\frac{\partial}{\partial x}\left(HU^2+\frac{1}{2}gH^2+Hp-\frac{1}{\rho}H\tau_{xx}\right)+\frac{\partial}{\partial y}\left(HUV-\frac{1}{\rho}H\tau_{yx}\right)=gH\frac{\partial d}{\partial x}-p\frac{\partial d}{\partial x}+S_x \tag{3.16}$$

$$\frac{\partial (HV)}{\partial t}+\frac{\partial}{\partial x}\left(HUV-\frac{1}{\rho}H\tau_{xy}\right)+\frac{\partial}{\partial y}\left(HV^2+\frac{1}{2}gH^2+Hp-\frac{1}{\rho}H\tau_{yy}\right)=gH\frac{\partial d}{\partial y}-p\frac{\partial d}{\partial y}+S_y \tag{3.17}$$

$$\frac{\partial (HW)}{\partial t}+\frac{\partial (HUW)}{\partial x}+\frac{\partial (HVW)}{\partial y}=-p_{\text{surface}}+p_{\text{bottom}}+\frac{1}{\rho}\frac{\partial}{\partial x}(H\tau_{xz})+\frac{1}{\rho}\frac{\partial}{\partial y}(H\tau_{yz}) \tag{3.18}$$

In these equations:

- p is the non-hydrostatic pressure;
- τ_{ij} are the horizontal turbulent stress components;
- S_x and S_y represent sink and source terms;
- W is the depth-averaged vertical velocity.

The equations are discretized using a staggered grid and solved using a McCormack scheme (Smit et al., 2010). This approach, combined with a non-hydrostatic pressure correction, enables accurate resolution of short waves, including dispersive effects and nonlinear wave transformations, while allowing wave breaking to be captured naturally without the need for an explicit breaking model.

Five different formulations are implemented in XBeach for determining the friction coefficient c_f (McCall et al., 2022). The default method for calculating bed friction is Manning's method (Manning, 1891). A typical Manning bed friction would be 0.02, and the relationship between Manning's coefficient and bed friction c_f is (e.g. McCall et al., 2022):

$$c_f=\frac{gn^2}{h^{1/3}} \tag{3.19}$$

Where n is the Manning coefficient (Battjes & Labeur, 2021).

Boundary conditions

The governing equations require appropriate conditions for velocity and pressure at all domain boundaries, including the free surface, the bottom, and the lateral and open boundaries.

At the **free surface**, the pressure is assumed to be equal to atmospheric pressure, which is set to zero for convenience. This yields the boundary condition for the non-hydrostatic dynamic pressure:

$$p(x,y,z=\zeta,t)=0 \tag{3.20}$$

At the **bottom boundary**, a kinematic boundary condition is applied that ensures zero vertical velocity at the bottom:

$$w=\frac{\partial d}{\partial t}+u\frac{\partial d}{\partial x}+v\frac{\partial d}{\partial y} \tag{3.21}$$

where d is the bed level. The bottom stresses are incorporated through a quadratic friction law:

$$\tau_{bx} = \rho c_f U|U|, \quad \tau_{by} = \rho c_f V|V| \tag{3.22}$$

with c_f being a friction coefficient.

At the **open boundaries**, either the free surface elevation or the depth-averaged velocity can be prescribed. For non-hydrostatic simulations, it is recommended to force the model with a prescribed velocity time series, which contains the time-varying boundary signal (Smit et al., 2010). The short-wave motion is included in this velocity signal.

At **closed boundaries**, no flow is allowed to pass through; the discharge is zero, making the boundary fully reflective. This setup represents a solid vertical wall. The velocity component perpendicular (normal) to the boundary is set to zero, while for the components parallel (tangential) to the boundary, free-slip conditions are used, meaning their gradients are zero and no shear stress is applied.

Reduced 2-layer model

To enhance the dispersive accuracy of XBeach non-hydrostatic without substantially increasing computational cost, a reduced two-layer formulation was introduced (De Ridder et al., 2020). This approach divides the water column into two vertical layers but simplifies the formulation by assuming that the non-hydrostatic pressure in the lower layer is constant. The upper layer still has a non-hydrostatic pressure, and the pressure at the surface remains zero. This allows the model to capture dispersive effects more accurately than the original single-layer implementation, particularly in intermediate water depths where $kh > 1$. Importantly, the additional computational cost when working with this model is low (De Ridder et al., 2020).

3.3.3. Wave breaking

Wave breaking in XBeach non-hydrostatic is not explicitly modeled because only the surface elevation is tracked in the model, making it impossible to track the complete shape of the wave. Instead, as wave steepening progresses and the wave front becomes unstable, the model simulates breaking as a hydraulic jump across which momentum is conserved.

To avoid requiring multiple vertical layers at the wave front, the model uses the hydrostatic front approximation (Smit et al., 2013, 2014) (HFA). When a wave becomes sufficiently steep, a hydrostatic pressure is enforced at the wave front. This transition is triggered based on a surface steepness criterion (default in XBeach: $\frac{\partial \eta}{\partial t} > 0.4$. The HFA ensures that wave breaking is modeled realistically, even with coarse vertical grids. Once the front has passed and the wave steepness reduces, the model reverts to non-hydrostatic mode once another steepness criterion is met (default in XBeach $\frac{\partial \eta}{\partial t} < 0.1$). Both these thresholds can be adjusted in XBeach using the model parameters `maxbrsteep` and `secbrsteep`, respectively (McCall et al., 2022).

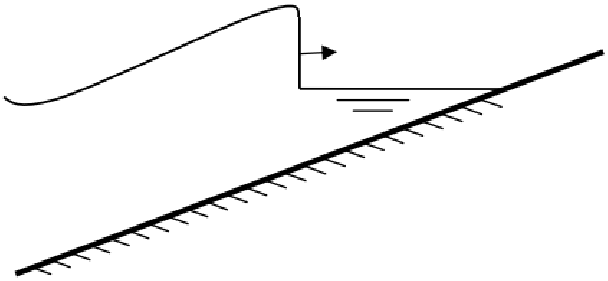

Figure 3.2: Wave steepens (Smit et al., 2010)

4

Wave propagation - Taman case study

This chapter introduces a physical model study of the Taman port, which is used to evaluate the performance of two numerical wave models, SWAN and XBeach non-hydrostatic, in simulating wave propagation under the influence of channel refraction. The physical model includes a navigational channel, breakwaters, and wave-measuring instruments. XBeach non-hydrostatic is calibrated and assessed against measurements from two wave conditions, representing moderate and extreme storm events. This chapter outlines the model setups, sensitivity analyses, and calibration procedures, followed by a comparison of model results with physical measurements to determine each model's capability in capturing wave transformation processes relevant to coastal and channel design.

4.1. Physical model description

An overview of the physical model is shown in Figure 4.1a (a larger version can be found in Appendix C). The model contained a port entrance with a navigation channel and two breakwaters. It was scaled using Froude's law, with a scale factor of 57.6 (Riezebos, 2014).

(a) Map of physical model (Riezebos, 2014) (enlargened version in Appendix C)

(b) Photograph of the western breakwater in the physical model (Riezebos, 2014)

Figure 4.1: Physical model

In the physical model, six wave gauges (WHMs) and four directional wave gauges (GRSMs) were placed. The WHMs measured surface elevation, which can be processed into a wave spectrum, whereas GRSMs also measured velocity, which means that the incoming waves can be separated from the reflected waves. The gauges were placed all over the domain, some in front of the channel, inside the channel, and behind the channel and breakwaters. The locations of all gauges are shown in Figure 4.1a and Appendix C. Some notable gauges for this study are:

- **GRSM1:** The most offshore wave gauge can be used to check whether the incoming wave spectrum is correct.
- **WHM02:** The wave gauge in front of the channel where wave focusing is expected to arise.
- **WHM03/WHM05:** The wave gauge inside the channel with little influence from the breakwaters.
- **WHM01:** The wave gauge on the other side of the channel.

4.1.1. Notable model features

Below, the most important features of the physical model are briefly described.

Breakwaters

The domain contained two breakwaters; their trunks consisted of rubble mound material with a fine mesh over it. The breakwater heads were made with more detail, containing a filter layer with a rubble mound core (Riezebos, 2014). A photograph of the western breakwater can be seen in Figure 4.1b.

Foreshore

In the construction of the physical model, it was impossible to include the complete foreshore because of space restrictions. Therefore, waves were generated in deep water (−21.3 m CD - chart datum). Then, the waves went through a transition with a 1:10 slope up to shallow water (−11 m CD). This ensured that waves were generated in deep water and are depth-restricted when they reached the harbor (Riezebos, 2014).

Channel

The channel was −21.3 m CD deep, and the side slopes of the channel had a slope of 1:5. The width of the channel was 250 m near the harbor entrance, and transitioned into 170 m further offshore. In reality, the channel was approximately 14 km long, but only the kilometer ($\approx 3L_0$) closest to the harbor was built in the physical model (due to space constraints).

At the channel entrance, a sill was constructed, see Figure 4.2. This was done such that waves didn't penetrate the channel at the offshore boundary, which was not realistic because the channel was, in reality, much longer than in the physical model.

Figure 4.2: Sill constructed at the channel entrance (Riezebos, 2014)

Wave spending beaches

At the northern boundary, wave-spending beaches were constructed, designed to absorb wave energy and reduce reflection. These wave-spending beaches consisted of rubble mound rocks with a large diameter.

4.1.2. Wave conditions

Five different scenarios were used in the physical test, named T01 to T05. However, the spectrum was given for only two conditions, so only conditions T01 and T03 are analyzed in this case study. T01 was a condition belonging to a storm with a 1-year return period, with a significant wave height of $H_s = 3.0\text{m}$. T03 was the design condition of the port belonging to a storm with a return period of 100 years with $H_s = 4.70\,\text{m}$. The conditions are specified in Table 4.1.

Case	Conditions	H_s [m]	T_p [s]	Water level [m]	Duration [hr]
T01	10-year return period	3.00	9.43	+0.8	3
T03	100-year return period	4.70	14.45	+0.8	6

Table 4.1: Conditions in the physical model

The wave conditions also contained approximately 20° of directional spreading. The full 1D and 2D spectra for both conditions are provided in Appendix C.

4.2. Numerical setup

This section describes the setup of the numerical models SWAN and XBeach in the context of the physical model described in Section 4.1. The bathymetry used in the models is adapted from the physical model (Riezebos, 2014) and shown in Figure 4.3. In SWAN, the breakwaters are removed and replaced with obstacle objects in the model.

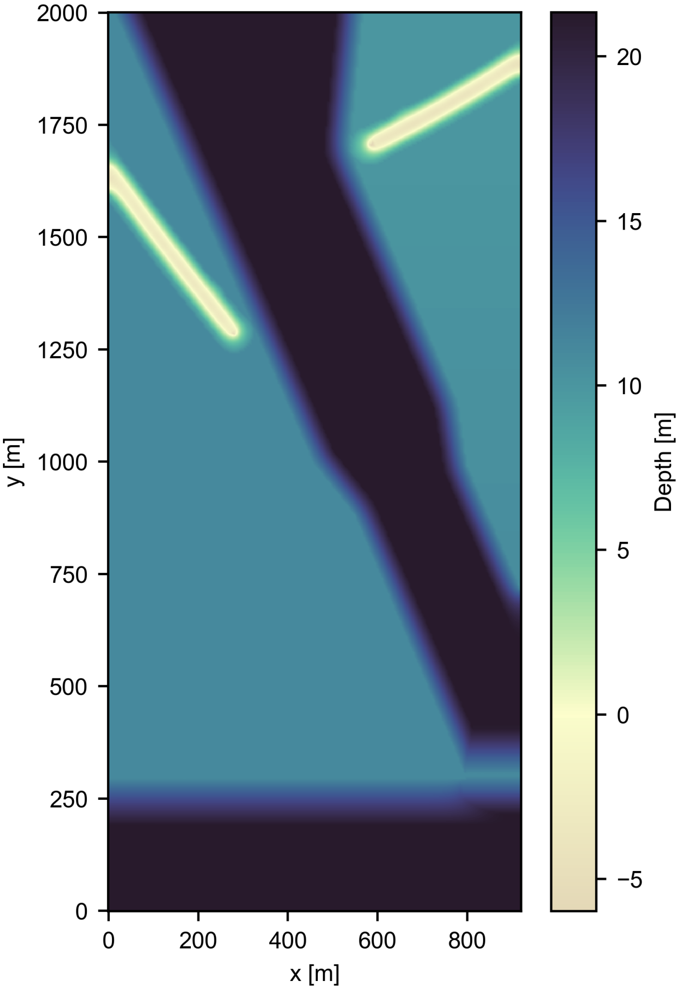

Figure 4.3: Bathymetry of the Taman case

4.2.1. SWAN

The setup of the SWAN model is a slightly modified version of the setup by Dusseljee et al. (2014). This section discusses how the grid is implemented and what physical processes are active during the computation. The complete input file can be found in Appendix A.

Grid

In SWAN, the computational grid and bottom grid are defined separately. The computational grid has a resolution of $dx = dy = 3\,\mathrm{m}$, the bottom grid has a resolution of $dx = dy = 5\,\mathrm{m}$. The computational grid is longer than the bottom grid; it extends northwards for another 1500 meters. The directional bins in the computational grid have a size of $5°$.

Physical processes

SWAN is run in third-generation mode for wind input, quadruplet interactions, and white capping. Whitecapping is computed with the method by Alves and Banner (2003) (as applied to SWAN in van der Westhuysen et al. (2007)). The default constant depth-induced breaking is applied in SWAN. Quadruplet and triad interactions are included. The bottom friction is computed with the method by Hasselmann et al. (1973) with the default friction parameter.

Boundary conditions

On the south boundary, a 1D spectrum is imposed with directional spreading. On the left and right boundaries, obstacles are placed with a reflection coefficient of 0.85. An important difference to the obstacles used by Dusseljee et al. (2014) is that they are placed one meter inwards. This appeared to influence the wave energy on the lee side of the channel a lot (Section 4.4).

Other parameters

The breakwaters are implemented using obstacles. These obstacles follow the shape of the breakwaters and have a reflection coefficient of 0.42. In the bathymetry used in SWAN, the breakwaters seen in Figure 4.3 are therefore removed and replaced by the obstacles.

4.2.2. XBeach non-hydrostatic

XBeach (Deltares, 2025b) is applied to the physical case in non-hydrostatic mode. This section discusses the model settings and how the physical model features are implemented in the numerical model. The input file can be found in Appendix A.

Grid

In XBeach, the computational grid and bottom grid are identical. A rectangular grid is applied, with a constant step size in x- and y-direction. The grid and bottom files are obtained from the study by Eikema et al. (2018), which is a triangular mesh grid with a resolution of 2 m. This grid is then processed and edited in Python using cubic interpolation to shape it into a rectangular grid and to obtain the desired grid resolution.

In the paper by Dusseljee et al. (2014), the grid step size used for SWASH was 3 m, which is less than 50 points per deep water wave length. This is not the ideal resolution for a non-hydrostatic model, but they chose this resolution to keep the computational costs low. The SWASH user manual (the SWASH team, 2025) recommends at least 100 steps per wavelength for more energetic conditions. With a wave height of 3 m and a depth of 11 m, $H/d \approx 0.27$, and the conditions can be considered energetic. Dusseljee et al. (2014) found that because the spatial resolution is too low, the higher frequencies dampen in the first few grid cells. They recommend a grid size of 0.5 m. For this study, a grid size of 1 x 1 m was chosen, the justification for this grid size is given in Section 4.3.1.

Physical processes

The physical processes included in the model are flow, long waves, viscosity, and advection. Short waves are excluded because in the non-hydrostatic mode, these are inherently part of the equations. Sediment transport and morphology are also excluded since this case study focuses on the hydrodynamics of the models.

Boundary conditions

The wave boundary conditions are obtained from the study by Riezebos (2014), as discussed in Section 4.1.2. The wave spectrum was extracted as a 2D SWAN spectrum from one of the first grid cells in the SWAN simulation domain. XBeach non-hydrostatic can accept 2D SWAN spectra as input, which are then used to generate a surface elevation and flow velocity time series at the boundary. The time step (dt) of this generated time series is set to 0.5 s.

The flow boundary condition at the front (wave maker) is set to `nonh_1d`. At the lateral boundaries (left and right), the flow boundary condition is set to `wall`, ensuring no flux across these boundaries to represent the guiding walls present in the physical model. The wave-dissipating beaches at the rear are simulated as realistically as possible by applying an absorbing-generating (weakly reflective) boundary condition.

Tidal motion is not included in the physical model. The initial water level in the numerical model is set to 0.8 m, consistent with the physical model setup.

Other parameters

Bed friction is handled as is default in XBeach; the bed friction is similar to what it is in SWAN. Manning's method for bed friction is used with $n = 0.02$, a typical value for bed friction on a sandy coast (McCall et al., 2022).

Wave breaking in non-hydrostatic mode can be controlled in the model by parameters that define the maximum wave steepness before wave breaking α and the steepness at which they reform after breaking β. Their default values are 0.4 and 0.1, respectively. An interdependence of grid resolution and wave-breaking parameters was found and is further analyzed in Section 4.3.1.

Also, the reduced two-layer model (De Ridder et al., 2020) was turned on. This model improves the dispersive behavior of the model, and during the testing of the model, the two-layer model was even necessary for a stable modeling result. Not including the two-layer model also resulted in problems regarding the parallelization between the different cores.

4.3. Model sensitivity and calibration of XBeach non-hydrostatic

During the implementation and testing of the XBeach Non-Hydrostatic model, several parameters were identified as having a large influence on the model outcomes. These include the spatial resolution, wave-breaking parameters, and an energy correction factor.

4.3.1. Sensitivity to Model Parameters and Spatial Resolution

Model testing revealed an interdependence between the wave-breaking parameters and the spatial resolution, which resulted in problems in generating accurate results. The default values for the wave-breaking parameters α and β in XBeach are 0.4 and 0.1, respectively.

Simulations with a grid resolution of 2×2 m resulted in plots where wave focusing due to refraction on the channel slopes was clearly observed (see the left plot in Figure 4.4). However, refining the spatial resolution to 1×1 m significantly altered the results: the refraction pattern on the west side of the channel largely disappeared, and wave energy is much lower around the channel (right plot in Figure 4.4).

This effect was investigated by looking at the instantaneous surface elevation and wave-breaking. Figure 4.4 displays the instantaneous wave breaking in red at one time step at $t = 700\,\mathrm{s}$, overlaid on the significant wave height H_{m0}. The left panel shows results for $dx = dy = 2\,\mathrm{m}$, where breaking is confined near the breakwaters and the region between the left breakwater and the western boundary. In contrast, the right panel with $dx = dy = 1\,\mathrm{m}$ shows wave breaking throughout the domain, including the channel itself, leading to energy dissipation.

These results suggest that the spatial resolution affects the modeled wave steepness, which in turn influences wave breaking. The wave-breaking parameters control the threshold for breaking, while resolution determines the represented steepness. This is further investigated during model calibration.

Another problem encountered during testing in XBeach non-hydrostatic was a discrepancy between the imposed wave height and the predicted wave height in the first few grid cells. The difference between imposed and modeled H_{m0} can be seen in a 1D transect of the Taman bathymetry in Figure 4.5. Two issues are observed: (1) a discrepancy between the wave height imposed and the wave height in the very first grid cell in the domain, and (2) a rapid decrease in wave height in the first few meters of the domain. This is a known problem in non-hydrostatic models (Vasarmidis et al., 2024). Common practice is to solve this discrepancy by simply increasing the energy in the imposed spectrum by a factor from here on referenced as C_{energy} (de Wit, 2016; Dorochinski, 2014).

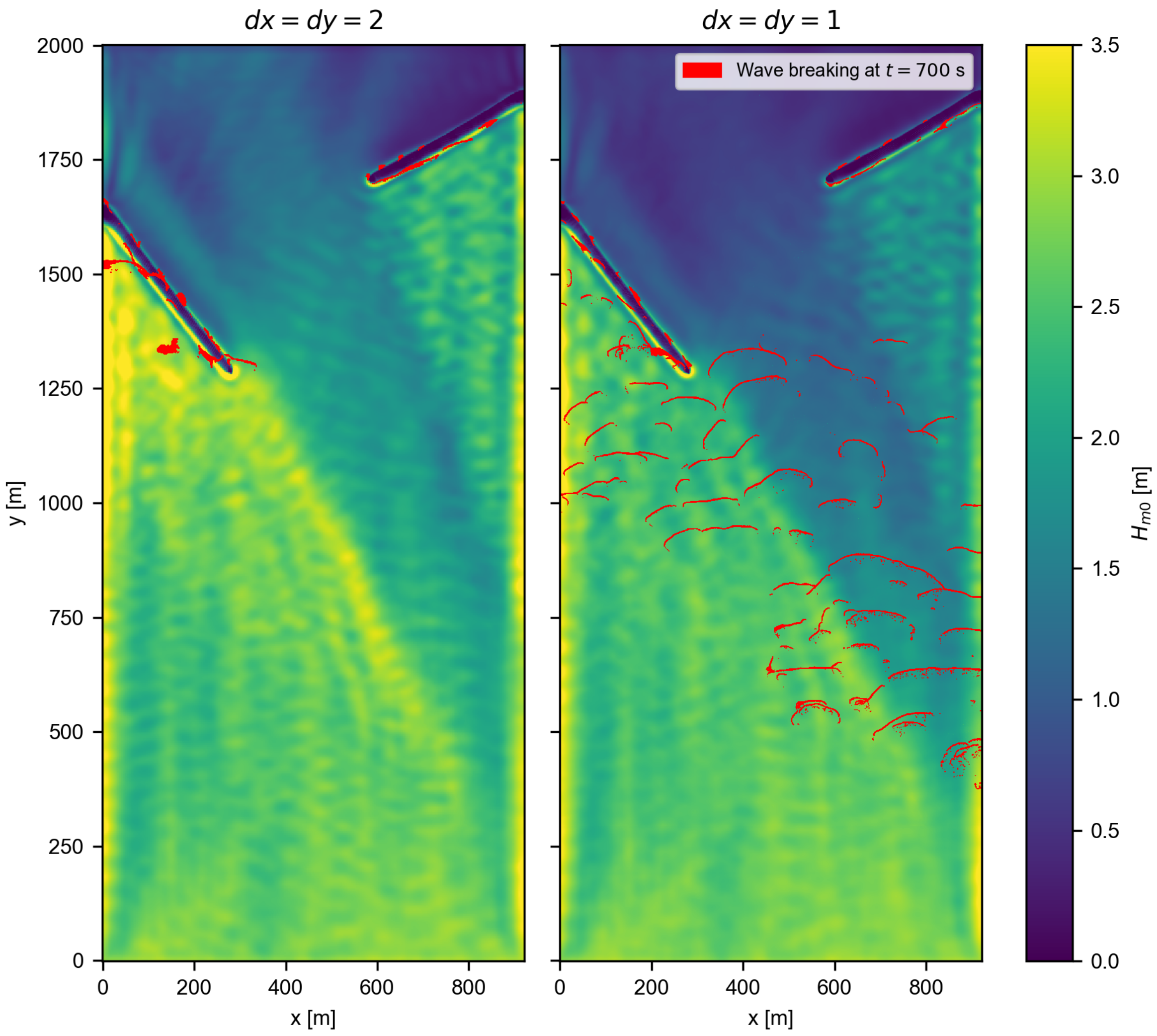

Figure 4.4: Effect of spatial resolution on wave breaking at $t = 700\,\mathrm{s}$, with default breaker parameters. Red areas indicate where waves are breaking. Left: $dx = dy = 2\,\mathrm{m}$. Right: $dx = dy = 1\,\mathrm{m}$. Colormap shows H_{m0} in meters.

Figure 4.5 shows runs with four different energy factors. The energy factors correspond to an increase of H_{m0} in the spectrum of 0.1 m at a time. The energy within the spectrum scales quadratically with the significant wave height ($E \propto H_{m0}^2$). An energy factor of 1.21 (equivalent to a 10% increase in H_{m0}) provided the best results after the initial drop in the first few meters. After 40 grid cells, the significant wave height is 3.05 m when the energy factor is applied, while the wave height is only 2.78 m when the energy factor is not applied.

4.3.2. Calibration methodology

After determining sensitive parameters for XBeach non-hydrostatic, a calibration was performed by varying the parameters α, β, C_{energy}, dx, and dy. α and β are the wave-breaking parameters, C_{energy} is an energy factor which is elaborated upon below, and dx and dy represent the spatial resolution. The range within which the parameters are varied is given in an overview in Table 4.2.

The spatial resolution - dx and dy - is varied between 2 m, 1 m, and 0.5 m. In most of the domain, the wavelength is $L \approx 100\,\mathrm{m}$. Therefore, a spatial resolution of 2, 1, and 0.5 m corresponds to 50, 100, and 200 points per wavelength.

The maximum steepness α varies from the default value in XBeach, 0.4, to the value recommended for non-hydrostatic models in literature (Smit et al., 2013, 2014), 0.6. The value of β is recommended

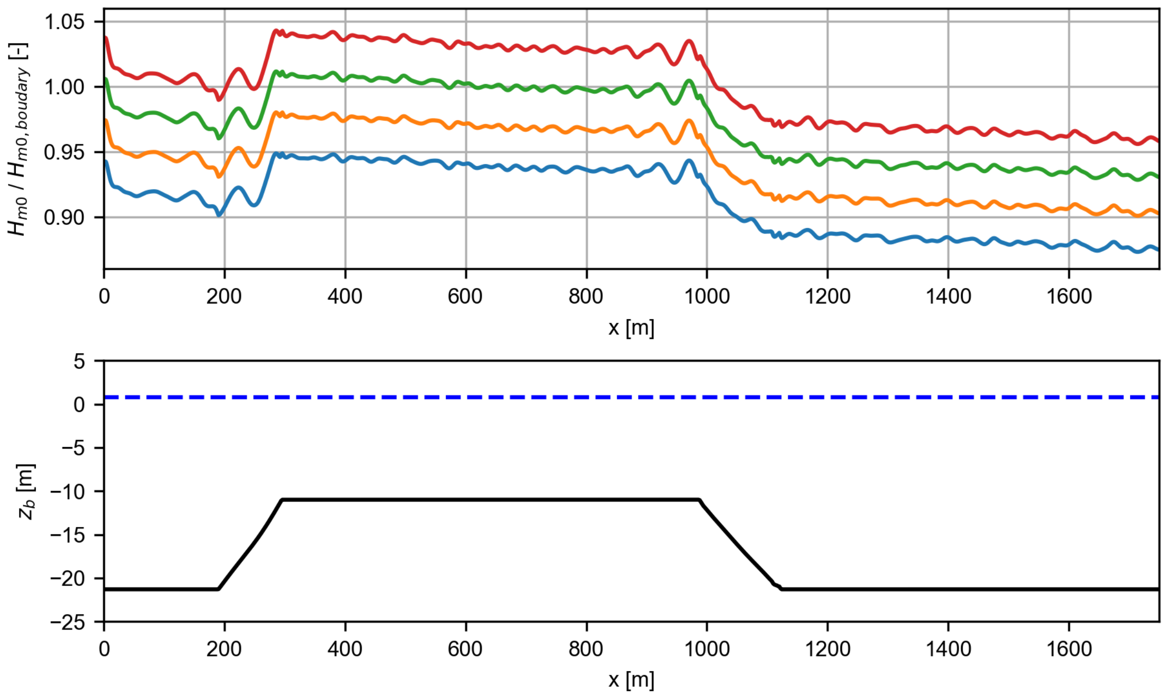

Figure 4.5: Top graph: Ratio in wave height between original imposed wave height and computed wave height for different energy factors. Bottom graph: bathymetry for 1D test, cross-section of 2D physical model

Parameter	Symbol	Range
Spatial resolution	dx	0.5 m, 1.0 m and 2.0 m
Maximum steepness	α	0.4, 0.5, 0.6
Reform steepness	β	0.1, 0.2, 0.25, 0.3
Energy factor	C_{energy}	1.00, 1.21

Table 4.2: Parameter ranges used in the XBeach NH calibration

at 0.3 when $\alpha = 0.6$, so during all calibration runs $\beta = \frac{1}{2}\alpha$, except for one run with the XBeach default values: $\alpha = 0.4,\ \beta = 0.1$.

Lastly, the energy factor added to the spectrum at the wave boundary is changed between 1 (no energy increase) and 1.21 (a 10% increase in wave height), according to the results seen in Figure 4.5.

4.3.3. Calibration results

The results of the calibration runs are shown in Table 4.3. Each run is evaluated based on the root-mean-square error (RMSE) between observed (Dusseljee et al., 2014) and simulated values of:

- significant wave height H_{m0}
- spectral wave period $T_{m-1,0}$
- peak wave period T_p

The RMSE is calculated with:

$$\mathrm{RMSE} = \sqrt{\frac{1}{n}\sum_{i=1}^{n}(y_i - \hat{y}_i)^2} \tag{4.1}$$

Where i are the observation points (Section 4.1), y_i is the observed value, and $\hat{y}_i$ is the predicted value.

The RMSE quantifies the difference between the observed and the predicted values.

A closer inspection of Table 4.3 provides further insight into how each parameter affects model performance. First, increasing the energy factor to 1.21 significantly reduces the RMSE in wave height for coarser resolutions, confirming the necessity for compensating for energy loss near the wave maker. However, at finer resolutions ($dx = dy = 0.5$), this same increase results in model instability.

Second, varying the wave-breaking parameters α and β yields small changes in RMSE, in contrast to what was observed during testing with XBeach (Figure 4.4). Runs with $\alpha = 0.6$ and $\beta = 0.3$ often provide slightly better or comparable results relative to lower values of α, aligning with the recommendations from literature (Smit et al., 2013, 2014). Notably the simulations using the default $\beta = 0.1$ while keeping $\alpha = 0.4$, clearly provide worse results (primarily for $dx = dy = 1$), particularly in H_{m0} ($1.2\,\mathrm{m}$). This indicates how the model in this case is mostly sensitive to a run with low β (in combination with a fine resolution).

The spatial resolution is perhaps the most influential parameter. Moving from $dx = 2\,\mathrm{m}$ to $dx = 1\,\mathrm{m}$ generally reduces the RMSE, but moving further to $dx = 0.5\,\mathrm{m}$ either causes the model to crash or results in extremely long computation times. Not only do they become unstable, but they also don't offer better results (lower RMSE). An explanation for this is again the wave breaking, which is initiated more often with a finer grid, because inspection of run 15 before it imploded gave a slightly better result than run 9.

Model instability is primarily associated with the combination of fine grid spacing and elevated wave energy. Out of all runs with $dx = 0.5\,\mathrm{m}$, only two completed successfully, and neither applied the energy factor. This means that for this case, the risk of the model run becoming unstable increases when the grid is made finer and the conditions become more energetic. This risk must be taken into account when choosing the model parameters.

The RMSE values for the spectral wave period $T_{m-1,0}$ are more consistent over the different calibration runs. Changing the wave-breaking parameters or energy factor has very little effect on the mean period. Increasing the spatial resolution from $dx = dy = 2\,\mathrm{m}$ to $dx = dy = 1\,\mathrm{m}$ slightly improves the RMSE.

		RMSE H_{m0} [m]		RMSE $T_{m-1,0}$ [s]	
dx, dy [m]	$\alpha,\ \beta$	$C_{\text{energy}} = 1$	$C_{\text{energy}} = 1.21$	$C_{\text{energy}} = 1$	$C_{\text{energy}} = 1.21$
2	0.4, 0.1	0.574	0.448	1.127	1.248
	0.4, 0.2	0.565	0.386	1.121	1.120
	0.5, 0.25	0.563	0.384	1.123	1.120
	0.6, 0.3	0.566	0.385	1.126	1.120
1	0.4, 0.1	1.200	1.065	1.519	1.592
	0.4, 0.2	0.429	Unst	0.936	Unst
	0.5, 0.25	0.428	0.255	0.928	0.978
	0.6, 0.3	0.422	0.253	0.927	0.978
0.5	0.4, 0.2	1.275	Unst	1.412	Unst
	0.5, 0.25	0.890	Unst	1.116	Unst
	0.6, 0.3	Unst	Unst	Unst	Unst

Table 4.3: Calibration results for different combinations of α and β at $dx, dy = 2$ m and two energy dissipation factors C_{energy}. "Unst" implies that the model became unstable at some point during the simulation, yielding an incomplete result.

The runs with a spatial resolution of 200 cells per wavelength take more than two days, and the majority of them have imploded at some point during computation, giving no result. From these results, it is difficult to assess whether a grid with 100 cells per wavelength ($dx = 1\,\mathrm{m}$) is sufficient or whether it is needed to make the grid finer.

4.3.4. Grid resolution convergence study

To determine whether a 1 x 1 m (100 points per wavelength) grid is fine enough, an additional test was performed in 1D with different dx. A cross-section was taken from the 2D model (the same as in Figure 4.5), and the model was run with $dx = 3\,\mathrm{m}$, $dx = 2\,\mathrm{m}$, $dx = 1\,\mathrm{m}$, and $dx = 0.5\,\mathrm{m}$. For simplicity, not the same spectrum was used as in the 2D test, but a JONSWAP spectrum with the same characteristics as the 2D test ($H_{m0} = 3$ and $T_p = 9.4$).

This test is based on the convergence of the results. At some point, the results won't improve by increasing the spatial resolution. At this point, a sufficient spatial resolution is reached. The results from this test are shown in Figure 4.6. Dusseljee et al. (2014) recommend a spatial resolution of 0.5 x 0.5 m. However, the result from the run with a resolution of 1 x 1 m is very close to the result of 0.5 x 0.5 m, and doubling the spatial resolution multiplies the necessary computation time by 8.

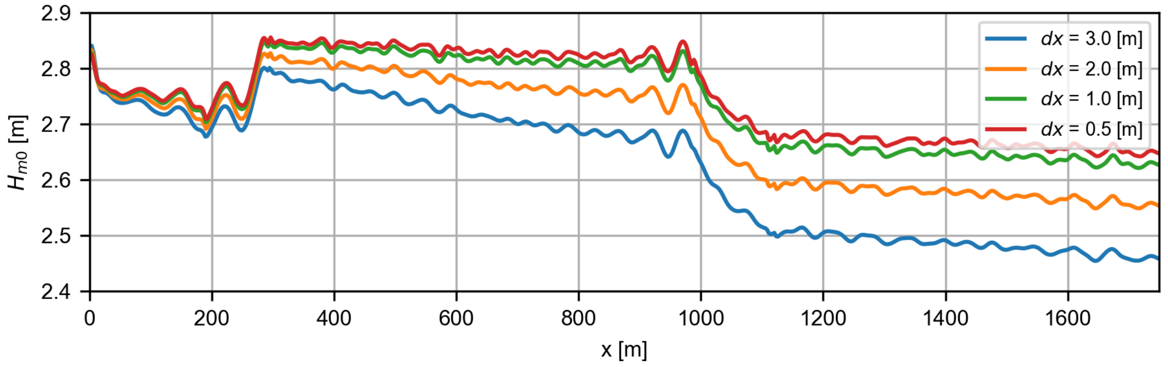

Figure 4.6: 1D test with different spatial resolutions

By combining the results from the 2DH calibration runs and the 1D convergence test, the parameters that best fit the model are determined. Making the trade-off between accuracy, model stability, and computational cost identifies the parameter combination of $dx = 1\,\mathrm{m}$, $\alpha = 0.6$, $\beta = 0.3$, and $C_{\mathrm{energy}} = 1.21$ as the most robust and efficient. An overview of these parameters and their results is given in Table 4.4.

Parameter	Chosen Value / Result	Unit
Spatial resolution $dx = dy$	1.0	m
Maximum steepness α	0.6	–
Reform steepness β	0.3	–
Energy factor C_{energy}	1.00	–
RMSE in H_{m0}	0.253	m
RMSE in $T_{m-1,0}$	0.978	s
RMSE in T_p	1.120	s
Simulation time	6.8	hrs

Table 4.4: Final XBeach NH parameter configuration

4.4. Numerical results

The results of the Taman case using both SWAN (phase-averaged) and XBeach non-hydrostatic (phase-resolving) in both conditions (Table 4.1) are shown and discussed in this section. In XBeach, both cases were run on a grid with approximately 100 grid points per wavelength. For condition T01 ($L \approx 100\,\mathrm{m}$), this is equivalent to $dx = dy = 1\,\mathrm{m}$, and for condition T03 ($L \approx 150\,\mathrm{m}$), this is equivalent to $dx = dy = 1.5\,\mathrm{m}$. In XBeach, the models were run with wave breaker parameters $\alpha = 0.6$, and $\beta = 0.3$, and an energy factor of 1.21 was used in both conditions. The input files for SWAN and XBeach are given in Appendix A.

Before providing the results, an overview of the computation time of all model runs is shown in Table 4.5. SWAN was run in stationary mode and finished in under 20 minutes for both conditions, on 16 cores. XBeach, in contrast, required over 14 hours on a 32-core processor to simulate the T01 condition and over 4.5 hours for T03 with a faster 32-core processor.

Model	Condition	Runtime	Cores
SWAN	T01	14 min	16
	T03	16 min	16
XBeach non-hydrostatic	T01	14 h 31 min	32
	T03	4 h 35 min	32FF

Table 4.5: Computation time of the Taman case model runs

These numbers show the enormous difference in computational cost between the two models. SWAN running on 16 cores is 6100% faster than XBeach running on 32 cores in T01.

4.4.1. Significant wave height

See in Figure 4.7 plots of the significant wave height of all four model runs. The XBeach runs were run for three hours, and SWAN was run in stationary mode. The significant wave height after the XBeach run was calculated using the variance of the surface elevation ($H_{m0} = 4\sqrt{m_0} = 4\sqrt{Var(\eta)}$). This is why the XBeach result may seem less ”smooth” than the SWAN result. Note that the scale of the colorbars between the two conditions is not equal.

In all plots, channel refraction is present in the domain because of the sharp increase in wave height near the channel slope. This zone of increased wave height starts at the beginning of the channel and widens towards the north. Inside the channel and on the other side of the channel, the wave heights are lower. In between the western breakwater and the western boundary, very high wave heights are observed, mostly in the XBeach simulations, possibly due to reflection from the boundary and the breakwater.

The plots of SWAN and XBeach are visually quite similar for each condition. The biggest visual difference is that the wave heights on the lee side of the channel, in front of the eastern breakwater, are higher in XBeach than in SWAN.

4.4.2. Comparison to observations

See in Tables 4.6 and 4.7 a comparison between the measurements (Dusseljee et al., 2014) and model results of H_{m0} and $T_{m-1,0}$, with the RMSE and normalized RMSE ($\mathrm{nRMSE} = \mathrm{RMSE}/(\max(y)-\min(y))$) of all measurement locations. A comparison to T_p can be found in Appendix E. Because the peak period is sensitive to outliers, it was not included in the analysis here.

When only the RMSE of the significant wave height is taken into account, SWAN performs slightly better in the less energetic conditions, and XBeach performs slightly better in the more energetic conditions. When the mean spectral period $T_{m-1,0}$ is considered, SWAN performs better in both conditions. In general, both models perform better in T01 than in T03.

Two points that are not very important to the channel refraction are GRSM1, which is the most offshore point, and can be used to determine if the incoming energy is correct. WHM07 lies behind the eastern breakwater and is very much influenced by diffraction and not by channel refraction. The other eight points can be split up into three parts:

1. **In front of the channel:** GRSM2, WHM02
2. **Inside the channel:** GRSM3, WHM03, WHM04, WHM05
3. **On the lee side of the channel:** GRSM4, WHM01

In front of the channel, where channel refraction occurs, both models predict the wave heights very accurately. In T01, XBeach is off by only 1%, and SWAN is off by 3-4%. In T03, these values are slightly higher (2% in XBeach, 4-6% in SWAN), but still very close to the observations.

Table 4.6, displays that inside that channel, the wave energy is usually underestimated by both wave models (7-18% by XBeach and 4-13% by SWAN). For T03, the wave height inside the channel is even further underestimated (18-23% by XBeach and 17-30% by SWAN).

On the lee side of the channel, XBeach performs better than SWAN. SWAN tends to underestimate

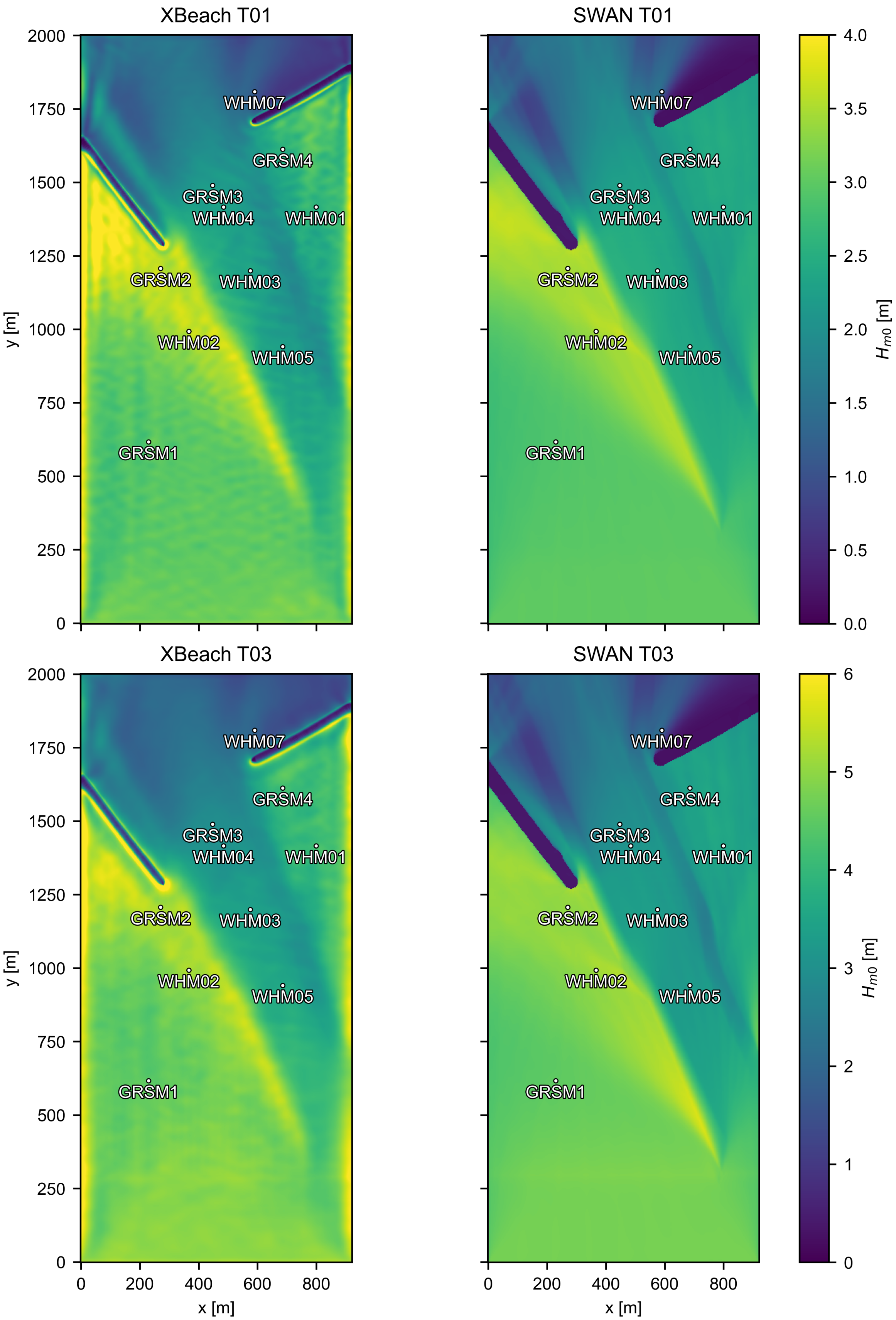

Figure 4.7: Comparison of H_{m0} between SWAN and XBeach in two different conditions

the wave heights on the lee side more than XBeach does. This is most visible in T03, where SWAN is 20-21% off and XBeach only 3-4% off from the observations.

The mean spectral periods $T_{m-1,0}$ predicted by the numerical models mostly show that SWAN tends to underestimate the mean period, while XBeach tends to overestimate the period.

T01	Physical Model		SWAN		XBeach	
	H_{m0}	$T_{m-1,0}$	H_{m0}	$T_{m-1,0}$	H_{m0}	$T_{m-1,0}$
GRSM1	3.03	7.89	2.89 (-4%)	7.32 (-7%)	3.03 (0%)	8.66 (+10%)
GRSM2	3.62	8.41	3.48 (-4%)	7.89 (-6%)	3.65 (+1%)	8.97 (+7%)
GRSM3	2.35	7.38	2.26 (-4%)	6.79 (-8%)	2.17 (-7%)	8.04 (+9%)
GRSM4	2.48	7.33	2.32 (-7%)	6.94 (-5%)	2.57 (+4%)	8.49 (+16%)
WHM01	2.81	7.66	2.37 (-16%)	7.01 (-8%)	2.53 (-10%)	8.71 (+14%)
WHM02	3.55	8.11	3.45 (-3%)	7.87 (-3%)	3.52 (-1%)	8.81 (+9%)
WHM03	2.77	7.19	2.43 (-12%)	6.81 (-5%)	2.32 (-16%)	8.07 (+12%)
WHM04	2.60	7.11	2.35 (-10%)	6.80 (-4%)	2.30 (-12%)	8.22 (+16%)
WHM05	2.73	6.97	2.38 (-13%)	6.60 (-5%)	2.24 (-18%)	7.94 (+14%)
WHM07	1.30	7.23	1.32 (+2%)	7.83 (+8%)	1.13 (-13%)	8.04 (+11%)
RMSE	–	–	0.24 m	0.48 s	0.26 m	0.89 s
nRMSE	–	–	0.320	0.578	0.334	0.785

Table 4.6: T01: Comparison of significant wave height H_{m0} and mean wave period $T_{m-1,0}$ between the physical model, SWAN, and XBeach.

T03	Physical Model		SWAN		XBeach	
	H_{m0}	$T_{m-1,0}$	H_{m0}	$T_{m-1,0}$	H_{m0}	$T_{m-1,0}$
GRSM1	4.79	10.8	4.51 (-6%)	10.3 (-5%)	4.47 (-7%)	11.5 (+6%)
GRSM2	5.32	11.6	5.02 (-6%)	11.4 (-2%)	5.24 (-2%)	12.0 (+4%)
GRSM3	3.58	10.2	2.96 (-17%)	9.0 (-11%)	2.93 (-18%)	11.6 (+14%)
GRSM4	4.28	11.0	3.36 (-21%)	9.7 (-11%)	4.13 (-4%)	11.8 (+8%)
WHM01	4.35	10.7	3.50 (-20%)	9.9 (-7%)	4.20 (-3%)	12.5 (+17%)
WHM02	5.35	11.4	5.14 (-4%)	11.2 (-1%)	5.23 (-2%)	11.9 (+5%)
WHM03	4.42	10.2	3.30 (-25%)	9.2 (-9%)	3.37 (-24%)	11.5 (+13%)
WHM04	3.97	9.9	3.10 (-22%)	9.1 (-8%)	3.01 (-24%)	11.6 (+17%)
WHM05	4.65	10.1	3.27 (-30%)	8.8 (-13%)	3.60 (-23%)	11.2 (+12%)
WHM07	2.10	9.5	1.94 (-8%)	10.8 (+13%)	1.87 (-11%)	11.5 (+21%)
RMSE	–	–	0.78 m	0.92 s	0.61 m	1.30 s
nRMSE	–	–	0.490	0.667	0.435	0.796

Table 4.7: T03: Comparison of significant wave height H_{m0} and mean wave period $T_{m-1,0}$ between the physical model, SWAN and XBeach.

4.4.3. Comparison of spectra

Figures 4.8 and 4.9 show the spectra observed in the physical model and the spectra modeled in SWAN and XBeach at each of the measurement locations in T01 and T03, respectively. The spectra are produced using Welch's method with a Hanning window, a segment length of 256 samples, and a sampling frequency of 2 Hz, resulting in a spectral density estimate. Welch's method smoothes the spectrum, which can otherwise have a very jagged shape, for improved readability and interpretability.

When the spectra of T01 in Figure 4.8 are observed, it can be seen that, first of all, in the points in front of the channel (GRSM1, GRSM2, WHM02), the energy in the frequencies near the peak frequency is higher in XBeach than what was measured. On the other side, the higher frequencies are lower than what was measured. This increase of energy at the peaks might be caused by the energy factor that is added to the spectrum in XBeach. This increases energy in the whole spectrum, but when the higher energies dampen (Dusseljee et al., 2014), only the lower frequencies remain higher in energy. This might also explain why the mean spectral period $T_{m-1,0}$ tends to be overestimated in XBeach; the ”weight” in the spectra appears to shift a bit to the lower frequencies (higher periods) in the spectrum in XBeach.

In the spectra of the points inside the channel (WHM03, WHM04, WHM05, GRSM3), the observations show two peaks in the spectrum. SWAN and XBeach follow the first peak quite well but do not reproduce the second peak as clearly. Only in the spectrum of WHM05 does XBeach display two peaks.

On the lee side of the channel (WHM01, GRSM4), the shapes of the model spectra resemble those of the observed spectra. As observed in front of the channel, XBeach tends to overestimate the energy in the lower frequencies near the peak and underestimate the energy in the higher frequencies.

The spectra of T03 in Figure 4.9 generally show a larger difference to the observed spectra, which aligns with the higher RMSE found for T03. At the points in front of the channel (GRSM1, GRSM2, WHM02), there is no similar increase in energy near the peak frequency in XBeach as seen in T01. At the most offshore point, GRSM1, both SWAN and XBeach underestimate the energy in the higher frequencies. In GRSM2, SWAN underestimates the higher frequencies, while XBeach performs better. In WHM02, both SWAN and XBeach overestimate the energy in the lower frequencies and underestimate the energy in the higher frequencies. In this region, XBeach and SWAN produce very similar results.

Inside the channel (WHM03, WHM04, WHM05, GRSM3), the models underestimate the energy in the spectrum. SWAN shows even lower spectral energy compared to XBeach. While XBeach performs reasonably well in the lower frequencies (e.g., WHM04, WHM05), both models greatly underestimate the energy at higher frequencies.

In the points on the lee side of the channel (WHM01, GRSM4), XBeach matches the energy in the higher frequencies of the spectrum quite well. In WHM01, XBeach shows a large peak around 0.08 Hz, which is not present in the measurements. SWAN tends to underestimate the higher frequencies but does well around the lower frequencies in WHM01.

4.5. Chapter summary

This chapter evaluated the performance of two numerical wave models: SWAN (phase-averaged) and XBeach non-hydrostatic (phase-resolving). The model outputs were compared to measurements from a physical scale model of the Taman port. The physical model included a navigation channel, breakwaters, and wave-measuring instruments, and provided data under two storm conditions (T01 and T03).

The numerical model setups were described, with particular attention to how physical processes and boundary conditions were implemented. For XBeach, a calibration and sensitivity study was performed to address the interdependence between spatial resolution and wave-breaking parameters. This revealed that finer grid resolutions lead to increased wave breaking and energy dissipation, requiring adjustment of wave-breaking parameters. The wave energy at the boundary was slightly increased due to a discrepancy between the imposed wave height and the modeled wave height in the first few grid cells. A 1D convergence study confirmed that a resolution of 100 cells per wavelength provides a good balance between computational cost and accuracy.

In terms of performance, both models reproduced wave heights well in offshore regions and in front of the channel. On the lee side of the channel, both models tended to underestimate wave energy, with XBeach showing slightly higher accuracy in the more energetic case (T03). Inside the channel, both models underestimated the significant wave heights. XBeach generally overestimated the mean spectral wave period, while SWAN showed better results.

Spectral comparisons showed that XBeach tended to underestimate high-frequency energy, particularly in the less energetic condition. The shape of both models’ spectra was very comparable to the measured spectra.

Overall, both models provide a relatively accurate result compared to the measurements. XBeach was slightly more accurate than SWAN in the locations on the lee side of the channel, but was computationally much more expensive. These findings highlight the trade-off between accuracy and computational efficiency that must be made.

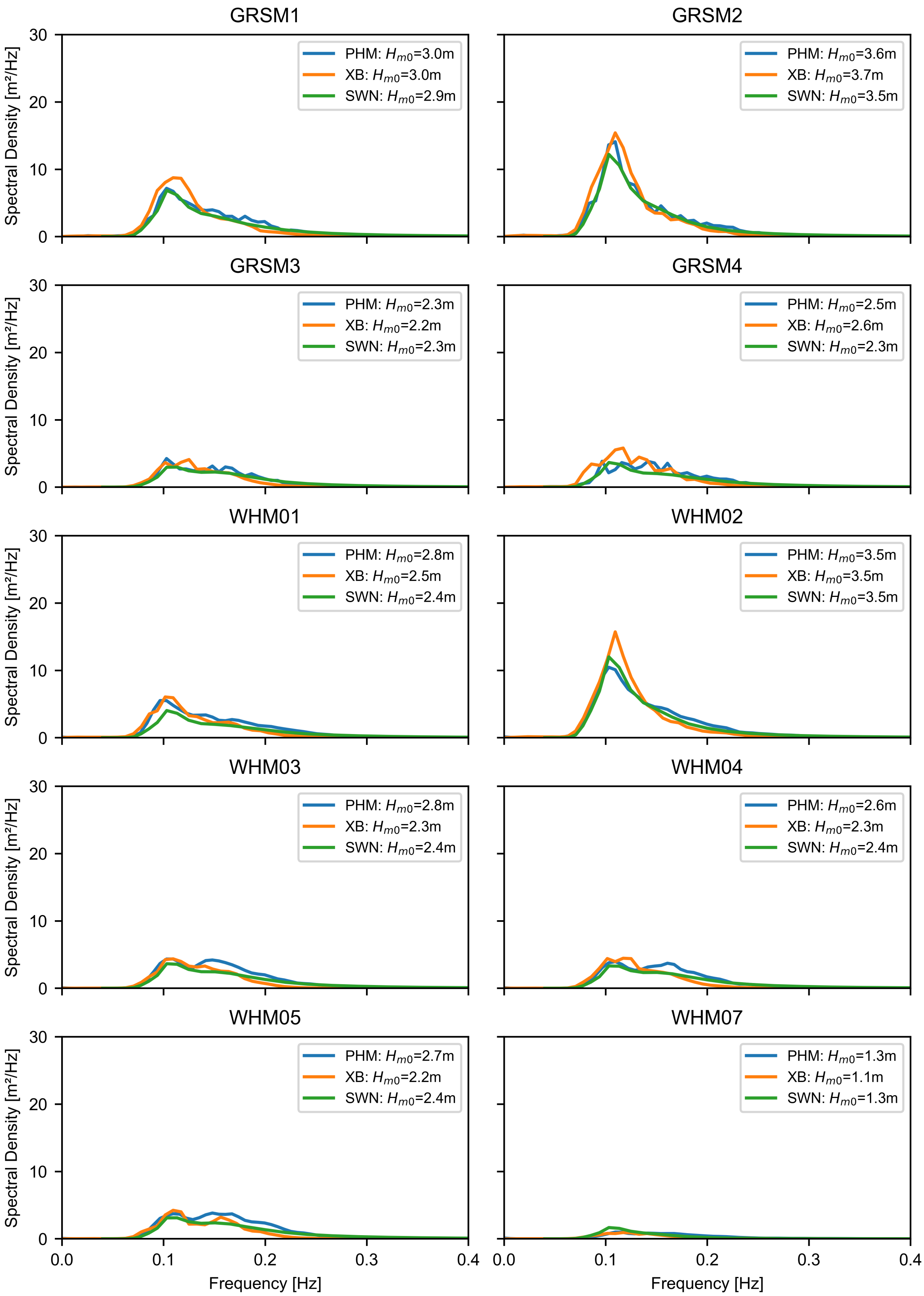

Figure 4.8: Comparison of observed spectra and spectra predicted by SWAN and XBeach in condition T01.

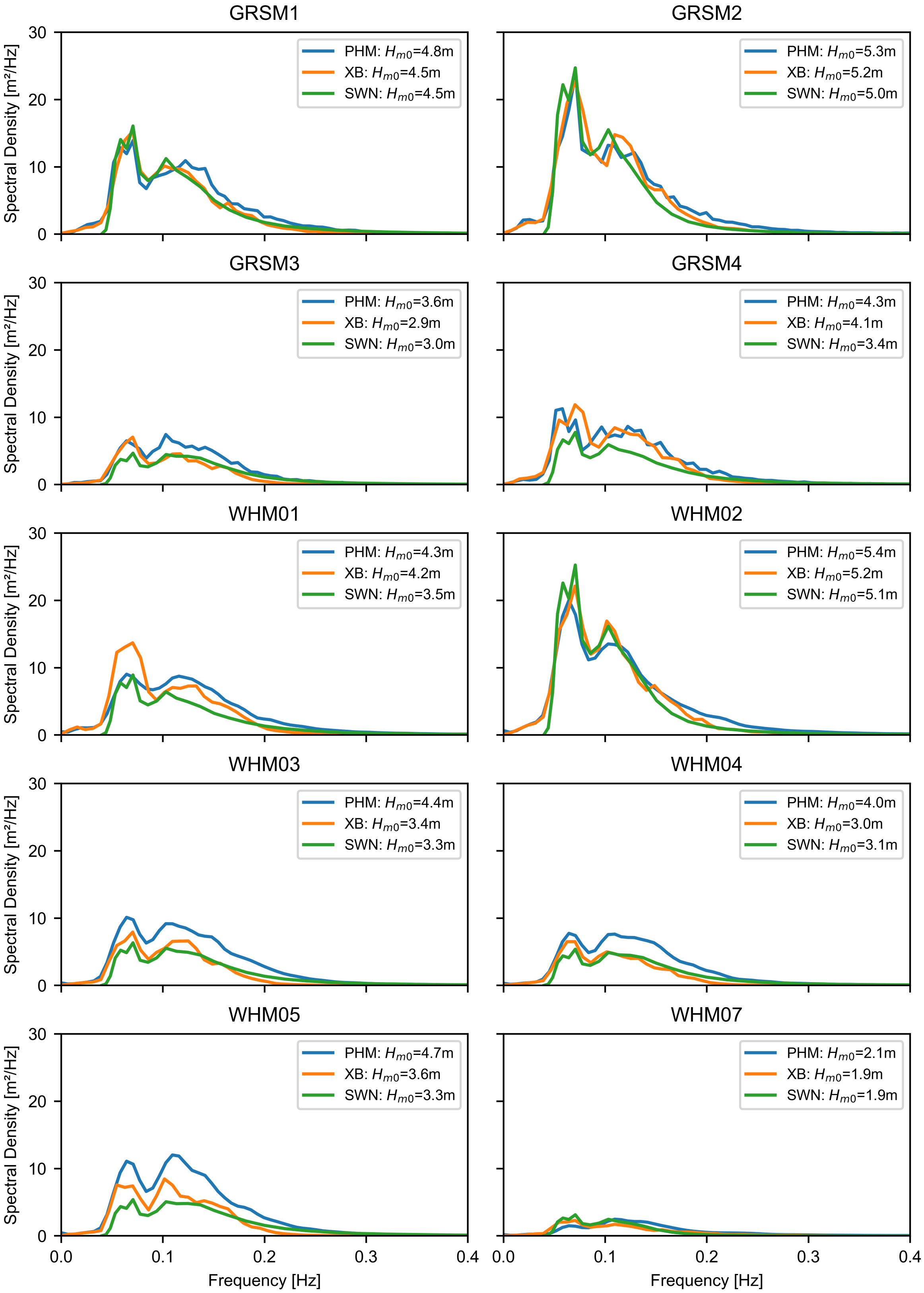

Figure 4.9: Comparison of observed spectra and spectra predicted by SWAN and XBeach in condition T03.

Key takeaways

- SWAN is significantly more computationally efficient (14 mins in T01 on 16 cores) compared to XBeach (14.5 hrs in T01 on 32 cores).
- A grid resolution of 100 cells per wavelength with $\alpha = 0.6$, $\beta = 0.3$, and an energy factor of $C_{\text{energy}} = 1.21$ produced the most reliable results in XBeach.
- Based on the RMSE of H_{m0} in all measurement locations, both models performed very similarly. XBeach performed slightly better in the more energetic conditions (T03).
- XBeach non-hydrostatic outperformed SWAN on the lee side of the channel, particularly under energetic conditions (T03).
- Inside the channel, both models underestimate the wave heights.
- XBeach tended to overestimate the spectral mean period $T_{m-1,0}$, whereas SWAN underestimated it.
- The shape of the spectra from both models resembled the shapes of the measured spectra very well.

5

Sediment transport - Synthetic case study

This chapter investigates the effect of channel refraction on wave propagation, flows, bed shear stresses, and sediment transport patterns along a simplified coastal system with a dredged channel. The study is motivated by the need to better understand how refraction at the channel edges could influence the coastal morphology, and what level of modeling detail is required to accurately predict this process.

The analysis is based on a comparative modeling experiment using two different numerical approaches: a phase-averaged model (SWAN-FINEL) and a phase-resolving non-hydrostatic model (XBeach non-hydrostatic). The purpose of this numerical study is to assess how the model formulation influences the computed wave, flow, and sediment transport patterns in a complex situation (in this case, channel refraction).

A synthetic test case is proposed, consisting of a straight sandy coastline with a dredged navigation channel. Obliquely incident waves are imposed at the offshore boundary, inducing wave refraction along the channel edges. This case aims to assess how the choice of model influences the representation of wave transformation, flow patterns, and sediment transport, particularly around the channel.

Sediment transport plays an important role in the stability and functionality of navigation channels. When waves refract along the channel edges, they can alter both flow patterns and bed shear stresses in ways that affect sediment redistribution. Understanding these effects is crucial for predicting channel infilling, shoreline erosion or accretion, and the overall morphodynamic response of the coastal system. As such, this chapter focuses specifically on sediment transport processes as the variable for evaluating the impact of channel refraction.

5.1. Case description

This section describes the case that is used for this investigation. The aim of the bathymetry is to construct a simplified yet physically meaningful environment in which the effects of channel refraction can be isolated. The design reflects a setting in which processes important to erosion and accretion, such as wave-induced longshore currents and cross-shore hydrodynamic processes, are represented within the domain.

To facilitate this, a longshore-uniform coast with a constant slope is implemented. The coast is sloped such that waves will undergo shoaling and breaking and induce a longshore current. In the center of the domain, a navigation channel with constant side slopes is dredged. The bottom profile of the case is shown in Figure 5.1.

5.1.1. Domain size

The design of the case required balancing the size of the domain with computational feasibility. A coastal section of 2000 m by 3000 m was selected. This allows for the development of a longshore

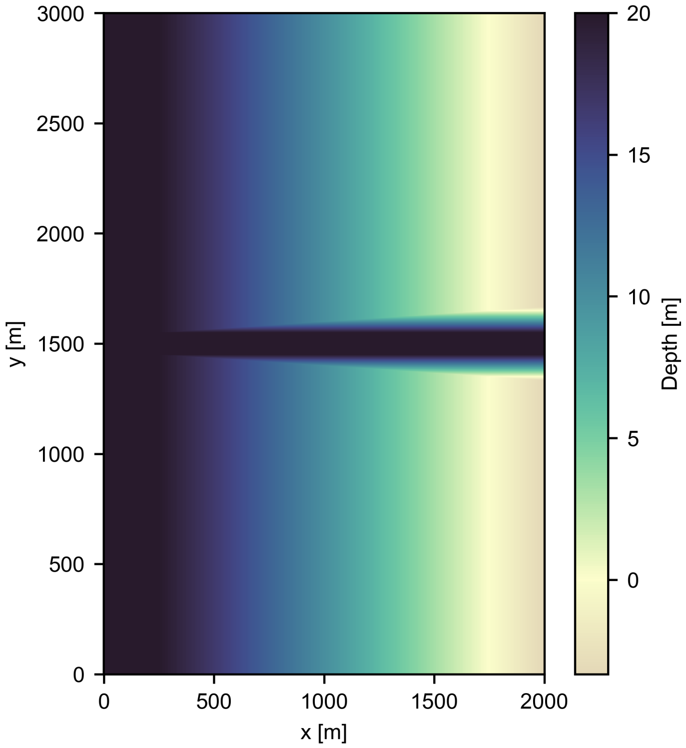

Figure 5.1: Alongshore-uniform coast with a dredged navigation channel

current on both sides of the channel while still keeping computation time under 24 hours. Model-specific boundary treatments are applied, as described in Section 5.2.

5.1.2. Bathymetry features

This subsection highlights the key features of the bathymetry and justifies design choices. An overview of bathymetric parameters is presented in Table 5.1.

Feature	Value	Unit
Max. depth	20	m
Min. depth	-3.33	m
Bottom slope	$1:75$	$-$
Channel width	100	m
Channel slope	$1:5$	$-$

Table 5.1: Bathymetry features overview

The offshore (western) boundary of the domain has a depth of 20 m, which corresponds to the offshore depth used in the Taman case (Section 4.1). Based on the boundary conditions described below, this depth is considered an intermediate depth.

The bottom slope of the domain is constant at 1:75. This value falls within the range of beach slopes commonly observed along the Dutch coast (1:200 to 1:50 (Bosboom & Stive, 2023)). A relatively steep slope was chosen to reduce the required domain length while still enabling realistic wave breaking and current generation. This slope results in a beach elevation of 3.33 m above mean sea level at the eastern boundary, ensuring that incoming wave energy is dissipated before reaching the eastern boundary. The depth contours are parallel and aligned with the shoreline.

The navigation channel is oriented perpendicular to the shoreline. It has a uniform depth equal to the offshore depth of 20 m and a width of 100 m. The side slopes of the channel are 1:5, consistent with the Taman case. Additionally, the seabed near the offshore boundary is flat over a distance of 250 m before the slope begins.

5.1.3. Boundary conditions

Waves propagate towards the beach from the west. The wave spectrum follows a JONSWAP distribution (Hasselmann et al., 1973), and its parameters are listed in Table 5.2.

Table 5.2: Wave spectrum parameters

Parameter	Value	Unit
H_{m0}	1.5	m
T_p	10	s
γ	3.3	–
ϕ_m	20	$^\circ$
σ	12.4	$^\circ$

The boundary spectrum has a significant wave height of $H_{m0} = 1.5\,\mathrm{m}$ and a peak period of $T_p = 10\,\mathrm{s}$, corresponding to a deep-water wavelength of $L_0 = gT^2/2\pi = 156\,\mathrm{m}$. The peak enhancement factor is set to the commonly used value of $\gamma = 3.3$. The peak wave direction is 290° clockwise from the north (20° clockwise from the west). A directional spreading of $\sigma = 12.4^\circ$ is applied. At the boundary, the waves are in intermediate depth conditions.

In summary, the imposed waves represent a typical JONSWAP spectrum with intermediate wave height and 10-second period. The frequency spreading is moderate, and the directional spreading is relatively narrow to ensure predictable refraction behavior at the channel.

Tides are excluded from the model to isolate the effects of channel refraction and reduce simulation complexity. Moreover, the simulation time is insufficient for tidal variation to play a significant role.

5.1.4. Sediment characteristics

Sediment characteristics influence both transport rates and the relative contributions of bed load and suspended load. Based on computations by Van Rijn (2007), bed load transport dominates under moderate wave conditions ($H_s = 1\,\mathrm{m}$) when the median grain size is approximately 1 mm. Therefore, a median grain diameter of $D_{50} = 1\,\mathrm{mm}$ is selected, which is considered relatively coarse sand (Bosboom & Stive, 2023). The sediment parameters used in the models are listed in Table 5.3.

Parameter	Value	Unit
D_{50}	1	mm
D_{90}	2	mm
ρ_s	2650	$\mathrm{kg/m^3}$

Table 5.3: Sediment characteristics in FINEL

5.2. Numerical setup

This section describes the numerical modeling approach used for the synthetic case. Two different models are used: SWAN-FINEL, a phase-averaged model containing wave-current interactions, and XBeach non-hydrostatic (XBNH), a phase-resolving model. The setups of both models are described in terms of spatial discretization, boundary conditions, hydrodynamic and morphological configurations, and temporal settings. The final part of this section also describes the offline sediment transport module that is used to compute sediment fluxes for both simulations.

5.2.1. SWAN-FINEL

This section describes the numerical setup of the SWAN-FINEL model. SWAN handles the wave computations, while FINEL is responsible for the flows and morphological processes. The goal of this setup is to evaluate how waves and currents interact with the channel and how this interaction drives sediment transport patterns in a phase-averaged way. Attention is given to the model grid, boundary conditions, initial conditions, hydrodynamic and morphological parameters, and temporal settings.

Domain and grid

FINEL requires the use of triangulated grids. A MATLAB script is used to interpolate the bathymetric data and domain structure from a regular rectangular grid onto a triangular mesh. The resulting grid is refined in the nearshore region and around the navigation channel, with straight contour lines aligned with the channel edges to improve representation of the channel geometry.

The full bathymetry used in the SWAN-FINEL model is shown in Figure 5.2. Two zoomed-in views highlighting the triangular mesh and the difference in resolution moving onshore are presented in the same figure. The straight contour lines at the deep channel edges are observed at $y = 2050\,\mathrm{m}$. The maximum area of the cells in the coarser area is 312 m^2, and 16 m^2 in the finer area. The grid has a total of 475 276 cells.

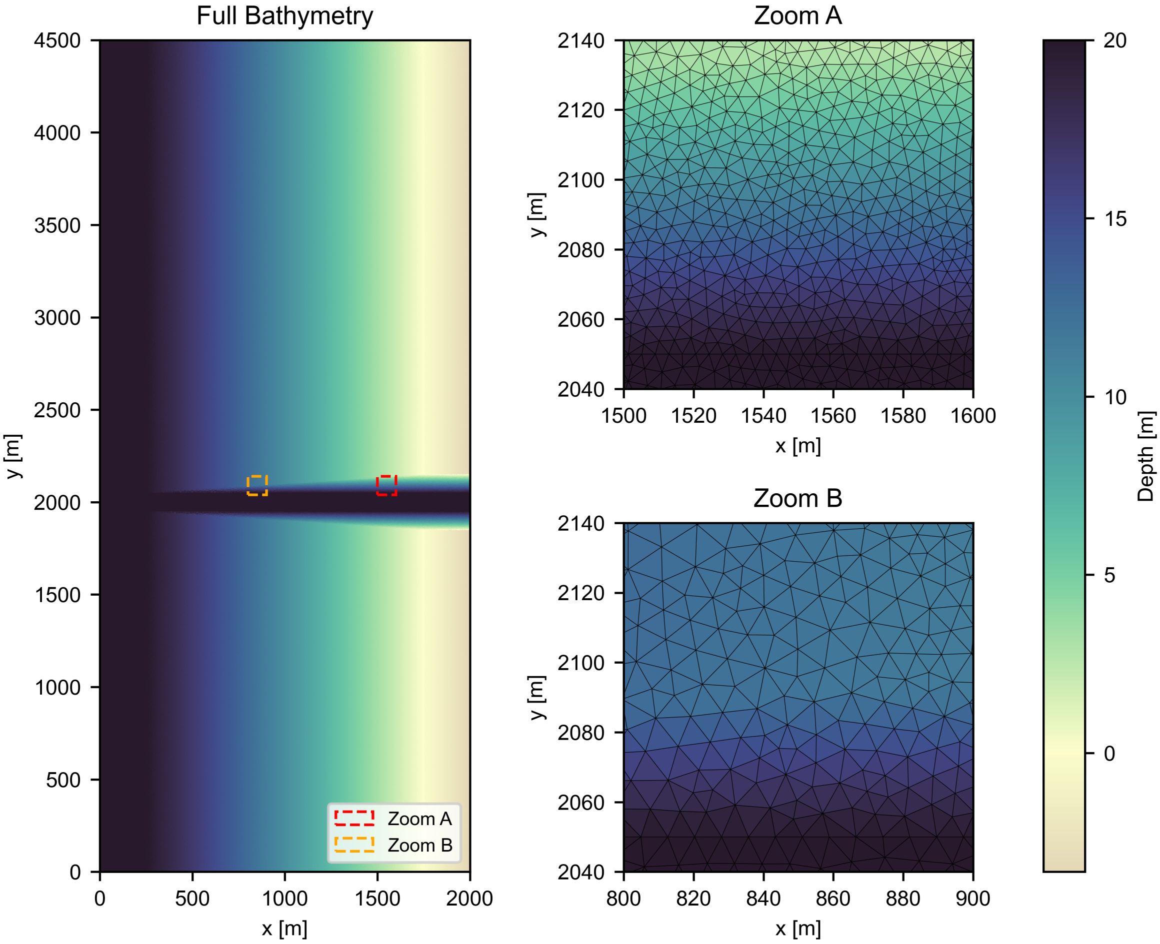

Figure 5.2: Overview and detail of the FINEL bathymetric grid

Boundary effects near the northern edge, caused by obliquely incoming waves and SWAN's lack of energy distribution over the wave crest, result in unrealistic wave heights and flow velocities. Extending the domain 1000 m northward and 500 m southward significantly reduces these artifacts. These buffer zones are excluded from the analysis.

SWAN operates on a separate grid, and the bathymetry for SWAN is generated by interpolating the FINEL mesh. The spatial extent of the SWAN grid matches that of the FINEL domain, but it has a coarser resolution, with $dx = 2\,\mathrm{m}$ and $dy = 5\,\mathrm{m}$.

Boundary conditions

The wave boundary conditions (Section 5.1.3) are applied in the SWAN model. Setting up the northern boundary required additional consideration. When waves are only imposed at the western boundary, a shadow zone develops near the northern boundary, resulting in an alongshore current directed northward. This current affects the region of interest, even with the extension of 1000 m towards the north.

To reduce this unwanted effect, a different wave condition is applied along the northern boundary in SWAN. From $x = 0$ to $x = 1000\,\mathrm{m}$, waves with regular heights (matching those at the western boundary) are imposed. From $x = 1000\,\mathrm{m}$ to $x = 1300\,\mathrm{m}$, the wave height decreases linearly to zero, reaching zero before the breaker line. This approach still induces a northward current, but with significantly reduced magnitude compared to not imposing waves on the northern boundary. As a result, boundary effects in the region of interest are minimal (Figure F.1 for the resulting velocity field in the full domain). The wave conditions are constant throughout the simulation.

In FINEL, Neumann flow boundary conditions are applied along the boundaries.

Hydrodynamic settings

All of the wave-related computations are handled by SWAN, so most of the hydrodynamic settings are tweaked in the SWAN input file. For simplicity, wind growth, whitecapping, and quadruplets are turned off. Triads are turned on with the DCTA method, and breaking is set to constant.

All flow-related computations are handled by FINEL. Some important settings include the bed roughness, which is defined with the Manning bed friction coefficient (Section 3.3.2) at $n = 0.02$. The sediment characteristics used in the model are displayed in Table 5.3. See Section 5.2.3 how sediment transport is assessed from the FINEL results.

Temporal settings

To assess the time required for the longshore current to develop, the model was first run for thirty minutes. The resulting longshore current in the transect at $y = 500\,\mathrm{m}$ is shown in Figure 5.3. From this transect, as well as others, it can be observed that the longshore current stabilizes after approximately 20-25 minutes. Based on this, a spin-up time of 30 minutes was chosen.

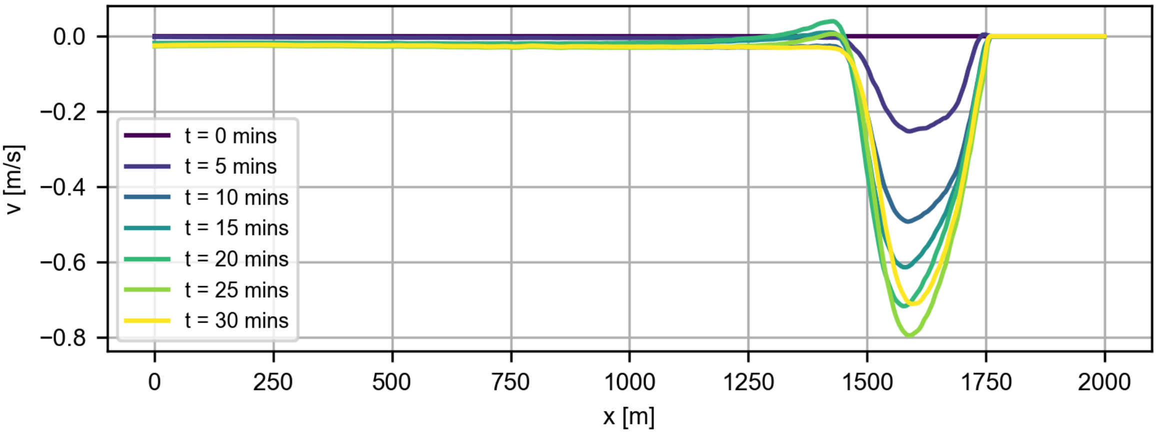

Figure 5.3: Longshore current velocity at different times at $y = 500\,\mathrm{m}$.

After the 30-minute spin-up period, the model is run for one hour, providing phase-averaged wave and flow fields output every two minutes. The phase-averaged wave and flow fields are then time-averaged over this one-hour period.

Coupling SWAN and FINEL

SWAN is run every 10 minutes; the wave conditions are kept constant, and the water level in SWAN is updated from FINEL. This makes sure that wave setup is included in the model. The wave stresses from SWAN are input into FINEL, which generates currents. The coupling is only from SWAN to FINEL, meaning that the currents computed by FINEL do not affect wave propagation.

5.2.2. XBeach

This section describes the numerical setup of the XBeach non-hydrostatic model. Attention is given to the model grid, boundary conditions, initial conditions, hydrodynamic and morphological parameters, and temporal settings.

Domain and grid

The grid used in XBeach is a regular grid with a resolution of $dx = 1\,\mathrm{m},\ dy = 2\,\mathrm{m}$. This corresponds to approximately 100 grid cells per deep-water wavelength in the propagation direction x, and 50 grid cells per wavelength in the alongshore direction. A resolution of 100 cells per wavelength was found to be the best balance between accuracy and computational effort in Section 4.3.4. The bathymetry used in the XBeach computations is given in Figure 5.1.

Boundary conditions

At the western boundary, a JONSWAP spectrum is imposed in XBeach with the values mentioned in Section 5.1. No issues were observed close to the wavemaker, making an energy factor like in Chapter 4 unnecessary. At the eastern boundary, a weakly absorbing boundary is imposed, but (almost) all wave energy should be dissipated before it reaches this boundary. On the northern and southern boundaries, cyclic boundary conditions are used. This option in XBeach allows for flows and waves leaving one boundary to enter the other. This configuration minimizes boundary effects and allows the domain to be reduced by approximately 60%.

Hydrodynamic settings

Like in Chapter 4, the reduced 2-layer mode is switched on, and the breaking parameters are set to $\alpha = 0.6$, and $\beta = 0.3$. Bed friction is set to Manning, with a bed friction coefficient of $n = 0.02$. Flow is turned on, and sediment transport and morphology are turned off. The model will still output bed shear stresses.

Temporal settings

Based on results from the SWAN-FINEL simulations, a spin-up time of 30 minutes was found to be sufficient to allow the development of a longshore current. However, SWAN-FINEL is a stationary model in which wave conditions are applied instantaneously throughout the domain from $t = 0$. In XBeach, the waves must propagate from the boundary toward the beach, which is why an additional 10 minutes was added to the spin-up duration. This results in a total spin-up time of 40 minutes for XBeach.

The XBeach simulation is also a run of 1 hour, preceded by the 40-minute spin-up phase. It outputs global Eulerian flow velocities, bed shear stresses, and surface elevation at a one-second interval. Such high temporal resolution is necessary for intra-wave sediment transport computations. The run also outputs averaged values, which are suitable for visualizing spatial patterns or comparing mean flow characteristics between models, while requiring significantly less storage and post-processing time than the global outputs. Time-averaged variables output are surface elevation, Eulerian flow velocity, and bed shear stress.

5.2.3. Sediment transport modeling

To obtain values for sediment transport fluxes, a model has to be chosen or designed. This section outlines and justifies all decisions that were made regarding the modeling of flows, bed shear stresses, and sediment fluxes.

The flow velocities and bed shear stresses can be obtained as model outputs from both XBeach non-hydrostatic and FINEL. In XBeach, we will use the bed shear stresses from the model directly. In FINEL, however, the flow velocities from currents and waves are used to compute the bed shear stress with the formulas in Section 2.7.1 because the formulations for wave-averaged shear stresses are simple and the results can be controlled and checked more easily. For the bed shear stress by waves, currents, and the mean bed shear stress under waves and currents combined, the following formulas are used:

$$\vec{\tau_c} = \rho \frac{g\vec{U}^2}{C^2} \tag{5.1}$$

Where C is the Chézy coefficient and $\vec{U}$ the depth-averaged flow velocity, both obtained from FINEL.

$$\vec{\tau_w} = \frac{1}{2}\rho f_w \vec{U_w}^2 \tag{5.2}$$

Where the orbital velocity of waves $\vec{U_w}$ is obtained from SWAN and f_w is the skin friction factor computed according to Equation (2.18) with T_p and A obtained from SWAN, and $k_s = 2.5, D_{50} = 0.0025$.

$$\vec{\tau_m} = \vec{\tau_c}\left[1 + 1.2\left(\frac{|\tau_w|}{|\tau_c| + |\tau_w|}\right)^{3.2}\right] \tag{5.3}$$

The implementation of the bed shear stress computations in Python is given in Appendix B.

The sediment fluxes resulting from the model's currents and waves are not assessed from the model output itself, but are assessed using an *offline* sediment transport model. There are two reasons for this:

1. The sediment transport modeling in XBeach non-hydrostatic is complex and is still in the research phase for 2DH.
2. Using an offline approach to sediment transport modeling allows full control over the applied transport formulations, enabling customization to suit the case and models under investigation.

As noted in Section 2.7.3, sediment transport modeling is highly empirical, and the calibration of the transport models is very important. In comparisons that were made between results of different (longshore) sediment transport models, large differences between the results are observed (Bayram et al., 2001). Therefore, when comparing sediment transport between SWAN-FINEL and XBeach non-hydrostatic, the choice of transport formulation must be consistent. The objective is to assess the impact of underlying model assumptions rather than to evaluate different transport formulations. Careful selection of the transport model is thus required for a meaningful comparison.

Since the aim is to compare model behavior rather than to produce accurate sediment transport predictions, a simplified sediment transport formulation is sufficient as long as it includes the relevant physical processes. A simpler model is preferred to minimize the influence of model-specific complexities.

A review of sediment transport formulations was presented in Section 2.7.3. The current section focuses on the selection and implementation of a sediment transport model for SWAN-FINEL and XBeach. Table 5.4 provides an overview of the considered transport models, including their main characteristics, advantages, limitations, and compatibility with the two models. Suitable transport models are selected according to the following criteria:

1. It needs to be applicable in both SWAN-FINEL and XBeach non-hydrostatic.
2. It needs to have a way to include intra-wave sediment dynamics.
3. A simple transport model is preferable compared to a complex one.

Meyer-Peter and Müller, 1948 is selected as the best model suited for implementation in XBeach non-hydrostatic in this case. It is chosen because it checks most boxes:

- It is a widely used formula, and very simple and intuitive to use.
- A lot of research has been done on this formula, e.g., Ribberink (1998) investigated Meyer-Peter-Müller in oscillatory flow with a superimposed current and Soulsby and Damgaard (2005) derived analytical expressions using wave-averaged values based on Meyer-Peter-Müller.
- Soulsby and Damgaard (2005) derived analytical expressions based on Meyer-Peter-Müller for wave-averaged values, making it easy to use in SWAN-FINEL.
- It has been applied to phase resolving (intra-wave) models before (e.g. Mancini et al., 2021; Reniers et al., 2013; van Rooijen, 2011; van Rooijen et al., 2012).

Table 5.4: Comparison of sediment transport models

Model	Type	Key features	Advantages	Disadvantages	FINEL	XBNH
Bailard, 1981	Bedload + suspended	Energy-based; uses wave orbital velocity and sediment concentration	Not very complex; works well in wave-dominated areas	Requires near-bed velocity, which is not computed in XBeach non-hydrostatic.	Yes	Yes
Engelund and Hansen, 1967	Total load	Empirical, based on total load transport by the mean flow	Simple and fast	Developed for mean-flow transport. Wave action in FINEL is not properly implemented; it has an Englund-Hansen waves module, but it is not entirely correct.	Yes	Yes
Meyer-Peter and Müller, 1948	Bedload	Based on the instantaneous Shield's criterion	Simple, fast, and designed for instantaneous flow stresses	Has no way of including influence of waves from wave-averaged approach	No	Yes
Nielsen, 2006	Bedload	Improvement of Meyer-Peter-Müller; includes wave asymmetry and boundary streaming	Good for swash zone and coastal regions	Designed for 1D; not applicable in FINEL. Introduces complex processes.	No	Yes
Van Rijn, 2007	Bedload + suspended load	Physically-based; includes slope effects, waves and currents	Robust and detailed; good for mixed conditions	Complex; more parameters needed; requires near-bed velocity.	Yes	No
Soulsby and Damgaard, 2005	Bedload	Empirical formulas for combined wave-current transport; includes influence of wave orbital velocity and current shear stress	Widely used; good for engineering applications; handles combined forcing well	May oversimplify complex sediment dynamics	Yes	No

Implementation of Meyer-Peter-Müller (XBeach non-hydrostatic)

The general formula for a Meyer-Peter-Müller transport model is (Amoudry & Souza, 2011; Meyer-Peter & Müller, 1948; Ribberink, 1998):

$$\Phi_b = \begin{cases} m\theta^P(\theta - \theta_c)^n & \text{for } \theta \geq \theta_c \\ 0 & \text{for } \theta < \theta_c \end{cases} \tag{5.4}$$

Where m, n, and P are empirical constants, θ_c is the critical Shields stress. In the original paper by Meyer-Peter and Müller (1948), $m = 8$, $n = 1.5$, $P = 0$. In this study, the recommendations by Soulsby and Damgaard (2005) are adapted with $m = 12$, $n = 1$, $P = 0.5$. The equation is written in vector form to account for the direction of flow in the computation. This results in the following sediment transport formula:

$$\vec{\Phi_b} = 12|\theta|^{1/2}(|\theta| - \theta_c)\frac{\vec{\theta}}{|\theta|} \tag{5.5}$$

Where $|\theta|$ is the Shields stress *magnitude*. The critical Shields parameter is dependent on the sediment diameter, sediment and water densities, and the kinematic viscosity of the water $\nu = 1.05 \cdot 1^{-6}$ (ITTC, 2011). It is computed according to the formulation by Soulsby and Whitehouse (1997):

$$\theta_c = \frac{0.3}{1 + 1.2D_*} + 0.055\left[1 - \exp\left(-0.02D_*\right)\right] \tag{5.6}$$

with

$$D_* = \left[\frac{g(s-1)}{\nu^2}\right]^{1/3} D_{50} \tag{5.7}$$

The implementation of the Meyer-Peter-Müller transport formula in Python can be found in listing B.2. The function expects as input the temporally and spatially varying bed shear stress in x and y direction $\tau_{b,x}$, $\tau_{b,y}$, the other parameters are constants:

- The median sediment grain diameter $D_{50} = 0.001\,\mathrm{m} = 1\,\mathrm{mm}$.
- The critical Shields' parameter θ_c - dependent on sediment and water characteristics.
- Sediment density $\rho_s = 2650\,\mathrm{kg/m^3}$ and water density $\rho_w = 1025\,\mathrm{kg/m^3}$.

Implementation of Soulsby (SWAN-FINEL)

In the phase-averaged wave and flow model, a different transport model is required. The time-averaged current cannot be input into the Meyer-Peter-Müller transport formulation, because this method doesn't include the effect of the wave motion on the sediment transport. When a weak current is present, waves could mobilize the sediment where the current alone would not. Waves can also enhance the transport even if the current is strong enough to mobilize sediment by itself (Soulsby & Damgaard, 2005).

Therefore, the sediment transport formulation by Soulsby (1997) is used to compute the sediment fluxes from the FINEL-SWAN model. This model is based on the Meyer-Peter-Müller sediment transport formulation, but it can be used with phase-averaged models because it evaluates the time average of the shear stresses over a wave cycle and thus includes the wave-induced bed shear stresses. This gives much different (and more correct) results than simply inputting the mean bed shear stress into the Meyer-Peter-Müller.

The time-averaged bed shear stress under combined waves and currents is computed with (Soulsby & Damgaard, 2005):

$$\Phi_{x1} = 12\theta_m^{1/2}(\theta_m - \theta_{cr}) \tag{5.8}$$

$$\Phi_{x2} = 12(0.9534 + 0.1907\cos 2\phi)\theta_w^{1/2}\theta_m \tag{5.9}$$

$$\Phi_x = \max\left(\Phi_{x1}, \Phi_{x2}\right) \tag{5.10}$$

$$\Phi_y = \frac{12(0.1907\theta_m\theta_w^2 \sin 2\phi)}{\theta_w^{3/2} + (3/2)\theta_m^{3/2}} \tag{5.11}$$

$$\text{subject to:} \quad \Phi_x = \Phi_y = 0 \quad \text{if} \quad \theta_{\text{max}} \leq \theta_{\text{cr}} \tag{5.12}$$

$$\text{where:} \quad \theta_{\text{max}} = \left[\left(\theta_m + \theta_w\cos\phi\right)^2 + \left(\theta_w\sin\phi\right)^2\right]^{1/2} \tag{5.13}$$

In this formulation, Φ_x is the dimensionless transport in the current direction and Φ_y is the dimensionless transport in the direction perpendicular to the current. The implementation of this sediment transport model is shown in listing B.3.

Model justification

The combination of the Meyer-Peter-Müller and Soulsby sediment transport formulation is well suited for this study due to its simplicity and easy implementation in an offline Python function. As was mentioned in the previous section, sediment transport models are generally empirical and require calibration. That is why care must be taken in the decision of the sediment transport models when they are compared between two different models. They should be effective but based on the same physical principles.

Meyer-Peter and Müller (1948) accepts intra-wave bed shear stresses for detailed, but simple and intuitive, bed load transport modeling. The formulation by Soulsby (1997) builds on the same formula and principles as Meyer-Peter-Müller but is specifically adapted to wave-averaged inputs, making it compatible with phase-averaged models such as FINEL-SWAN. Therefore, the combination of the original Meyer-Peter-Müller formulation with the Soulsby adaptation creates a meaningful comparison between phase-resolving and phase-averaged sediment transport modeling approaches.

Bed level changes

To compute the initial bed level changes from the sediment fluxes, an Exner-type equation is used:

$$(1 - n_p)\frac{\partial z_b}{\partial t} + \frac{\partial q_x}{\partial x} + \frac{\partial q_y}{\partial y} \tag{5.14}$$

This takes the spatial gradients of the sediment fluxes and uses them to update the bed levels over time. The time frame of the morphological computation can not be too long (maximum in the order of hours to one day) because morphodynamics and hydrodynamics form a feedback system that affects one another. When the sediment fluxes contain some sharp spatial gradients (noise), a Gaussian filter can be applied to smooth them out before processing with the Exner equation.

5.3. Comparison of model hydrodynamics

This section presents the results of the wave transformation and flow patterns induced by an obliquely incident wave climate on a coast with a dredged navigation channel. This section aims to assess how the presence of the channel affects wave propagation and flow patterns along the coast.

Before displaying the results, the model runtimes for the hydrodynamic simulations were measured and are shown in Table 5.5. The SWAN-FINEL run was approximately 4 times faster running on 16 cores compared to XBeach running on 32 cores. Both model runs remained under 12 hours.

The results are structured as follows. First, the results regarding wave propagation patterns from XBeach and SWAN-FINEL are presented. After that, flow patterns predicted by both models are presented and compared.

Model	Runtime	Cores used
SWAN-FINEL	3 hours 12 minutes	16
XBeach non-hydrostatic	11 hours 45 minutes	32

Table 5.5: Model runtimes for sediment transport simulations.

5.3.1. Wave propagation

A spatial plot of the significant wave height H_{m0} resulting from both models is shown in Figure 5.4.

First of all, the channel refraction can very clearly be observed in both plots. In both models, the refraction pattern that arises has a very similar shape and quantity. The wave heights inside that channel are lower, and they become lower the further onshore the waves propagate. This makes sense from the formulation of the critical angle Equation (2.14). Towards the shore, the depth ratio between the channel and its surroundings increases, increasing the critical channel and allowing fewer waves to pass.

On the southern side of the channel, a shadow zone would be expected due to waves not being able to pass. Both models show this shadow zone with wave heights of approximately 1 meter. The shape and size of the shadow zones are very comparable in both models.

Waves appear to propagate inside the channel more in SWAN-FINEL compared to XBeach, where wave heights inside the channel are almost zero from 1000 m towards the east. In SWAN-FINEL, some wave rays appear to end up deep inside the channel, as their wave energy is not distributed along the crest.

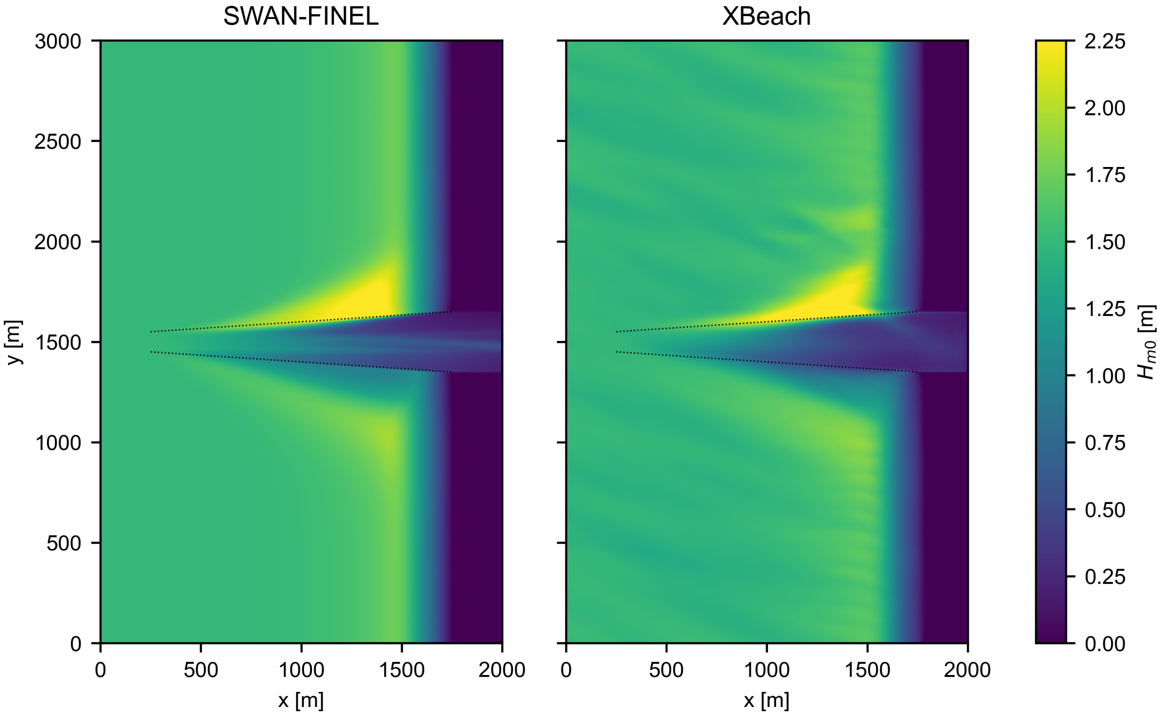

Figure 5.4: Comparison of significant wave height H_{m0}

In Figure 5.5 the significant wave height is plotted along y=500 m. This transect is chosen because in this location it is easy to observe how the waves and flows develop without the influence of the channel. This transect will be referenced frequently in the rest of this study. Both models show shoaling and wave breaking. The waves in SWAN-FINEL are slightly higher (1.93 m) compared to XBeach (1.88 m) when they break, and they also break a little further offshore. This could impact the longshore current location and magnitude.

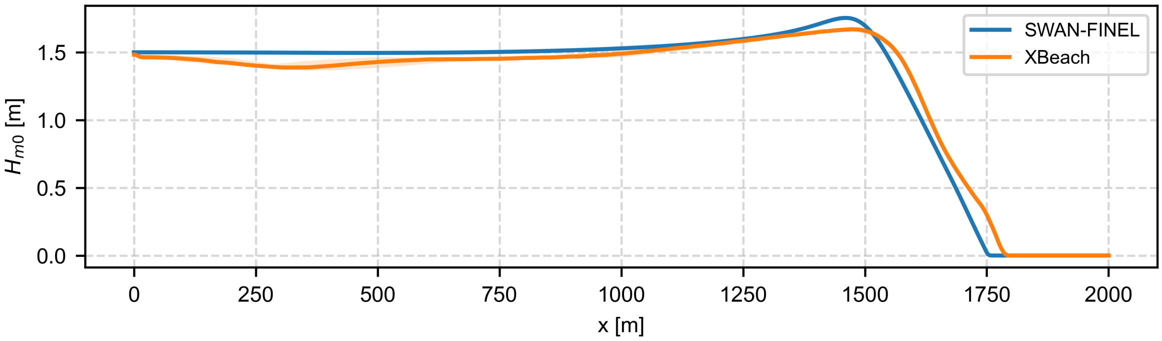

Figure 5.5: Transcect of significant wave height H_{m0} in y=500 m

Figure 5.6 shows the significant wave height along the breaker line at x=1500 m. The outer edges of the channel are plotted as grey lines. Both models show very comparable results; the wave heights in the refraction part are very similar. Only on the southern (or lee) side of the channel are wave heights in FINEL slightly higher. Some waves managed to propagate to the middle of the channel in the FINEL results, where the waves in XBeach are slightly lower. On both sides of the channel, where the refraction effects don't play a role, the wave heights are very similar again.

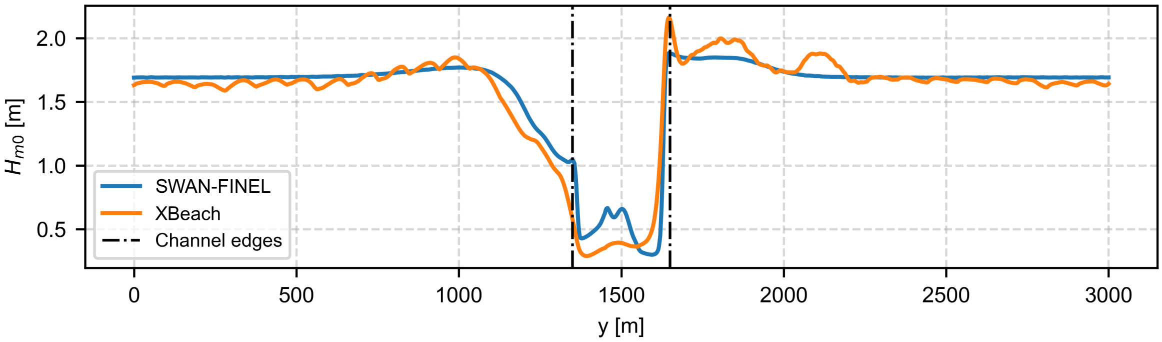

Figure 5.6: Transect of significant wave height H_{m0} in $y =$ 1500 m

In Figure 5.7 the wave directions in the domain from SWAN are shown between 180° (waves from the south) and 360° (waves from the north). This plot displays the mean wave direction, although in the model, the directions are distributed over a directional spectrum.

All over the western boundary, waves arrive at an angle of 290 degrees. Wave angles gradually decrease as waves refract as they propagate towards the shore. At the northern side of the channel, waves refract over the channel slope and slowly turn northwards. The area in which wave directions are affected by the refraction over the channel slope increases landward. On the southern side of the channel, waves also refract over the channel slope, turning further southward. However, as they leave the channel slope towards the beach, they quickly change direction again towards the shoreline. Inside the channel inlet, waves are refracted towards the channel slopes, almost directed purely northward and southward as they reach the shoreline inside the channel.

The green line shows the location at which $\phi_c = \phi$, according to the theoretical solution based on Equation (2.14). From this line eastwards, waves with ϕ_m and T_p are expected to refract over the channel slope and not cross the channel.

5.3.2. Flow

In XBeach, flow velocities are inherently computed as part of the shallow water equations, which form the basis of the model. Flow velocities are computed instantaneously (intra-wave), after which they are averaged over time. In contrast, SWAN must be coupled with a separate hydrodynamic model,

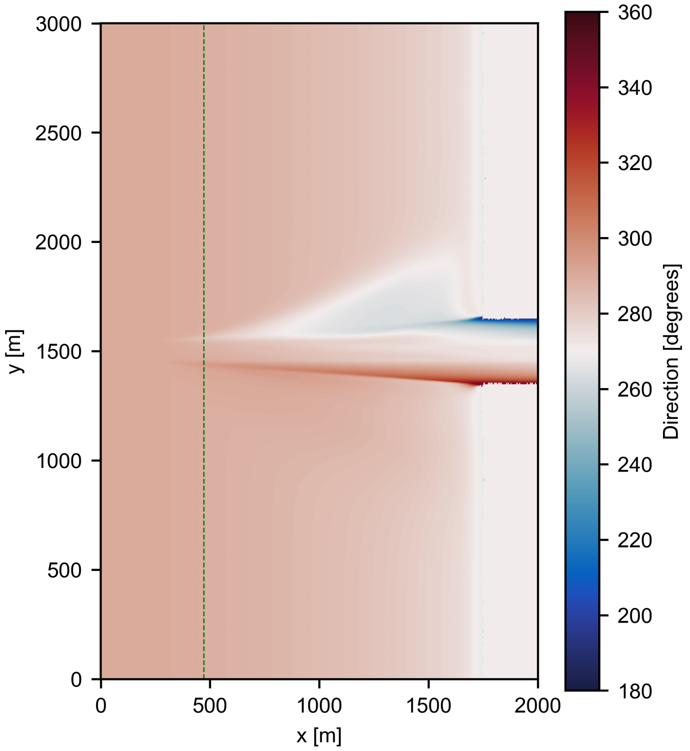

Figure 5.7: Wave directions from SWAN. The green dashed line shows the location of the theoretical prediction of the start of channel refraction at $x = 472\,\mathrm{m}$.

such as FINEL, to compute flow fields, and the time-averaged flow velocities are computed from wave-averaged quantities. The results shown from both models are *depth-averaged* flow velocities. Also, they are Eulerian flow velocities, meaning the velocities are observed from a static viewpoint.

Hydrodynamic processes in FINEL

Stokes drift and wave rollers can create an onshore mass flux that induces an offshore-directed Eulerian return flow. In FINEL v8.0, these processes can be included and are computed with the wave energy, celerity, and water depth Equations (3.13) and (3.14). The computed flow velocities Equations (3.6) to (3.8) are then updated with the return flow. In this section, the importance of including this process is evaluated.

Figure 5.8 displays how the different mass-flux processes (due to Stokes drift and wave rollers) contribute to the cross-shore and alongshore flow velocities in a transect at $y = 500\,\mathrm{m}$. The RMSE of each velocity compared to the XBeach results in this particular transect is shown in Table 5.6.

In the cross-shore direction, both wave roller and Stokes drift-induced mass flux induce a return flow. The return flow from Stokes drift is much higher than the return flow from wave rollers. Including Stokes drift mass-flux greatly increases the RMSE for the cross-shore flows from 0.0533 to 0.0333. When the wave roller is also included, the RMSE slightly reduces as the flow velocities now slightly dip below the XBeach flow velocities.

In the alongshore direction, the mass flux has very little influence on the flow. Since the mass flux has the same direction as the waves, it mainly has an effect in the cross-shore direction. The RMSE between the different flow velocities is very small, and the choice will be made based on the cross-shore flow distribution.

Purely based on the RMSE, only including Stokes drift mass-flux would be the best choice. However, the RMSE of including both wave roller and Stokes drift mass flux is very close to only including Stokes drift. Physically, it makes more sense to include both processes if this doesn't have a large negative impact on the RMSE. Therefore, for the remainder of the study, the FINEL results will include both Stokes drift and wave roller mass flux.

	RMSE to XBeach	
Mass-flux processes included in FINEL	cross-shore	alongshore
None	0.0533	0.0595
Wave roller	0.0486	0.0550
Stokes drift	0.0333	0.0551
Wave roller + Stokes drift	0.0340	0.0496

Table 5.6: RMSE of the inclusion of different processes compared to the XBeach non-hydrostatic flow results in transect at $y = 500\,\mathrm{m}$

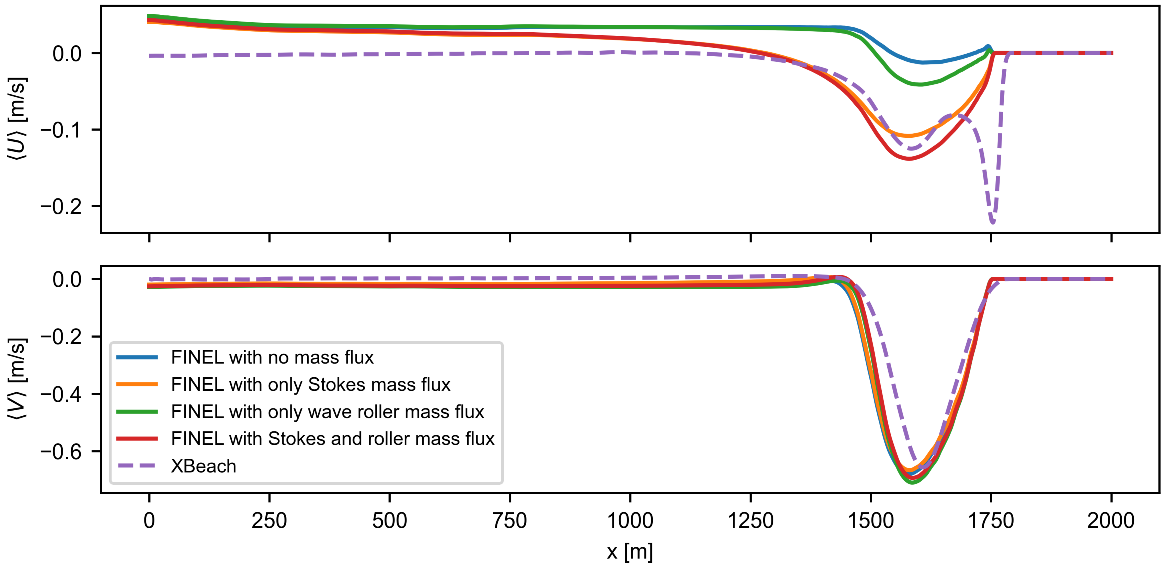

Figure 5.8: Comparison of mean cross-shore and alongshore flow velocities between XBeach and FINEL with different mass-flux contributions included: No mass flux, only Stokes drift mass flux, only wave roller mass flux, and combined Stokes and wave roller mass flux.

Flow patterns

Figure 5.9 presents a vector plot of the mean flow velocities obtained from both models, on a background of the significant wave height H_{m0}. FINEL includes mass fluxes due to Stokes drift and wave rollers.

In both models, a longshore current directed southward develops as a result of wave breaking under oblique incidence. The magnitude and cross-shore position of this current appear similar between the models. The most noticeable differences between the models are found in the flow patterns around the refracted region. In the nearshore zone, both models produce similar results: a northward-directed current originates from the refracted area and travels alongshore. Where it meets with the southward longshore current, the flow is redirected offshore, which is captured by both models.

Further offshore, differences between the models become noticeable. Around $x = 1000\,\mathrm{m}$, FINEL predicts that the offshore-directed current turns southward, forming a circulation current between the refracted area and the region immediately north of it. In contrast, XBeach shows this offshore current dissipating as it curves around the refracted zone, without forming a distinct recirculation pattern.

Near the beach and along the channel flanks, both models exhibit strong cross-shore currents directed into the channel. These inflows are of comparable magnitude and structure.

On the southern (lee) side of the channel, flow velocities are relatively low in both models. In this region, the predicted patterns are in strong agreement. Within the shadow zone with reduced wave energy, northward-directed currents develop. Moving further southward, out of this zone, these currents weaken and eventually reorient into a southward longshore flow.

Another interesting pattern can be observed near the beach, but away from the channel. XBeach predicts strong flows that are directed offshore, whilst SWAN-FINEL shows flows that are weakly directed offshore.

A small northward-directed current is observed in the northern half of the FINEL domain. This flow originates from the boundary implementation and persists near the northern boundary, extending weakly into the region of interest.

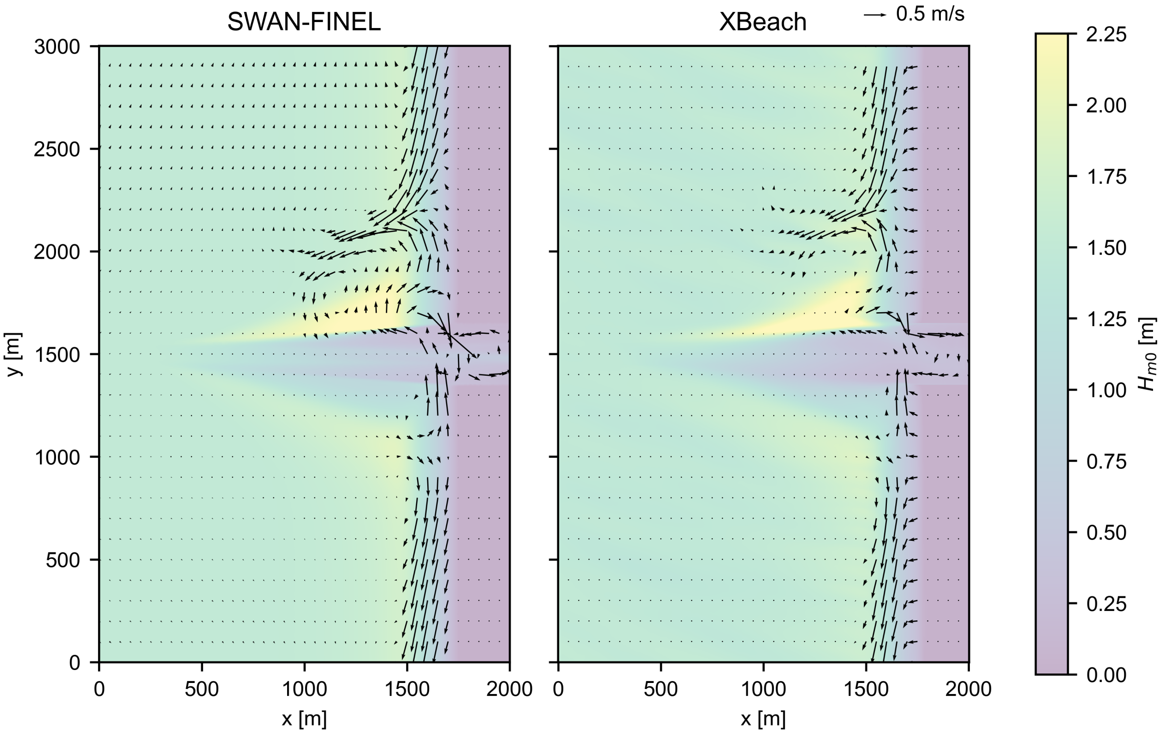

Figure 5.9: Vector plot of mean flows in SWAN-FINEL and XBeach. Colors indicate wave heights.

Alongshore flow

The mean depth-averaged flows in the y-direction $\langle V \rangle$ resulting from both models are visualized in a spatial plot in Figure 5.10. The boundary effects are visible in SWAN-FINEL, resulting in a slight northward-directed flow in the northern half of the domain.

North of the channel, the circulation current is again observed. These figures demonstrate how the longshore current turns around the northward current from the refracted area. In SWAN-FINEL, this current extends to the channel edge, significantly farther than in XBeach. FINEL predicts a large area of northward flow north of the channel, whereas in XBeach, the northward currents are confined to a more concentrated area but show a higher magnitude. In the nearshore zone, at the channel edges, large currents are observed towards the channels in both models.

Figure 5.11 displays the alongshore current in the absence of channel influence. Both currents display a very similar shape and location, although the current in FINEL is of slightly higher magnitude. Additionally, FINEL shows a small northward (positive) longshore current around $x = 1400\,\mathrm{m}$, which is absent in XBeach.

Cross-shore flow

The mean cross-shore flows ($\langle U \rangle$) resulting from both models are shown in a spatial plot in Figure 5.12. This plot provides insight into the offshore and onshore flow patterns and magnitude generated by

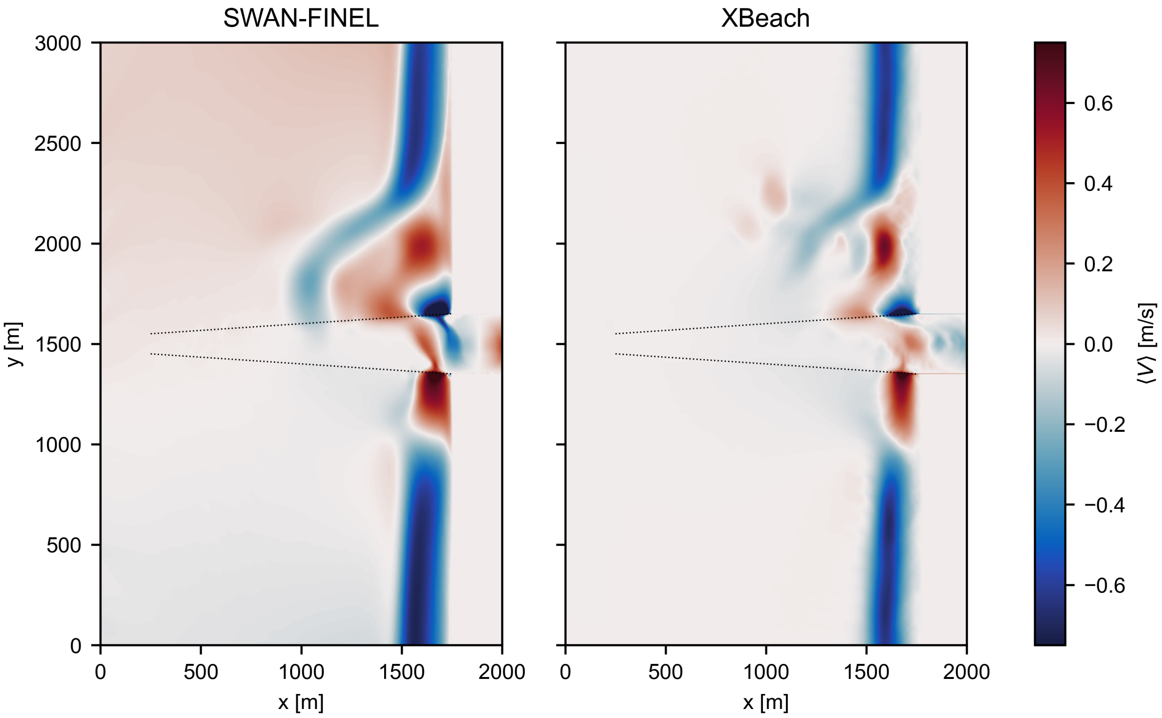

Figure 5.10: Spatial comparison plot of mean flow velocities in x-direction ($\langle V \rangle$)

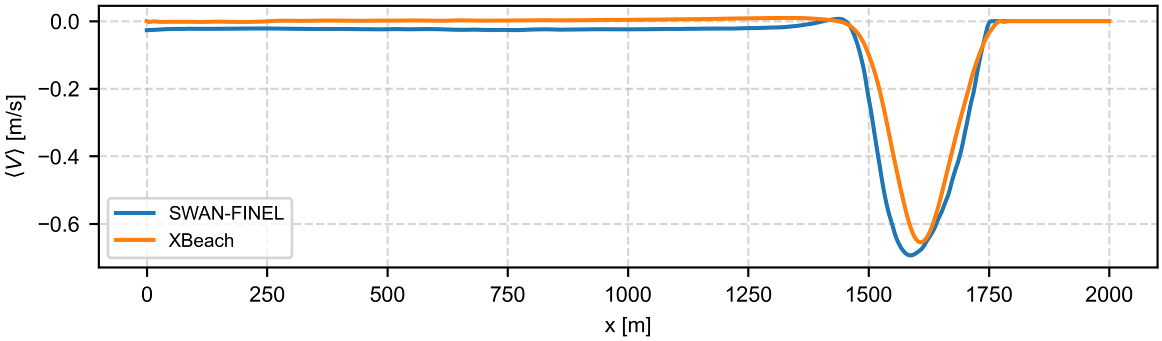

Figure 5.11: Plot of the mean cross-shore flow velocities ($\langle V \rangle$) in a transect at $y = 500\,\mathrm{m}$ - averaged over 20 m alongshore.

wave-induced processes and their interaction with the channel. Boundary effects result in a slight onshore-directed flow from the western boundary in SWAN-FINEL.

Immediately north of the channel, an onshore current is observed in both models. In SWAN-FINEL, this current extends far offshore - up to $x = 1000\,\mathrm{m}$ - whereas in XBeach, this flow is localized in the nearshore zone. Slightly further north, a strong offshore-directed current is observed on the northern side of the channel around $x = 2000\,\mathrm{m}$. In both models, this flow has a very comparable shape, but in FINEL, the offshore flow appears to have a slightly larger magnitude.

South of the channel, both models indicate weak onshore flow with very comparable magnitude and location. Inside the channel inlet, another circulation current appears to exist in both models, but in an opposing direction.

The transect plotted in Figure 5.13 shows that the models agree on the general shape of the cross-shore current profile. Both models predict an offshore undertow flow of approximately $-0.15\,\mathrm{m/s}$ due to mass flux compensation (see Appendix F for a comparison of cross-shore flows in FINEL without Stokes drift mass flux compensation).

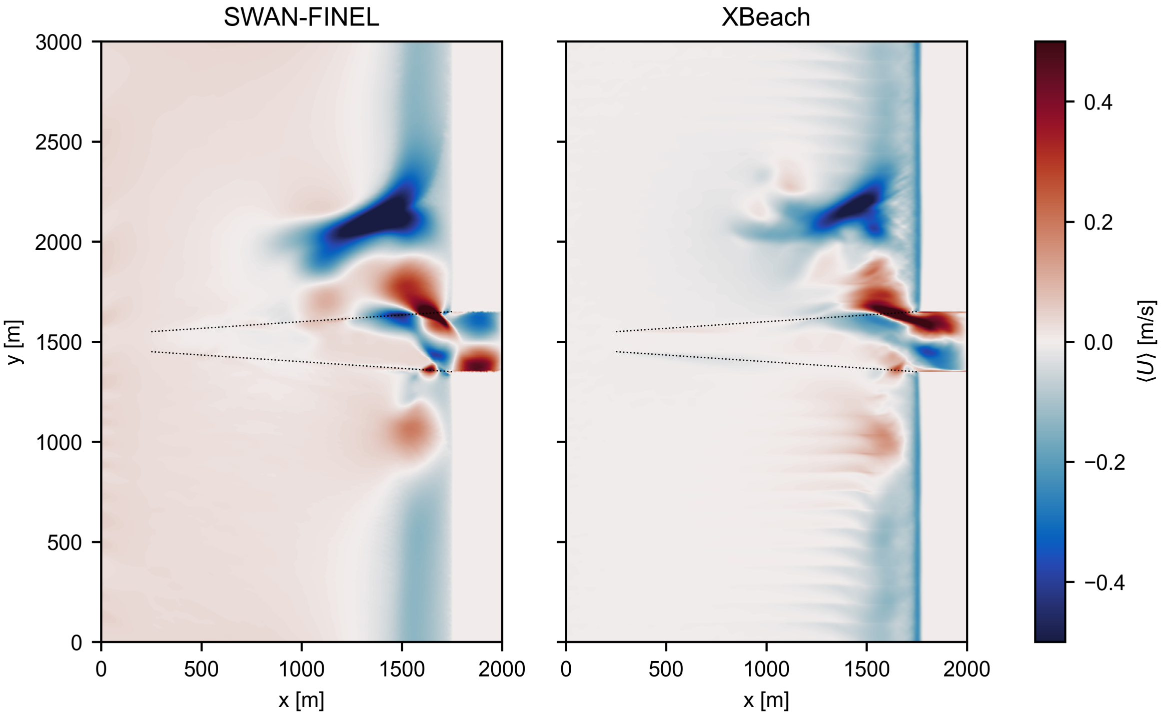

Figure 5.12: Spatial comparison plot of mean flow velocities in x-direction ($\langle U \rangle$)

Two differences are observed between the two models. The first is a gradually decreasing weak onshore flow at the western boundary in FINEL, whereas in XBeach, the flow velocity at the boundary is zero. XBeach predicts a large offshore flow of $-0.20\,\mathrm{m/s}$ in the swash zone, peaking at $x = 1750\,\mathrm{m}$. In FINEL, this flow is not present; instead, the velocity reduces to zero at the waterline.

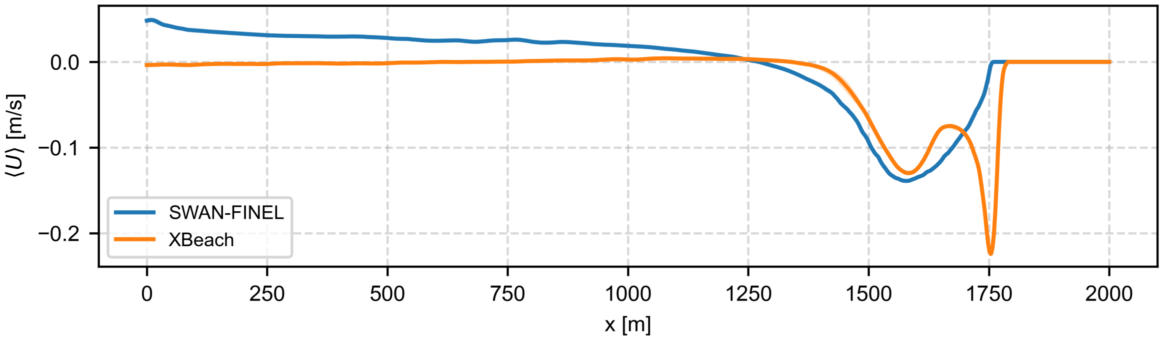

Figure 5.13: Plot of the cross-shore flow velocities ($\langle U \rangle$) in a transect at $y = 500\,\mathrm{m}$ - averaged over 20 m alongshore.

5.4. Comparison of model morphodynamics

This section presents the results of the sediment transport computations resulting from the wave and flow computations in SWAN-FINEL and XBeach. The analysis focuses on the direction, magnitude, and spatial distribution of bed shear stresses and bed-load sediment fluxes. By comparing the predicted fluxes, the goal is to evaluate how each model predicts sediment paths in and around the channel, and to estimate effects like channel infilling, longshore transport gradients, and onshore or offshore sediment redistribution.

5.4.1. Bed shear stresses

The bed shear stresses are a very important parameter for bed load sediment transport computations, like the Meyer-Peter-Müller transport formulation. This is why the bed-shear stresses resulting from the model are analyzed first. Bed shear stress is nonlinearly proportional to the flow velocity: $\tau_b \propto u^2$.

Bed shear patterns

The bed shear stress spatial patterns from both models are shown in Figure 5.14 in vector plots overlaid on the significant wave heights. All bed shear stresses higher than 2.0 N/m^2 are clipped to 2.0 N/m^2 to improve readability. The SWAN-FINEL results displayed here are not readily obtained from the model, since the only output from FINEL is the *current* bed shear stress τ_c. When both waves and currents are present, the *mean* bed shear stress is slightly increased (Equation (5.3)).

Both models display similar patterns in the bed shear stress compared to the flow velocities. XBeach displays quite different results in the cross-shore direction, however. In the outer surf zone, bed shear stresses are directed slightly onshore, whereas bed shear stresses in SWAN-FINEL are only directed offshore.

The offshore current north of the refracted area is also represented in the bed shear stresses in both models, although the circulation current observed in SWAN-FINEL is not as well represented in the bed shear stress patterns in XBeach. The skin friction for bed shear stress is dependent on depth, which is why currents in deeper water result in lower bed shear stresses.

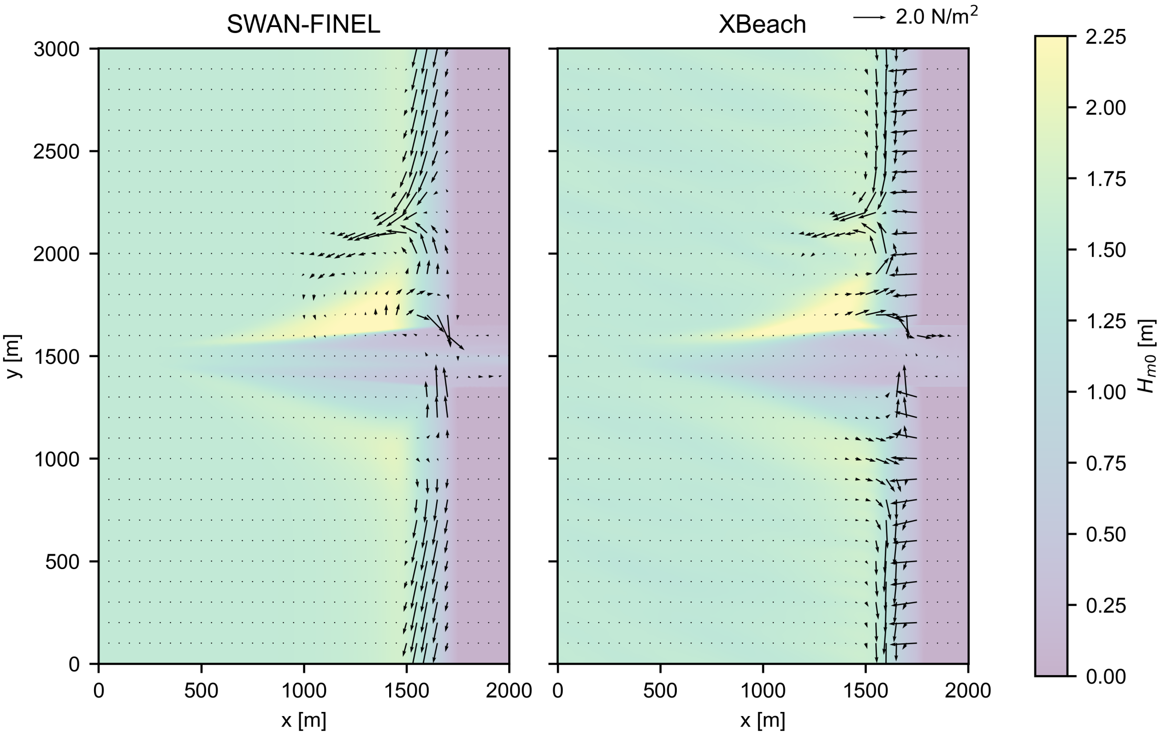

Figure 5.14: Comparison of spatial bed shear stresses in SWAN-FINEL and XBeach. Bed shear stress magnitudes are clipped to 2.0 N/m^2 for readability. Colors indicate wave heights.

Alongshore bed shear stress

A spatial plot of the y-component of the mean bed shear stress ($\tau_{m,y}$) resulting from both models is shown in Figure 5.15. In the nearshore zone, at the channel edges, the strong currents into the channel are also represented in the bed shear stresses. To the north of the channel, a northward bed shear stress is present in both models. In XBeach, this region of bed shear stress is more confined and of higher magnitude; in SWAN-FINEL, this area of northward-directed bed shear stress is more spread out. To the south of the channel, the bed shear stress patterns and magnitudes in both models are very comparable.

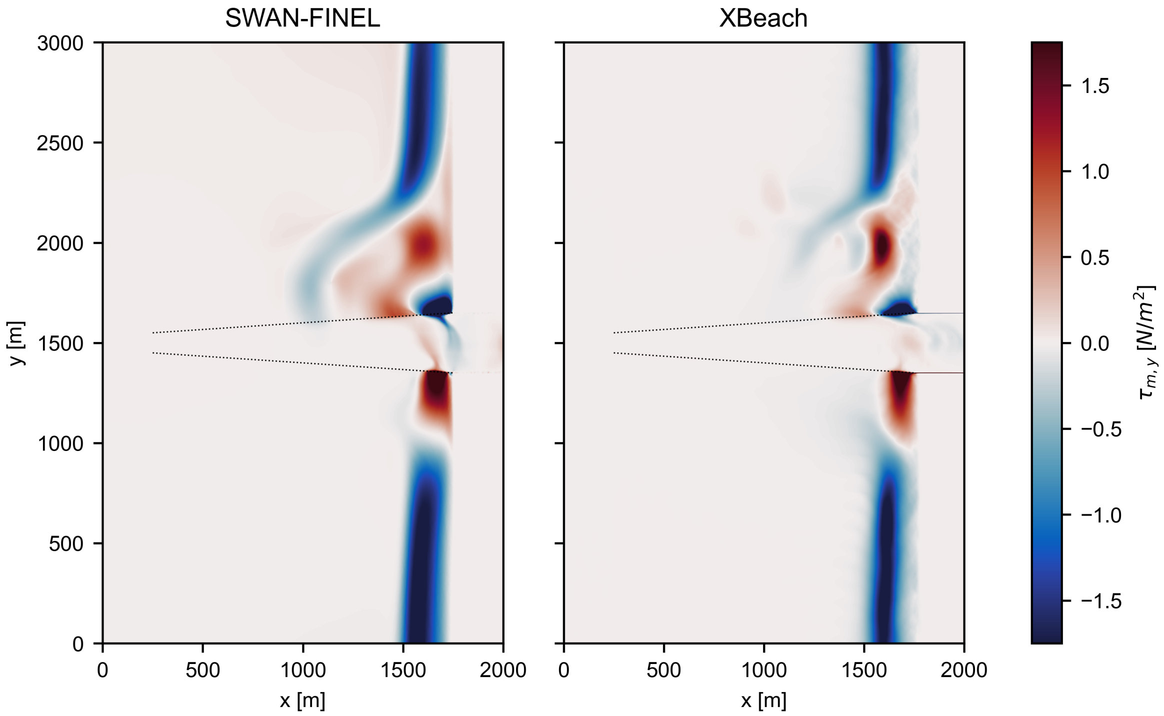

Figure 5.15: Spatial distribution of bed shear stress in the y-direction.

The transect in Figure 5.16 shows that both models agree on the location and general shape of the shear stress distribution in the y-direction. A distinct minimum occurs around $x = 1650–1700$ m, with values reaching approximately $-2\,\mathrm{N/m^2}$. XBeach predicts a slightly stronger and narrower minimum compared to SWAN-FINEL. The plot also shows how the mean bed shear stress is indeed higher under combined currents and waves compared to currents alone.

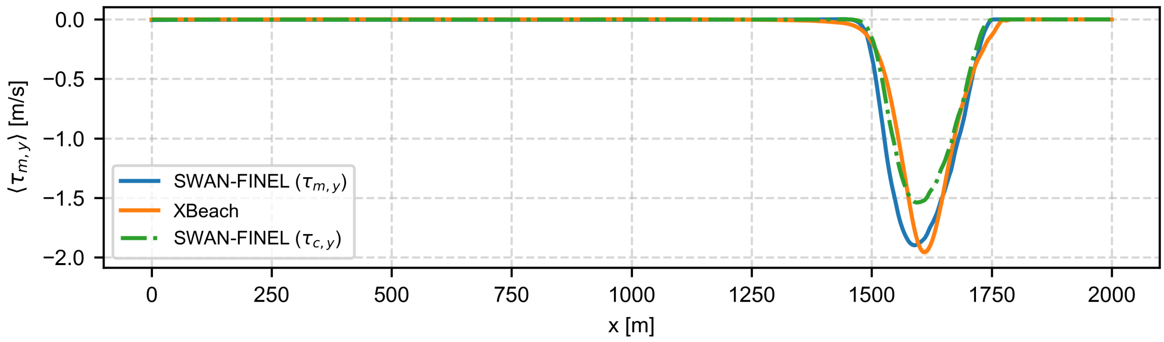

Figure 5.16: Transect of bed shear stress in the y-direction at $y = 500\,\mathrm{m}$ - averaged over 20 m alongshore.

Cross-shore bed shear stress

The x-component of the mean bed shear stress ($\tau_{m,x}$) from both models are displayed in a spatial plot of $\tau_{m,x}$ (Figure 5.17) and a cross-shore transect at $y = 500\,\mathrm{m}$ (Figure 5.18).

The spatial patterns in Figure 5.17 are quite comparable, although onshore-directed bed shear stresses are present in the outer surfzone in XBeach, and not in SWAN-FINEL. In the swash zone, large offshore-directed bed shear stress is observed in XBeach, which is not present at all in SWAN-FINEL.

Whilst the mean flow in x-direction was only directed offshore, XBeach displays a partly onshore-directed bed shear stress over the cross-shore in Figure 5.18. SWAN-FINEL only exhibits offshore-directed bed shear stresses in the cross-shore transect.

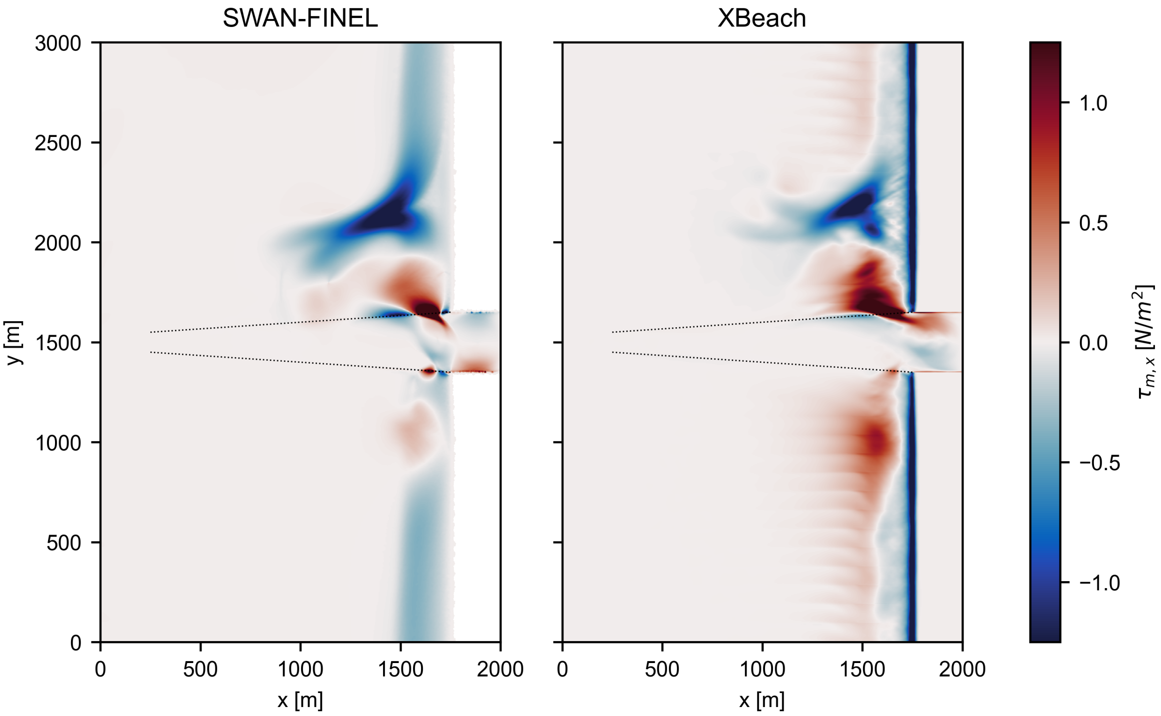

Figure 5.17: Spatial distribution of bed shear stress in the x-direction.

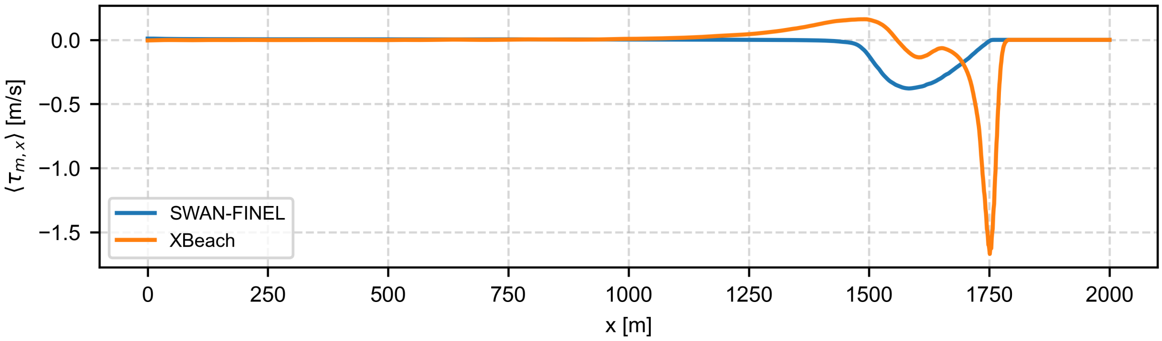

Figure 5.18: Transect of bed shear stress in the x-direction at $y = 500\,\mathrm{m}$ - averaged over 20 m alongshore.

Bed shear stresses due to waves

The bed shear stresses due to waves are an important factor for the sediment transport. In XBeach, waves are included in the sediment transport computations when an intra-wave sediment transport model is used. In FINEL, waves must be taken into account in a sediment transport model externally. Here, a comparison is made between the computed bed shear stresses due to waves from SWAN-FINEL and XBeach.

In Figure 5.19, the amplitude of the bed shear stresses due to waves is plotted. From SWAN-FINEL, the wave orbital velocity is obtained from the model output, from which the bed shear stress can be computed using Equation (5.2). From XBeach non-hydrostatic, the root mean square of the bed shear stress is computed, which is multiplied by $\sqrt{2}$ to obtain a representative τ_w amplitude for comparison. Figure 5.20 shows the wave-induced bed shear stresses in a transect at $y = 500\,\mathrm{m}$. The models predict a very comparable bed shear stress due to waves, although the peak of τ_w in SWAN-FINEL is slightly more offshore than the peak in XBeach.

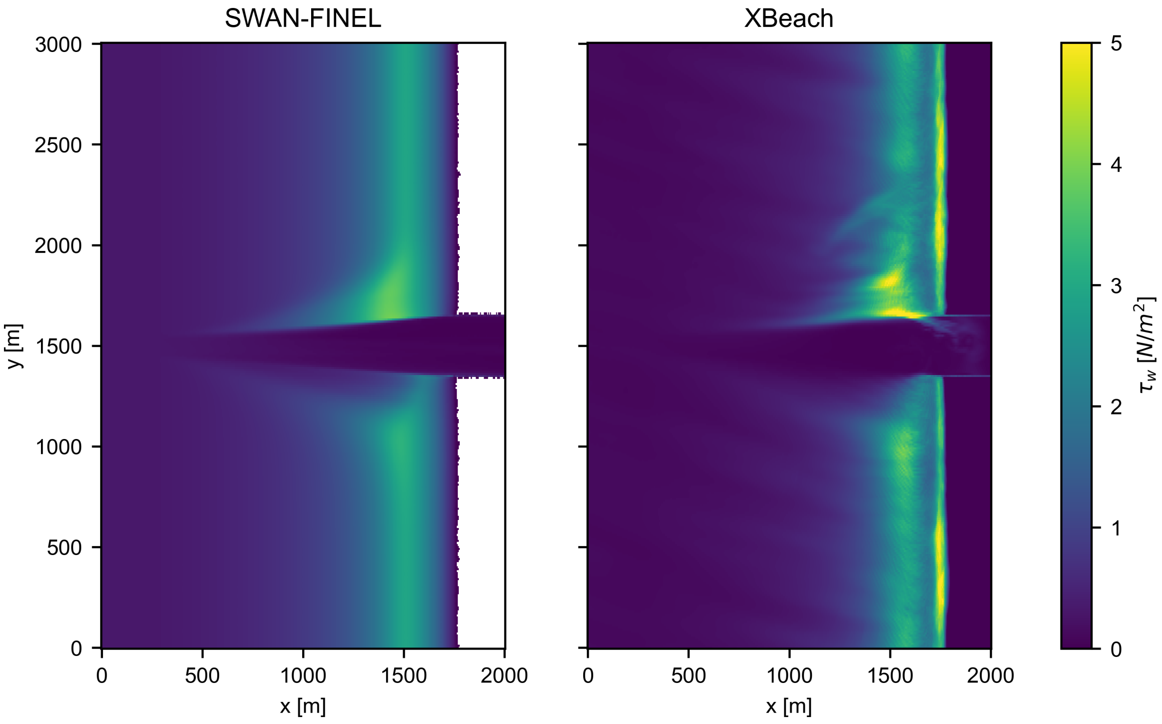

Figure 5.19: Spatial distribution of wave-induced bed shear stress amplitude (τ_w).

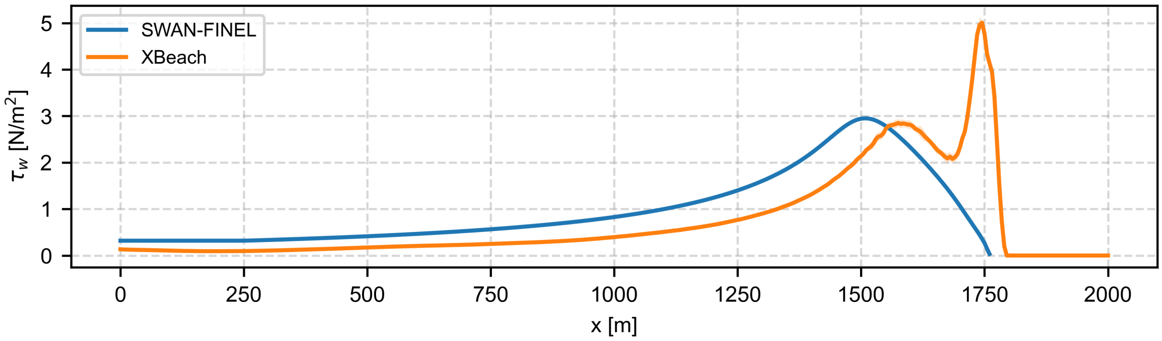

Figure 5.20: Transect of root mean squared amplitude of the wave-induced bed shear stress (τ_w) at $y = 500\,\mathrm{m}$.

5.4.2. Bed-load fluxes

The bed shear stresses computed by the models are used in the sediment transport formulations described in Section 5.2.3, based on the Meyer-Peter-Müller transport model, to compute bed-load sediment fluxes. The implementation differs slightly between the two models:

- **SWAN-FINEL**: Time-averaged (mean) bed shear stresses are used as input to the transport model proposed by Soulsby (1997), yielding a time-averaged sediment flux: $\langle\Phi\rangle = f(\theta_m, \theta_w, \theta_c)$.
- **XBeach**: Instantaneous (intra-wave) bed shear stresses are input to the transport model by Meyer-Peter and Müller (1948), and the resulting fluxes are subsequently averaged over time: $\langle\Phi\rangle = \langle f(\theta, \theta_c)\rangle$.

Figure 5.21 presents spatial maps of the dimensionless sediment fluxes obtained from both SWAN-FINEL and XBeach. A large difference between the results of the two models is that XBeach displays more onshore-directed transport in the surf zone, even more significant than the onshore bed shear stress. In SWAN-FINEL, the transport in a large part of the surf zone is offshore-directed. Another difference is that the offshore-directed transport current north of the refracted area is more pronounced and stretches further offshore in SWAN-FINEL compared to XBeach.

Near the channel edges, transport fluxes towards the inside of the channel are observed, signifying channel infilling over time. Inside the refracted area, fluxes in SWAN-FINEL are directed mostly northward, whilst in XBeach, they are directed mostly onshore. South of the channel, transport patterns are similar in the alongshore direction but oppositely directed in the cross-shore direction.

XBeach exhibits strong transport fluxes in the swash zone, which are not present in SWAN-FINEL.

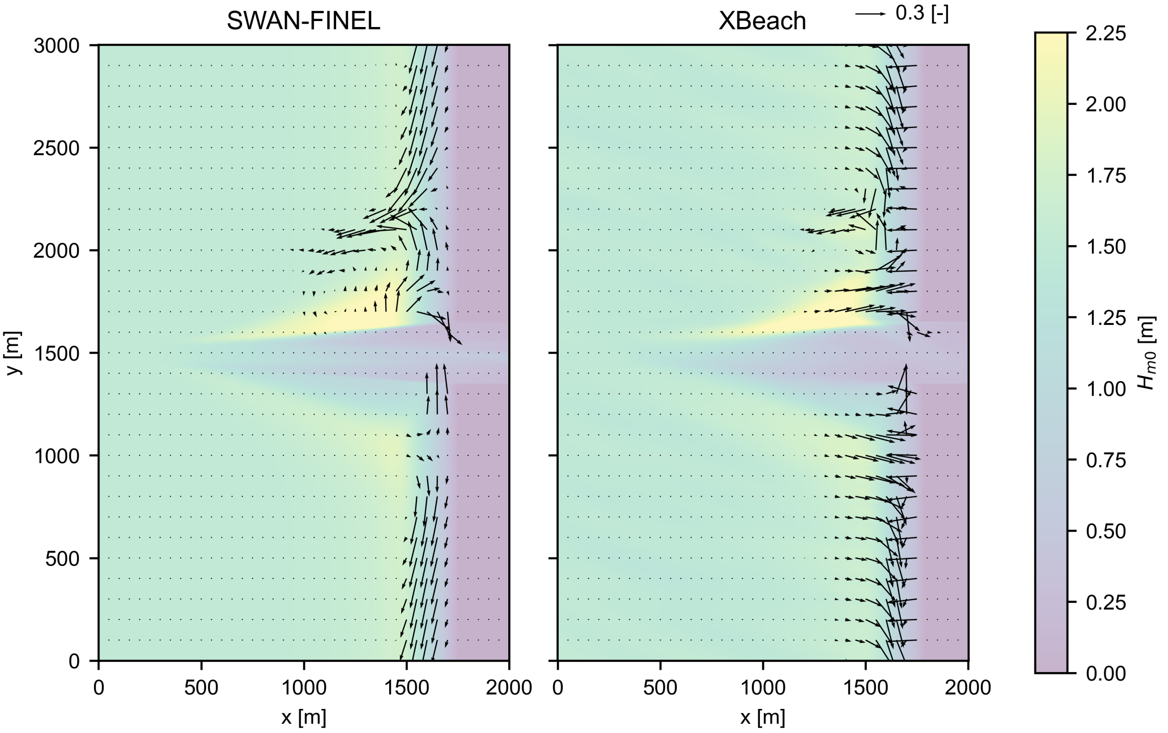

Figure 5.21: Spatial plot of dimensionless sediment bed-load flux Φ_b with direction and magnitude from both models. Colors indicate wave heights.

Alongshore sediment fluxes

The mean dimensionless transport fluxes in the y-direction are given in a spatial plot in Figure 5.22 for both models. It can be observed that the alongshore sediment transport in XBeach is more confined to the nearshore zone compared to SWAN-FINEL. The northward-directed current north of the channel is more concentrated in XBeach. Apart from that, the sediment flux patterns and magnitude among both models are very comparable.

In a transect at $y = 500\,\mathrm{m}$, the alongshore sediment flux is plotted in Figure 5.23. The figure shows how the alongshore transport in both models is comparable, but not equal. The transport in XBeach is more peaked with a narrower shape and a lower minimum. The peak of the transport in SWAN-FINEL is located slightly more offshore compared to XBeach.

Cross-shore sediment fluxes

The dimensionless bed load fluxes in the x-direction are plotted in Figure 5.24. The direction of sediment fluxes in the cross-shore direction is opposite in the majority of the domain. In XBeach, sediment transport is mostly directed offshore in the surf zone. In SWAN-FINEL, this is directed onshore. Again, sediment fluxes in XBeach are more confined to the nearshore zone to about $x = 1250\,\mathrm{m}$, whereas in SWAN-FINEL they stretch farther offshore up to around $x = 1000\,\mathrm{m}$.

The differences between the cross-shore transport in SWAN-FINEL and XBeach are more easily quantifiable in a cross-shore transect, see Figure 5.25. XBeach predicts an onshore-directed sediment transport in a large part of the surf zone. In the swash zone, the predicted bed-load flux is very large

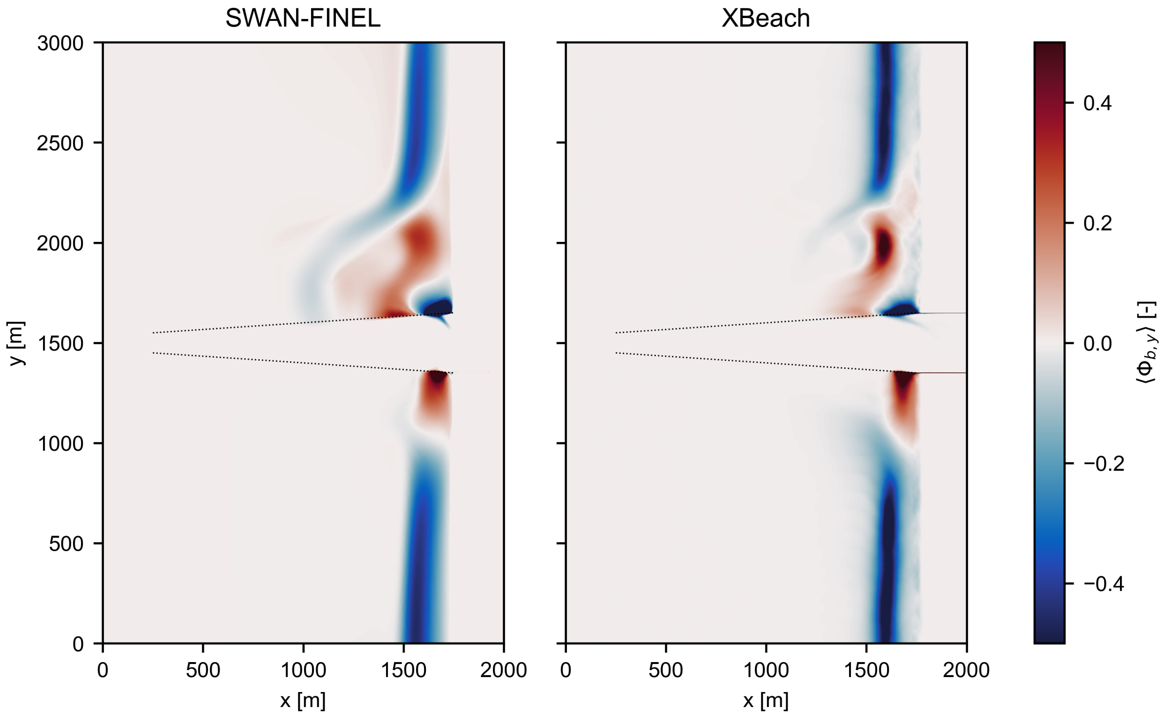

Figure 5.22: Spatial distribution of dimensionless sediment bed-load fluxes in y-direction ($\Phi_{b,y}$).

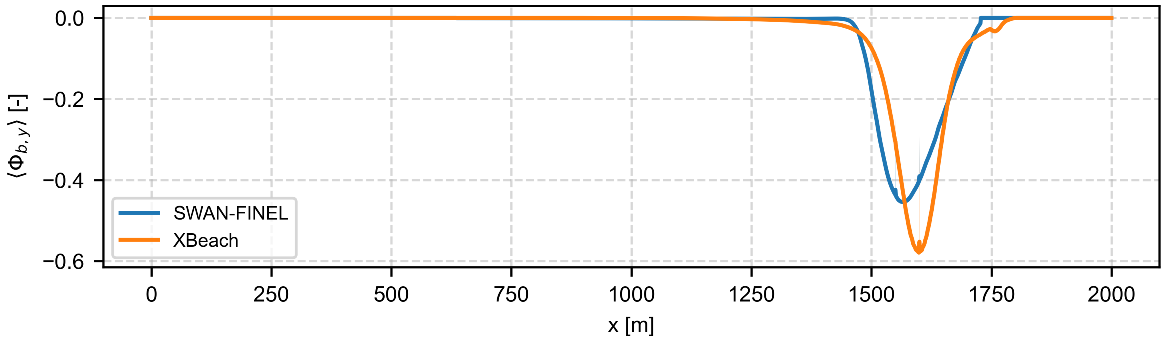

Figure 5.23: Dimensionless sediment bed-load fluxes in y-direction ($\Phi_{b,y}$) in a cross-shore transect at $y = 500\,\mathrm{m}$ - averaged over 20 m alongshore.

and offshore directed. The contrast with SWAN-FINEL is large, as it expects an offshore-directed sediment transport in a large part of the surf zone.

5.5. Effects on the channel and coast

This subsection aims to evaluate the impact of the predicted sediment transport patterns on the navigation channel. By comparing results from SWAN-FINEL and XBeach, differences in predicted sedimentation patterns are highlighted, providing insight into how model choice and wave-current interaction processes influence the channel and adjacent coastal region.

5.5.1. Longshore sediment transport gradients

To estimate the coastline response to the presence of the channel, the alongshore sediment transport is integrated over each cross-shore transect. The alongshore sediment transport is computed because gradients in alongshore sediment transport are the drivers of erosion and accretion along a coast. Positive gradients in the alongshore transport imply erosion, whereas negative gradients indi-

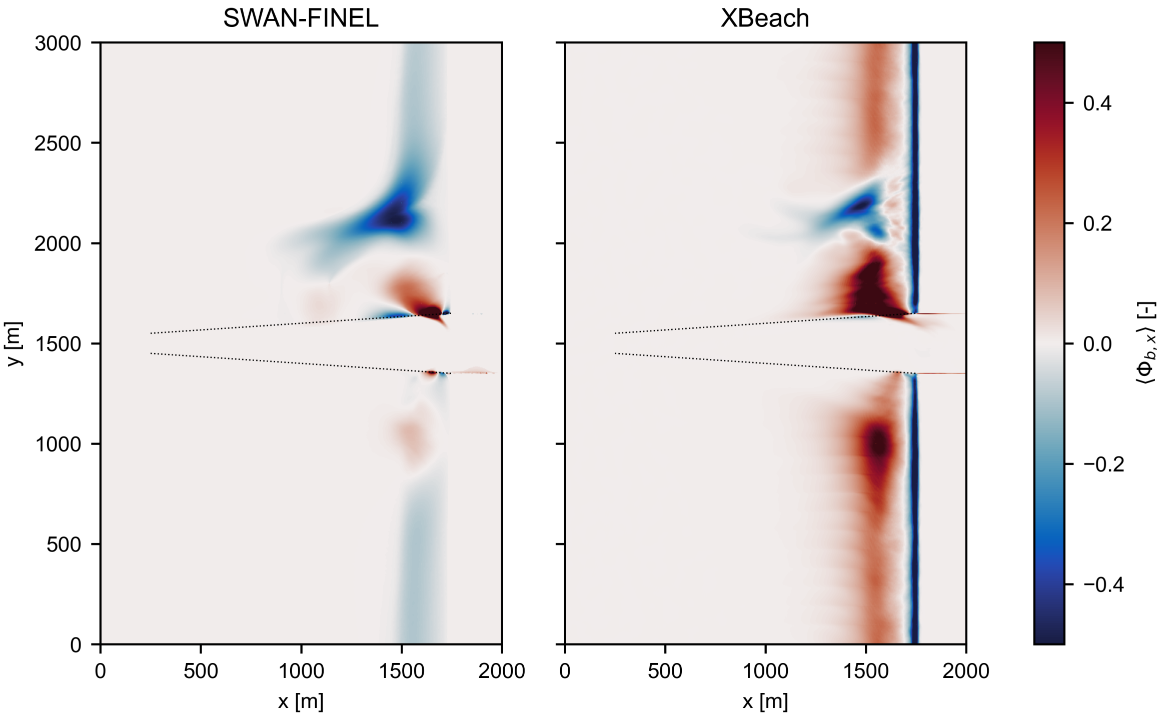

Figure 5.24: Spatial distribution of dimensionless sediment bed-load fluxes in x-direction ($\Phi_{b,x}$).

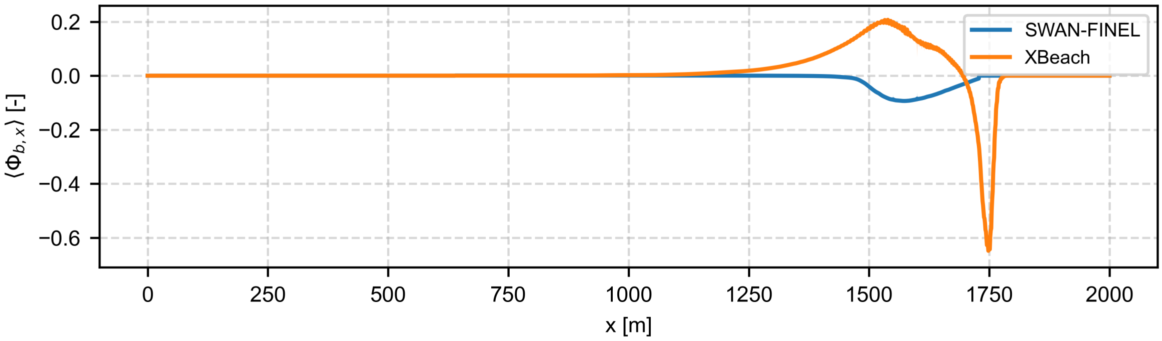

Figure 5.25: Dimensionless sediment bed-load fluxes in x-direction ($\Phi_{b,x}$) in a cross-shore transect at $y = 500\,\mathrm{m}$ - averaged over 20 m alongshore.

cate sedimentation. These gradients can be used to assess how the channel modifies the alongshore sediment budget.

To obtain the volumetric transport rates from the dimensionless bed load transport rates Φ_b, a factor is applied. The result is a sediment transport flux q_b in m^2/s:

$$q_b = \sqrt{\left(\frac{\rho_s}{\rho_w} - 1\right) g D_{50}^3} \cdot \Phi_b$$

The alongshore sediment fluxes are integrated over the cross-shore to obtain an estimate of the long-shore bed-load sediment volume $Q_{b,y}$:

$$Q_{b,y} = \int_{x=0}^{x=2000} q_{b,y} \, \mathrm{d}x$$

The predicted alongshore sediment transport volumes $Q_{b,y}$ between the two models can be compared in Figure 5.26. The longshore transport rates in the south of the domain (at $y = 0$) start southward and gradually increase toward the channel edge and change from negative to positive. At the southern channel edge, the longshore transport rates peak. The peak at the southern channel edge is slightly higher in XBeach (0.0262 m^3/s) compared to SWAN-FINEL (0.0167 m^3/s). Inside the channel, there is almost no sediment transport. At the northern channel edge, another peak in sediment transport arises, directed southward. In XBeach, this peak has a magnitude of 0.945 m^3/s, which is slightly lower than that in SWAN-FINEL (0.115 m^3/s). Further north, the alongshore transport rate stabilizes again, and inside the refracted area at $y = 1700$, the longshore transport is redirected northward (positive transport). Moving further toward the northern boundary, the influence of the channel refraction gradually weakens, and the longshore southward transport stabilizes.

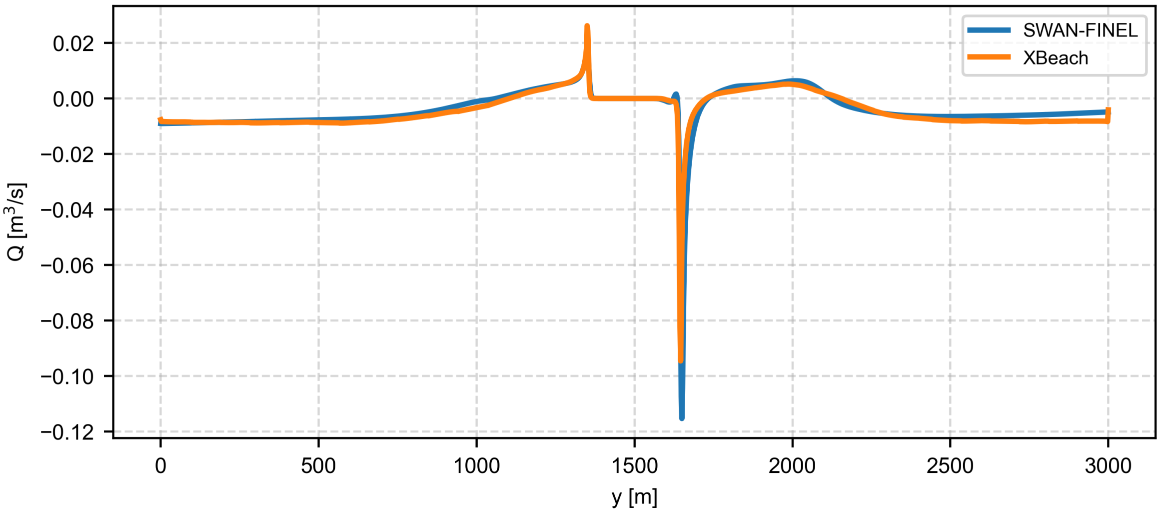

Figure 5.26: Integrated longshore sediment transport along the domain for both models.

Figure 5.27 displays the spatial alongshore sediment fluxes q_b in both SWAN-FINEL and XBeach, and also shows the longshore sediment transport with limits on the x-axis set between −0.01 m^3/s and 0.01 m^3/s to be able to see the details in the longshore transport better. Approximate areas with a positive gradient in the longshore transport are highlighted in red, implying erosion. The area highlighted in green is an area with a negative transport gradient where accretion is expected.

From the southern boundary ($y = 0$) up to approximately $y = 600$, the longshore transport rate is quite stable, indicating no erosion or accretion. The transport from both models is very comparable here. From $y = 600$ up to the channel edge at $y = 1350$, erosion is expected because of a positive gradient in sediment transport. Near the channel edge, the transport rate increases rapidly; this is where high erosion is expected. Inside the channel, the transport rate returns to zero with a very sharp gradient, implying strong accretion.

Near the channel edge, both models display a strong gradient towards the peak in southward transport at the northern channel edge, signifying strong accretion on the channel slope. From the northern channel edge up to $y = 2000\,\mathrm{m}$, a sharp positive gradient again indicates erosion. Where the positive and negative currents meet, the longshore current changes direction, causing a negative gradient in longshore transport, indicating accretion. In this area, the gradient in longshore transport by SWAN-FINEL is a bit sharper compared to XBeach. From approximately $y = 2500$ northwards, the longshore current has again stabilized. At the northern boundary, XBeach displays a stronger longshore transport compared to FINEL-SWAN, possibly due to boundary effects in SWAN-FINEL Figure F.1.

Figure 5.28 shows the difference in alongshore bed-load sediment transport rates between SWAN-FINEL and XBeach ($Q_{y,\mathrm{FINEL}} - Q_{y,\mathrm{XB}}$). The differences between the models stay mostly within a range of −0.025 m^3/s and 0.025 m^3/s. Considering that the computed stable longshore transport rate Q is in order 0.01 m^3/s, implies that the relative difference between the SWAN-FINEL and XBeach

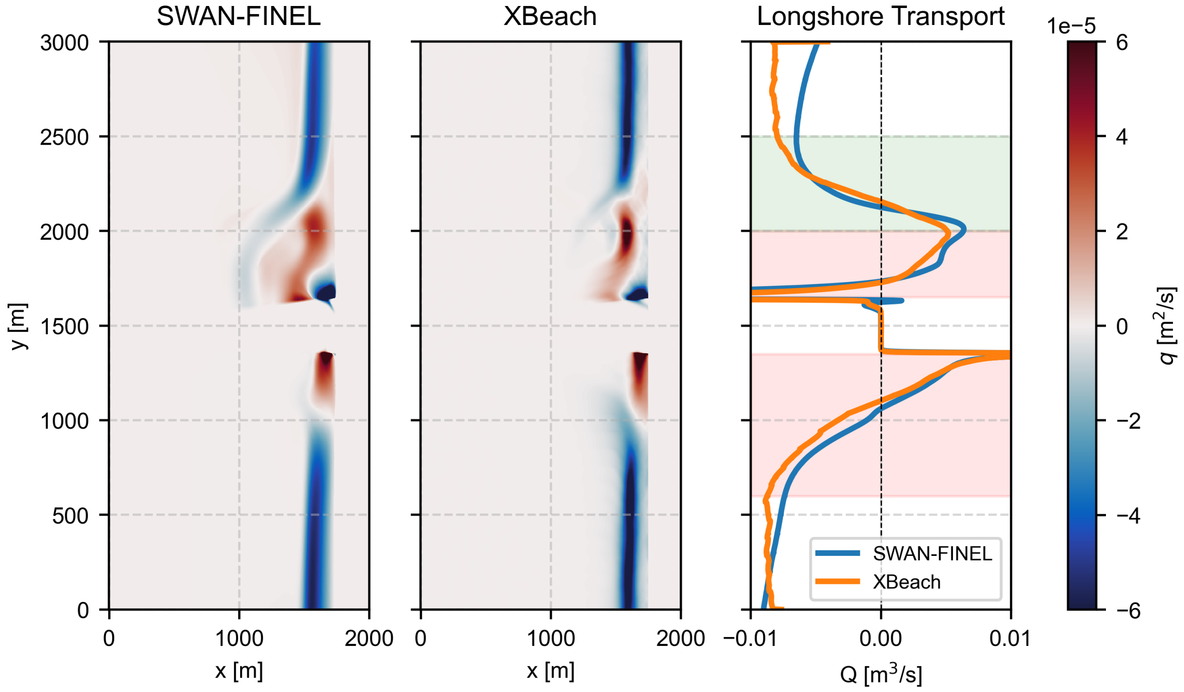

Figure 5.27: Comparison of spatial distribution of sediment flux vectors (q [m^2/s]) with cross-shore integrated longshore transport. Approximate areas with expected sedimentation are highlighted in green, and erosion is highlighted in red.

non-hydrostatic results is at most times below 25%.

Near the channel edges, large peaks in the differences between the models are observed. These peaks can be attributed to the large gradients in the transport rates in these regions. A minor shift in the location of maximum or minimum transport leads to a disproportionate deviation when the model results are compared.

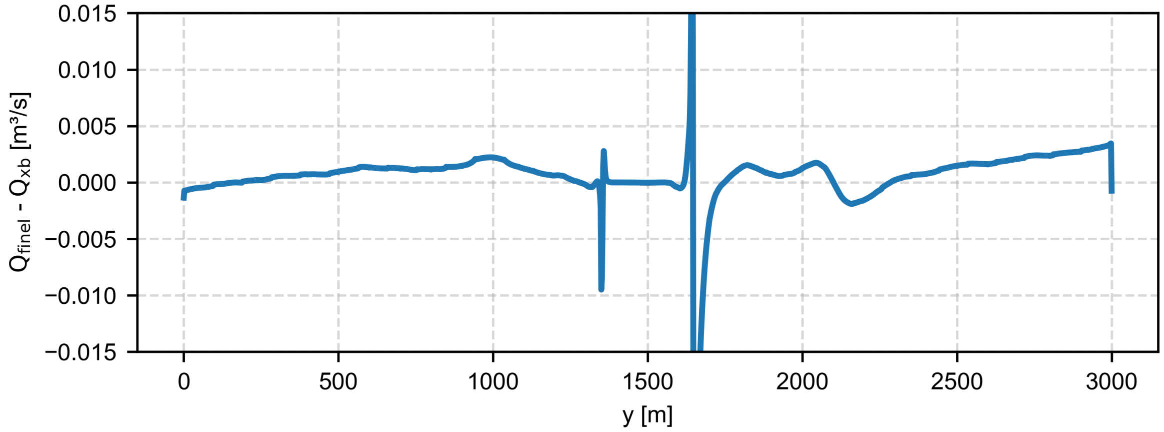

Figure 5.28: Difference in longshore transport volume $Q_{b,y}$ between FINEL and XBeach.

5.5.2. Initial bed level changes

Using the Exner equation, bed level changes can be computed from the bed load fluxes (see listing B.4 for implementation in Python):

$$\frac{\partial z_b}{\partial t} = \frac{1}{1-n}\left(\frac{\partial \langle q_{b,x}\rangle}{\partial x} + \frac{\partial \langle q_{b,y}\rangle}{\partial y}\right)$$

With the porosity $n = 0.4$. The time-averaged sediment fluxes from both models are used as the input, and the equation returns a spatial array with bed changes over time. A Gaussian filter with $\sigma = 3$ is applied to the XBeach sediment fluxes to reduce noise in the bed level changes. The bed update is computed over a short time (one day). The initial sediment fluxes are in some locations very high (e.g., near the channel edges and in the swash zone). This can create unrealistically large bed level changes.

Figure 5.29 displays a comparison of the computed initial bed level changes in the domain after one day, based on the time-averaged bed-load sediment fluxes from both models. This plot displays the differences between the models. SWAN-FINEL expects mainly erosion in the region from $x = 1500$ up to the shoreline, whereas XBeach predicts accretion in this region. The estimated bed level patterns appear to be reversed in the cross-shore direction between the two models.

In the alongshore direction, some of the predicted erosion and accretion can be observed in the bed level changes. South of the channel, the erosion increases moving toward the channel. Also, areas of erosion and accretion at the channel edges are visible in both models. One thing that the integration of the longshore transport over the cross-shore missed is the transportation of sediment further offshore. At $x = 2200$, sediment that is transported by the longshore current is transported offshore by the circulating current in the refraction region. The offshore transported sediment is building a shoal in this region. Both models agree on this, although this shoal is more spread out in SWAN-FINEL.

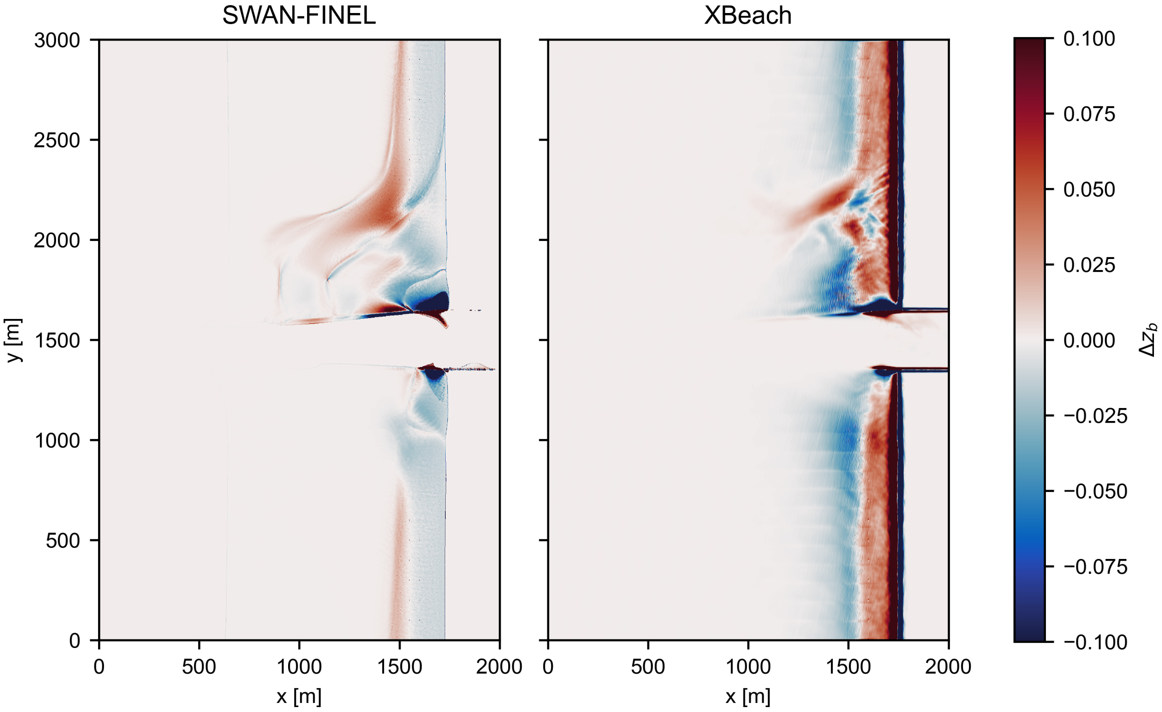

Figure 5.29: Comparison between bed level changes after one day, based on the initial sediment fluxes. Red implies an increase in bed level (accretion), where blue implies a decrease in bed level (erosion).

To further isolate the erosion and accretion in the alongshore direction, the sediment flux in the x-direction was set to zero ($q_{b,x} = 0$) in an additional computation. This analysis is performed to isolate the effect of the channel on the longshore transport and remove the dominance of the cross-shore redistribution of sediment. The results of this computation can be seen in Figure 5.30.

The difference between the two plots is much smaller compared to the initial bed level changes when considering sediment fluxes in both x- and y-directions. These plots exhibit similar erosion/sedimentation patterns as expected from the alongshore transport budget in Figure 5.27. The following patterns are observed:

- Heavy erosion on the outer edges and heavy accretion on the inner edges of the channel.

- Erosion south of the channel from $x = 500$ to $x = 1300$.
- Erosion directly north of the channel from $x = 1700$ to $x = 2000$.
- Accretion further north from $x = 2000$ to $x = 2400$.

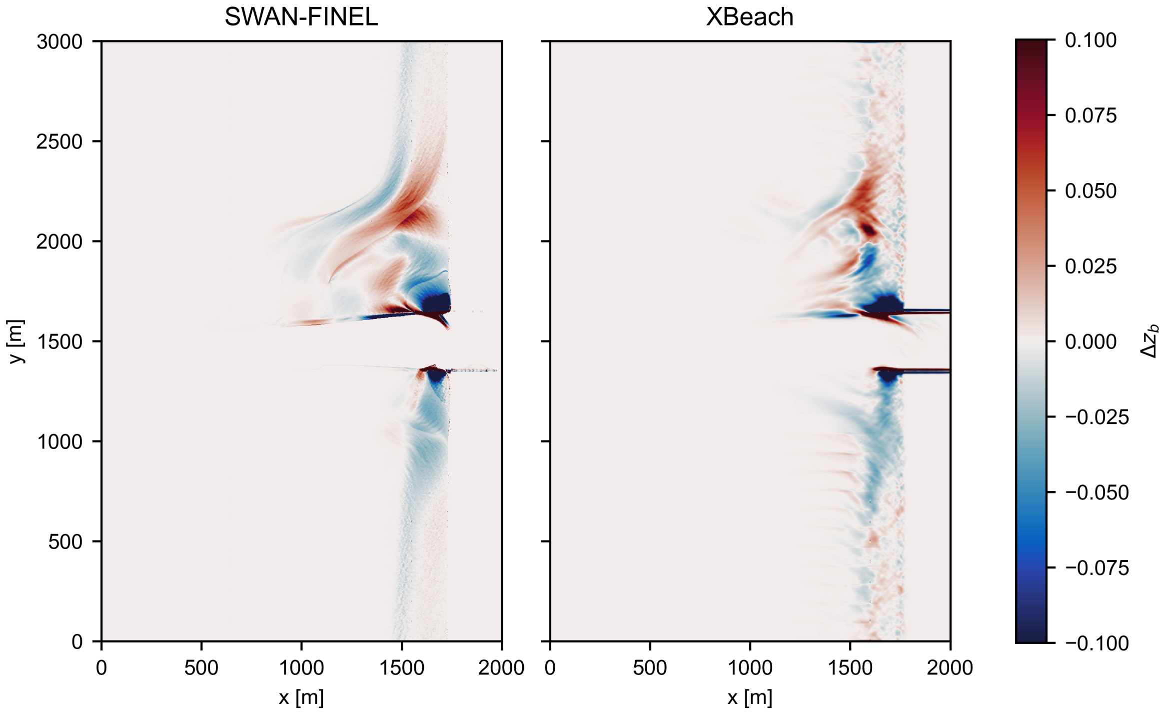

Figure 5.30: Comparison between bed level changes after one day, based on the initial sediment fluxes **only in y-direction**.

5.5.3. Channel infilling

The eroded sediment from the sand bed near the channel edges accretes on the channel slopes, where the flow velocities reduce. Channel infilling is an important process in the design of a channel, as it affects maintenance costs for dredging activities to maintain the required channel depth and width. Bed-load sediment usually does not end up deep in the channel, but on the channel edges, creating a shoal (Kraus & Larson, 2001). A similar thing is observed in the computed initial bed level changes; the sediment doesn't end up very deep in the channel, but remains at the higher parts of the channel slopes (Figure 5.31).

A comparison of the predicted sediment volume deposited in the channel was made. The region considered as the channel is marked with a green line in Figure 5.31. The total volumes of sand deposited and accreted in this region after one day (ΔV) in both models were computed and displayed in Table 5.7. The infilling volume predicted by SWAN-FINEL is approximately 13.8% larger than what XBeach predicts. The considered channel region stretches until $x = 1760$, not including any potential infilling in the channel inlet.

Model	Infilling volume ΔV [m^3]
SWAN-FINEL	14 476
XBeach	12 723

Table 5.7: Predicted channel infilling from both models after one day, based on the initial sediment fluxes.

5.6. Chapter summary

This chapter investigated the effects of channel refraction on wave propagation, hydrodynamics, and sediment transport using a synthetic test case consisting of an idealized straight coastline with a

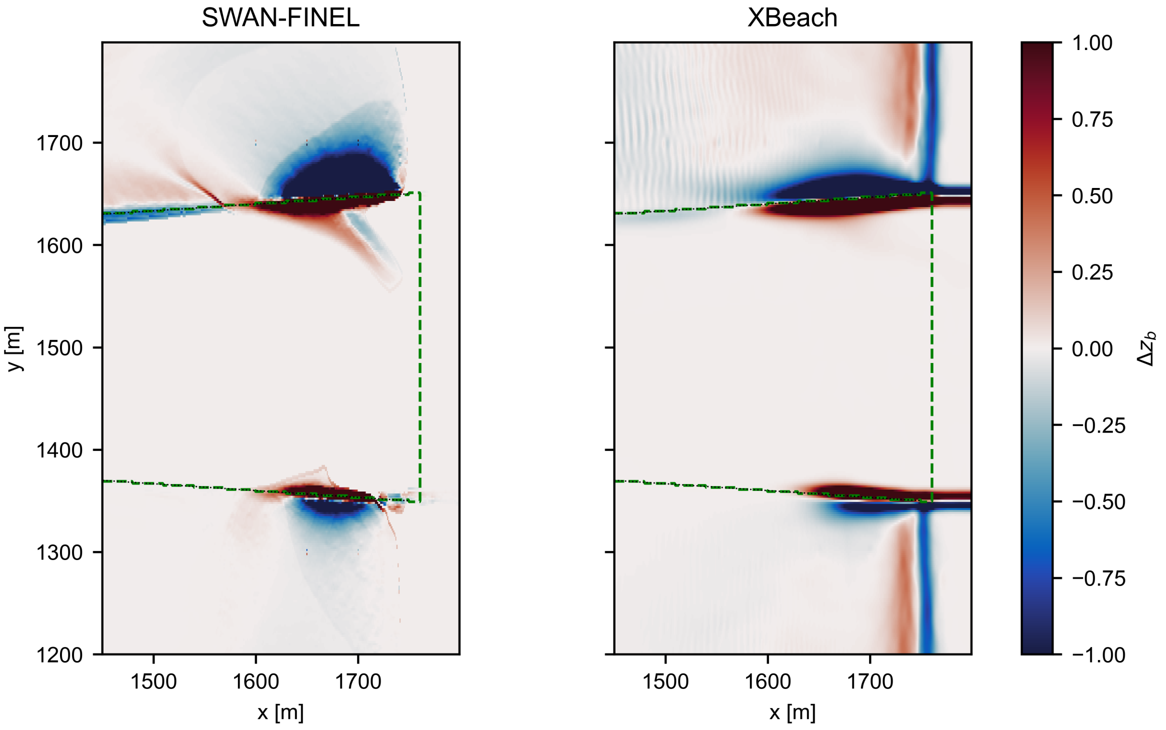

Figure 5.31: Comparison between bed level changes after one day, zoomed in on channel inlet. The green line signifies the region considered as the channel where infilling occurs.

dredged navigation channel. The study aimed to isolate and examine the physical mechanisms by which channel refraction modifies coastal morphodynamics and to evaluate the performance of two different modeling approaches under these conditions.

Two numerical models were employed: the phase-averaged SWAN-FINEL model and the phase-resolving XBeach non-hydrostatic model. The comparison provided insight into how model formulation influences predictions of wave transformation, flow patterns, bed shear stresses, and sediment transport fluxes.

The bathymetry consisted of a straight coast of 3 km long, with a perpendicular navigation channel of 20 m deep. It was designed to induce channel refraction at a dredged navigation channel with an adjacent straight coast to study the effects of channel refraction on the flows and sediment patterns in the nearby area.

Two different bed-load sediment transport models were employed: an intra-wave (for XBeach non-hydrostatic) and a wave-averaged (for SWAN-FINEL) model. Both models were based on the principles of the sediment transport model by Meyer-Peter and Müller (1948), allowing a fair comparison.

This case study highlights the added value of using a phase-resolving model like XBeach for capturing detailed nearshore processes, particularly in the surf and swash zones. At the same time, it shows that a phase-averaged model such as SWAN-FINEL can give very accurate sediment transport predictions in the longshore direction with much lower computational cost, provided that the limitations are understood.

Key takeaways

- The synthetic test case successfully induced channel refraction, resulting in an amplification of wave energy on the refracted side and a reduction on the lee side.
- SWAN-FINEL and XBeach both predicted similar wave propagation patterns and current structures, including a shadow zone on the lee side and a circulation current north of the channel.

- XBeach requires substantially more computational resources ($\sim$12 hours) than SWAN-FINEL ($\sim$3 hours) for an accurate result.
- It was found to be important to add mass-flux compensation to SWAN-FINEL for accurately capturing cross-shore flow.
- Cross-shore sediment transport differed significantly between both models: XBeach found onshore sediment transport in a large part of the surf zone, while SWAN-FINEL showed offshore fluxes.
- In the swash zone, XBeach predicted strong offshore-directed sediment fluxes, which were not captured by SWAN-FINEL.
- Longshore sediment transport magnitudes and gradients were consistent between the models, displaying similar regions of erosion and accretion.
- Initial bed updates showed a dominance of sediment redistribution in the cross-shore direction in the XBeach results. When only longshore transport gradients were evaluated, the initial bed level changes were very similar between both models.
- Predicted channel infilling volumes were similar, with SWAN-FINEL estimating 14 476 m^3 and XBeach estimating 12 723 m^3 of sediment deposition after one day.

6

Discussion

This chapter interprets the findings from both SWAN-FINEL and XBeach non-hydrostatic simulations. The discussion connects the results to the literature and channel design considerations and reflects on the study's uncertainties and limitations.

6.1. Interpretation

6.1.1. Model differences in wave and current processes

The comparison of SWAN-FINEL and XBeach non-hydrostatic revealed that both models are capable of reproducing large-scale wave transformation due to channel refraction. The agreement in significant wave height between models was generally good, with root-mean-square errors below 0.3 m under moderate wave conditions, and below 0.8 m in the energetic conditions. Additionally, both models properly captured the channel refraction and shadow zone on the channel lee side. This suggests that the core wave processes important to channel refraction are well represented in both the phase-averaged and phase-resolving models.

In SWAN-FINEL, the inclusion of Stokes and wave roller mass flux compensation was found to be very important for accurately predicting cross-shore flow patterns.

A notable difference between the flow patterns from both models was found in the circulation current on the northern side of the channel, which was more pronounced in SWAN-FINEL than in XBeach. This could be due to the wave-current interaction, which works only one way (wave forces induce currents) in SWAN-FINEL. Another explanation could be that the bed shear stresses in the shallow water equations in SWAN-FINEL don't contain mass flux compensation, whilst the bed would realistically experience these flows.

Additionally, a residual cross-shore flow from the western boundary was present in SWAN-FINEL and not in XBeach. This can likely be explained because it compensates for the outward flow in the northern and southern boundaries, which is not a problem in XBeach due to the cyclic boundaries. Because the waters near the western boundary are deep, this doesn't affect sediment transport.

6.1.2. Sediment transport and morphological response

The similarity in longshore transport predicted by both models displays that longshore processes are very well captured by both models, even in regions under the influence of channel refraction. Also, the amount of channel infilling is quite similar among both models, with a difference of only 13.8% based on the initial sediment fluxes. This suggests that, despite its simplifications, SWAN-FINEL performs comparably to XBeach in predicting longshore sediment transport.

The large differences observed in the bed level changes based on the initial sediment fluxes can be attributed to the models' differences in cross-shore sediment fluxes; in the cross-shore, large gradients are found in the sediment transport over the whole domain, causing heavy sedimentation and erosion.

This erosion and sedimentation are based on the initial sediment fluxes, and the sediment fluxes are expected to reduce quickly as sediment is redistributed over the cross-shore.

A beach profile can generally be characterized with a dynamic equilibrium (Bruun, 1954; Dean, 1977), where the beach profile varies based on the wave conditions at the time. The synthetic coast proposed in this study is likely far from its equilibrium, and as a result, the models try to redistribute sediment to reach equilibrium. Therefore, large cross-shore sediment fluxes are predicted by both models, which are most pronounced in the XBeach results.

Long-term evolution of the coastline is often determined by the longshore transport, whereas short-term changes can often be attributed to cross-shore transport (e.g. Bosboom & Stive, 2023; Hanson, 1989). This emphasizes the importance of accurately capturing longshore sediment fluxes when assessing long-term shoreline stability, even more so since the intervention in this research has a large effect on the alongshore flows near the channel.

6.1.3. Role of wave skewness and asymmetry in cross-shore transport

Some of the major differences in sediment transport between SWAN-FINEL and XBeach non-hydrostatic were observed in the surf zone. In SWAN-FINEL, although the cross-shore flows predicted were very close to XBeach, sediment transport was directed offshore in the largest part of the surf zone. In contrast, XBeach predicted onshore-directed sediment transport in most of the surf zone. This difference is likely explained by the influence of wave skewness and asymmetry, which are resolved in XBeach but not present in the wave-averaged sediment transport model used in this study.

Wave skewness leads to stronger and shorter onshore velocities during the wave crest phase, compared to weaker, but longer velocities in the trough. This asymmetry does not affect mean flow velocities, but it does affect sediment transport, which is proportional to the third power of the flow velocity ($q \propto u^3$).

To evaluate the potential influence of wave shape on sediment transport, the SWAN-FINEL results were post-processed using a modified Meyer-Peter-Müller approach inspired by the method of Soulsby and Damgaard (2005). In this approach, the nonlinear orbital velocities were reconstructed with the method by Abreu et al. (2010) based on the parameterized wave skewness and asymmetry approach by Ruessink et al. (2012). See Appendix D for a more comprehensive overview of this method.

Figure 6.1 compares the original SWAN-FINEL transport results (left), the skewness-and-asymmetry-corrected SWAN-FINEL results (middle), and the XBeach non-hydrostatic model (right). The inclusion of skewness produces transport patterns that more closely resemble the XBeach results in the cross-shore direction in large regions in the surf zone. These preliminary results indicate that even without a full phase-resolving model, waveshape effects can be captured using empirical parametrizations.

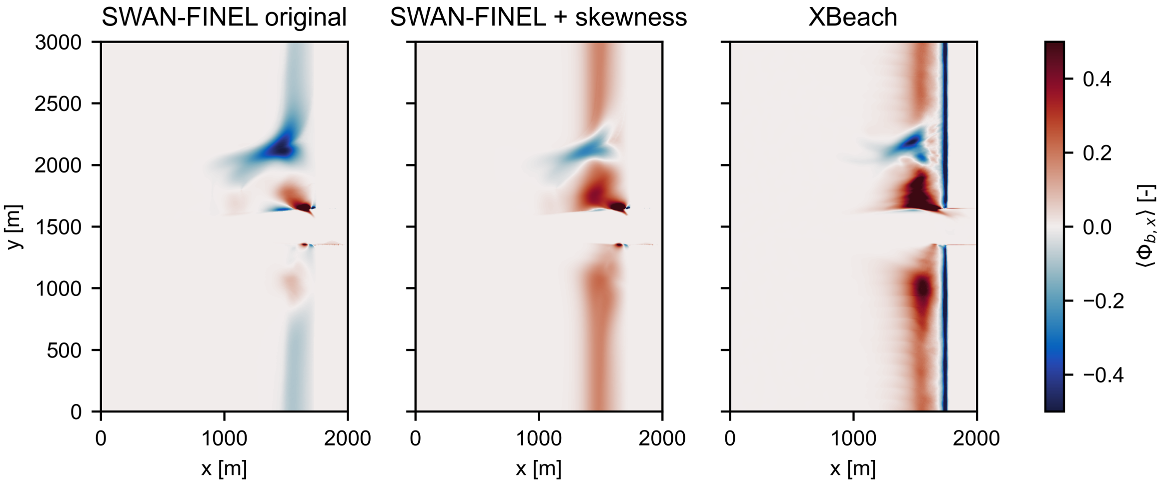

Figure 6.1: Comparison of dimensionless bed load transport in the x-direction ($\Phi_{b,x}$) after including wave shape parametrization in SWAN-FINEL (Ruessink et al., 2012).

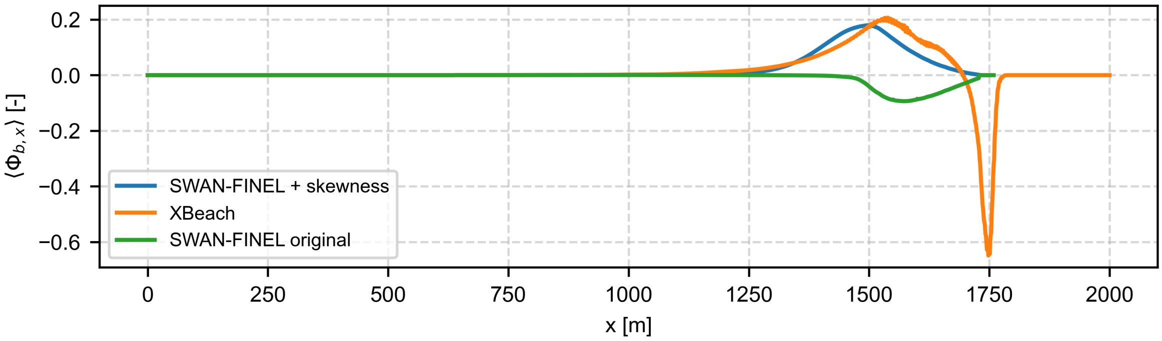

Figure 6.2: Comparison of dimensionless bed load transport in the x-direction ($\Phi_{b,x}$) in a cross-shore transect at y=500 after including wave shape parametrization in SWAN-FINEL (Ruessink et al., 2012).

Since this method was not used in the main workflow, the results are not used in the final sedimentation estimates. However, this demonstrates the importance of including the parameterized effect of skewness and asymmetry to properly predict cross-shore processes in a phase-averaged model.

6.1.4. Model differences in the swash zone

In the swash zone, XBeach displayed strong offshore-directed mean flows and sediment fluxes, which were not present in the simulations by SWAN-FINEL. Swash zone hydrodynamics and morphodynamics are less understood than those in the surf zone, mainly due to the challenges of collecting reliable data in the shallow, turbulent, and rapidly changing flows. Also, there is not a lot of experimental data on sediment transport in the swash zone (M. G. Hughes & Baldock, 2004).

In the swash zone, infragravity waves usually dominate (Stockdon et al., 2006). Short waves break in the surf zone and have most of their energy dissipated before reaching the swash zone. Low-frequency waves initially travel bound to short-wave groups, but are released in the surf zone after breaking (e.g. Longuet-Higgins & Stewart, 1962). These low-frequency waves induce backwashes with high velocities in the swash zone, primarily impacting bed-load transport (Butt & Russell, 1999). The backwash phase is longer than the uprush phase in the swash zone, and a mean offshore-directed flow is often observed in the swash zone (M. G. Hughes & Baldock, 2004; Raubenheimer, 2002).

The flow velocities in two locations in XBeach, as seen in Figure 6.3, align with the literature. In the swash zone, velocity oscillations have a lower frequency compared to the offshore region, implying that low-frequency waves dominate in this area. Uprushes with positive velocities are followed by backwashes with high offshore velocities and long duration, resulting in an offshore-directed mean flow.

In SWAN-FINEL, infragravity waves and swash motions are not resolved. In XBeach, infragravity waves are included, and flow velocities in the swash zone are fully resolved, resulting in the mean flow velocity in the swash zone being offshore-directed. The observed differences in the swash zone from both models may thus be attributed to the model fundamentals.

6.2. Implications for channel design

The results of this study contribute to the field of study that investigates the numerical modeling of wave-driven flow and sediment transport and its application near navigation channels. The observed patterns of wave propagation, wave focusing on the channel slope, and the formation of a shadow zone at the lee side are consistent with previous studies (e.g., Dusseljee et al., 2014; Li et al., 2000; Zwamborn & Grieve, 1974). However, the results of wave propagation on the lee side of the channel disagree with the studies by Dusseljee et al. (2014) and Groeneweg et al. (2014). The small difference between the results of wave propagation of the phase-averaged and phase-resolving model suggests that SWAN is a reliable tool for obtaining a fast estimate of wave propagation near a navigation channel.

The finding that both SWAN-FINEL and XBeach produce very comparable longshore sediment transport fluxes displays that simplified models are a useful tool for estimating coastline change and the

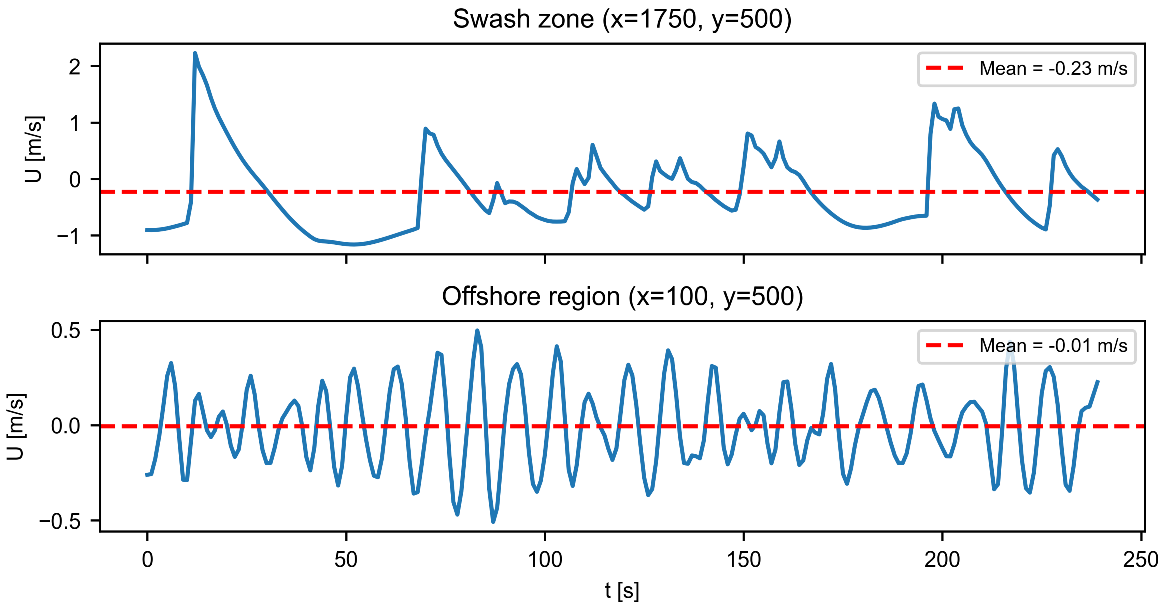

Figure 6.3: Instantaneous cross-shore depth-averaged flow velocities U during the first two minutes of the simulation (after spin-up time) as simulated by XBeach non-hydrostatic. The upper plot displays the flow velocities in the swash zone, and the lower plot displays the flow velocities in the offshore region where little wave transformations have taken place yet.

redistribution of sediment in the alongshore direction. This is particularly the case when cross-shore sediment flux gradients are small, for example, because the system is expected to be close to equilibrium.

The differences in cross-shore transport and resulting morphological change highlight the weaknesses of phase-averaged models. Wave skewness and asymmetry can be estimated with parameterizations (e.g., Ruessink et al., 2012; van der Lugt et al., 2024), but will require more calibration compared to non-hydrostatic models. This study further highlights that the omission of infragravity waves in the phase-averaged model impacts the predicted morphology. The complex processes in the swash zone are not included in SWAN-FINEL.

In practical terms, the results suggest that model choice influences the prediction of the effects of channel refraction on wave propagation and sediment dynamics. For coastal engineers, this means that model selection should be aligned with the physical processes most relevant to the project objectives. Longshore transport is often the dominant driver for coastline change following coastal interventions. When the objective is to estimate long-term shoreline evolution, and cross-shore gradients are expected to be small, phase-averaged models such as SWAN-FINEL provide a suitable and computationally efficient tool.

In the case studied in this thesis, the longshore processes were most dominant for the coastal response since the channel mainly affected wave energy distribution in the alongshore direction. Other channel and wave configurations could, however, lead to a more significant redistribution of wave energy in the cross-shore. For instance, a channel dredged at a more shore-parallel angle might create a lee zone in the cross-shore direction instead of the alongshore direction. This could induce sediment transport in the cross-shore direction and potentially lead to channel infilling in the cross-shore direction. In that instance, the cross-shore processes that are fully resolved by XBeach can be of more importance to the coastal response of the intervention.

Nevertheless, making a long-term simulation with XBeach non-hydrostatic is, in many practical applications, computationally unrealistic since the model time in XBeach in this study was order 5 times longer compared to SWAN and SWAN-FINEL, even when running on a faster machine. Additionally, for situations where alongshore processes are dominant, XBeach will not provide much added value, and SWAN-FINEL will be a good model to use. However, for situations where the channel greatly affects cross-shore processes, XBeach could be a valuable tool for a short-term prediction of coastal response. Furthermore, XBeach non-hydrostatic can be used to verify the reliability of SWAN-FINEL, and it can be used to calibrate the nonlinear processes in SWAN-FINEL, such as skewness and asymmetry.

6.3. Limitations and uncertainty

While the results of this study offer valuable insight into the impact of channel refraction on wave propagation and sediment dynamics, several limitations of this study must be acknowledged.

6.3.1. Limitations to the transport models

The sediment transport formulations applied in both models were limited to bed load transport only. Suspended load transport can contribute significantly to total sediment flux and can even be the dominant transport process for many coastal applications (Van Rijn, 2007). Mainly in the surf zone, turbulence induced by breaking waves is very efficient in suspending sediment high into the water column (e.g. Kubo & Sunamura, 2001; Yoon & Cox, 2010; Zhou et al., 2017). In this study, the sediment diameter was relatively coarse at $D_{50} = 1\,\mathrm{mm}$, but in many coasts in the world, the sediment is much finer, resulting in a larger contribution of suspended sediment.

A common modeling approach for suspended sediment is based on the advection-diffusion equation, which balances settling and mixing due to turbulent processes (e.g. van Rijn, 2007). The sediment that is transported is dependent on the instantaneous sediment concentration and flow velocity throughout the water column; $q_s(z,t) = c(z,t) \cdot u(z,t)$ (e.g. Aagaard et al., 2021; Van Rijn, 2007). The response of suspended sediment is thus different from the response of bed load transport to hydrodynamic forcing and is no longer quasi-steadily dependent on the bed shear stress.

A practical example of how suspended sediment can affect the channel is channel infilling. Bed-load transport primarily causes sediment to build up on the channel edges, increasing the channel width, but suspended sediment can be transported further into the deeper parts of the channel, where it settles in deeper parts of the channel, decreasing the channel depth (Kraus & Larson, 2001).

This simplification may lead to a wrong estimation of actual transport rates, particularly in the surf zone where turbulence driven by wave breaking can bring a lot of sediment in suspension. As a result, the predicted morphological changes in this study may not fully represent the sediment dynamics in a realistic situation. Therefore, the model results should be interpreted with the understanding that an important transport mechanism has been excluded.

Additionally, it is considered good practice to include a bed slope factor in the transport model (Bailard, 1981). Multiple approaches have been proposed to include a bed slope factor in the Meyer-Peter-Müller bed load transport formulation (e.g. Cheng & Chen, 2014; Damgaard et al., 1997; Smart, 1984). In the formulation by Soulsby (1997), this bed slope factor is not present. Therefore, it was chosen not to exclude bed slope altogether to keep the comparison between the two models fair. However, excluding the bed slope could affect transport patterns, mostly in the cross-shore direction.

6.3.2. No validation of sediment transport

The synthetic test case was not validated against field or laboratory measurements. The models used (SWAN-FINEL and XBeach non-hydrostatic) have been validated, and the assumption was made that XBeach non-hydrostatic is generally more accurate because of the higher resolution of the model and the additional processes, like skewness and infragravity wave, that it captures.

The synthetic setup allowed for a controlled comparison between models, which made it easier to isolate the differences between the models. However, the absence of observational data means that no quantitative assessment of model accuracy was possible. The analysis is therefore limited to a relative comparison between two modeling approaches rather than an evaluation of their performance against measurements.

The assumption that XBeach non-hydrostatic provides a more realistic baseline is not without limitations. In the Taman case, XBeach did not consistently outperform SWAN in simulating wave propagation, and previous studies have identified challenges in accurately predicting intra-wave sediment transport using XBeach non-hydrostatic (e.g., Mancini et al., 2021). While this study highlights fundamental differences in sediment transport predictions related to model fundamentals, it does not assess the absolute magnitude of inaccuracies in either model.

6.3.3. Simplified geometry and forcing conditions

The study was based on an idealized domain with a fixed bathymetry and boundary conditions. This simplified setup was useful for isolating the effects of channel refraction and comparing model behavior under consistent forcing. However, it does not capture the complexity of a real coastal system, where bathymetry variations and dynamic boundary conditions such as tides, currents, and wind-driven waves play a role.

In reality, a coastal wave climate consists of a wide spectrum of conditions varying in height, direction, and period (Pierson, 1955). The coastal response to these conditions will vary, and sediment transport patterns may change depending on the dominant wave direction, directional spreading, wave height, and wave period. A channel that appears stable under one wave condition may behave very differently under others. Additionally, the channel geometry (orientation, depth, shape) can also greatly alter the coastal response of such an intervention.

While the synthetic setup provides insight into the different processes incorporated in each model, the results cannot be directly applied to specific natural sites without a sensitivity study on variations in bathymetry and boundary conditions. The results from this study should be used in the context of this case only. Future applications should incorporate site-specific bathymetry and wave climate conditions to assess the reliability of the simulated morphodynamic response.

6.3.4. Short simulation period and absence of morphodynamic feedback

Morphological change was evaluated over a short simulation period of one day using fixed, time-averaged sediment fluxes. Morphodynamic feedbacks, where changes in bed levels influence hydrodynamics and sediment transport, were not included in this study. Bed level changes were computed in response to the initial transport fluxes without accounting for how those changes would, in turn, modify the flow and transport. This resulted in some locations in unrealistically large bed level changes (sometimes $> 1\,\mathrm{m}$).

Additionally, the long-term response of the coast was not assessed in this study. An evaluation was made on the longshore sediment budget and initial coastline response based on the initial sediment fluxes. An interesting insight would be to know how the coast would evolve over a time frame of months to years. This was not realistic in the scope of this research, considering that running XBeach non-hydrostatic for one hour already took almost twelve hours.

7

Conclusions and recommendations

7.1. Conclusions

This thesis investigated the effects of channel refraction on wave propagation and sediment transport using two numerical modeling approaches: the phase-averaged model SWAN-FINEL and the phase-resolving model XBeach in non-hydrostatic mode. By analyzing both a validated physical model case and an idealized synthetic case, insights could be obtained into how the underlying assumptions of both models affect predictions of nearshore hydrodynamics and sediment transport.

The central research question was:

> *How does channel refraction influence wave propagation and sediment transport, and what level of modeling detail is required to accurately predict its effects?*

This main question was split into four sub-questions, which are answered below.

How does channel refraction impact wave propagation and sediment dynamics?
Channel refraction occurs when waves refract on the slopes of a navigation channel when they approach at near-parallel angles. As a result, wave energy focuses on the slopes of the channel, while a shadow zone with reduced wave heights forms on the lee side. This refraction pattern was evident in both the physical and synthetic cases.

In the studied case, the wave field induces flow patterns leading to features such as a circulation current north of the channel around the region of wave focusing, and inward-directed flows on both sides of the channel. These flows affect sediment transport: bed-load transport fluxes at the channel slopes lead to infilling at the channel edges. An offshore-directed current north of the refraction area moves bed-load sediment to deeper waters, creating a shoal. New gradients in longshore transport are expected to impact the coastline in the long term.

What are the strengths and limitations of phase-averaged models (e.g., SWAN-FINEL) in representing channel refraction and its influence on sediment transport?
The SWAN-FINEL model was able to accurately predict the overall effects of channel refraction on wave propagation and flows. Wave heights and the refraction pattern aligned well with observations in the Taman case. The model also captured the most important sediment transport features around the channel, including a longshore current, an offshore-directed flow north of the refracted area, and large sediment fluxes at the channel edges. The longshore transport fluxes in SWAN-FINEL were very comparable to those in XBeach.

Limitations were most apparent in the cross-shore direction. In particular, SWAN-FINEL underrepresented sediment processes in the swash zone and surf zone. SWAN-FINEL does not resolve infragravity waves, which are very important in the swash zone, leading to a large underestimation of sediment transport in that region.

Wave skewness and asymmetry, which lead to onshore sediment transport, were not included in the phase-averaged transport model. In the SWAN-FINEL simulations, undertow was the dominant driver for sediment transport in the surf zone, leading to offshore transport, whereas XBeach predicted onshore transport. Using a parametrization to estimate the waveform is possible, but would require careful calibration and an appropriate sediment transport model.

To what extent does a phase-resolving model (e.g., XBeach non-hydrostatic) improve the accuracy of wave propagation and sediment transport predictions under channel refraction conditions?
XBeach accurately captured channel refraction and the resulting wave field. However, compared to SWAN, XBeach did not offer much added value based on measurements. On the lee side of the channel, XBeach did outperform SWAN.

XBeach non-hydrostatic demonstrated better performance in predicting sediment transport in areas where intra-wave processes dominate. The model captured the effects of wave skewness and asymmetry, leading to higher onshore-directed sediment transport compared to SWAN-FINEL. In the swash zone, backwashes induced by low-frequency waves resulted in an offshore-directed bed-load transport. It also produced slightly better agreement with measurements in a physical model, especially under energetic conditions.

However, this improved accuracy came at the cost of significantly higher computational demands, as XBeach required four times more computational time and a higher resolution.

What insights can be derived from the model comparison to guide the design of navigation channels?
SWAN-FINEL has captured the longshore transport processes very well at a much lower computational cost than XBeach. Thus, SWAN-FINEL is a reliable sediment model in systems where longshore transport is expected to dominate over cross-shore transport.

XBeach non-hydrostatic can be a valuable tool for gaining a more detailed initial estimate of the hydrodynamics and morphology in a short time frame in systems where cross-shore transport is expected to be significant. In practical applications, XBeach will often be too computationally intensive to use for determining the long-term impact of the channel refraction.

It is important to note that these findings are based on one single idealized case, and the conclusions may not be directly applicable to all real-world settings. The results are valid for the channel geometry, wave conditions, and sediment characteristics considered in this study.

Main conclusion
Using the answers to the sub-questions above, the main research question can now be answered.

Channel refraction significantly influences wave propagation and sediment dynamics. It creates a zone with increased wave energy on the refracted side of the channel and a shadow zone on the lee side of the channel. This induces flows and sediment transport gradients in the coastal system, impacting morphology. In the Taman case, both models captured wave propagation well, and SWAN was significantly less computationally demanding. On the lee side of the channel and in energetic conditions, XBeach performed better than SWAN. In the idealized case, the phase-averaged model SWAN-FINEL is sufficiently accurate and efficient for capturing longshore transport effects at a low computational cost, making it well-suited for long-term simulations in longshore-dominated systems. However, accurately predicting cross-shore sediment transport in the surf and swash zones requires the added detail of a phase-resolving model like XBeach non-hydrostatic.

The level of modeling detail required depends on whether longshore or cross-shore sediment transport processes dominate and the time scale of interest. For systems where longshore transport dominates, a phase-averaged model like SWAN-FINEL is sufficient, whereas in systems with strong cross-shore dynamics, a phase-resolving model like XBeach non-hydrostatic is expected to provide valuable insight into short-term sediment transport patterns.

7.2. Recommendations

- **Investigate the role of suspended sediment.** The study excluded suspended load sediment transport. Including suspended sediment in the morphological computations will give a more complete and accurate picture of the differences between the models.

- **Extend the analysis to include morphodynamic feedbacks.** This study used an offline sediment transport model to compute the bed load transport fluxes. Future work should include fully coupled morphodynamic simulations to assess the long-term effects of channel refraction on coastal evolution and sediment redistribution along the cross-shore.
- **Quantify uncertainty and model sensitivity more systematically.** While this study included a calibration of sensitive parameters for XBeach, a full sensitivity analysis with different wave conditions and channel configurations could help identify which parameters influence channel refraction and give more guidance on the design process.
- **Validate sediment transport predictions with field data.** While the physical model helped validate hydrodynamics, the results of the synthetic case were not validated with measurements. A future study with field measurements of sediment dynamics at a site with channel refraction would strengthen confidence in the model outcomes.

References

Aagaard, T., Brinkkemper, J., Christensen, D. F., Hughes, M. G., & Ruessink, G. (2021). Surf Zone Turbulence and Suspended Sediment Dynamics— A Review. https://doi.org/10.3390/jmse9111300

Abreu, T., Silva, P. A., Sancho, F., & Temperville, A. (2010). Analytical approximate wave form for asymmetric waves. *Coastal Engineering*, *57*(7), 656–667. https://doi.org/10.1016/J.COASTALENG.2010.02.005

Adema, J., van Vledder, G., & Koop, O. (2009). *SWAN Hindcast Eastern Wadden Sea: Storm of 9 November 2007* (tech. rep. No. A2191R1R5) (Accessed June 6, 2025). Alkyon. https://open.rijkswaterstaat.nl/publish/pages/82052/a2191_swan_hindcast_eastern_waddensea_storm_of_9_november_2007_a2191r1r5_final.pdf

Adytia, D., Ramdhani, M., & Groesen, E. (2012). Phase resolved and averaged wave simulations in jakarta harbour.

Airy, G. B. (1845). *Tides and waves: Extracted from the encyclopaedia metropolitana*.

Alves, J.-H., & Banner, M. (2003). Performance of a saturation-based dissipation-rate source term in modeling the fetch-limited evolution of wind waves. *Journal of Physical Oceanography - J PHYS OCEANOGR*, *33*. https://doi.org/10.1175/1520-0485(2003)033<1274:POASDS>2.0.CO;2

Amoudry, L. O., & Souza, A. J. (2011). Deterministic coastal morphological and sediment transport modeling: A review and discussion. *Reviews of Geophysics*, *49*(2). https://doi.org/10.1029/2010RG000341

Arthur, R. S., Munk, W. H., & Isaacs, J. D. (1952). The direct construction of wave rays. *Eos, Transactions American Geophysical Union*, *33*(6), 855–865. https://doi.org/10.1029/TR033i006p00855

Bailard, J. A. (1981). An energetics total load sediment transport model for a plane sloping beach. *Journal of Geophysical Research: Oceans*, *86*(C11), 10938–10954. https://doi.org/https://doi.org/10.1029/JC086iC11p10938

Barber, N. F., & Ursell, F. (1948). The generation and propagation of ocean waves and swell. i. wave periods and velocities. *Philosophical Transactions of the Royal Society of London. Series A, Mathematical and Physical Sciences*, *240*(824), 527–560. https://doi.org/10.1098/rsta.1948.0005

Battjes, J. A., & Janssen, J. (1978). Energy loss and set-up due to breaking of random waves. In *Coastal engineering 1978* (pp. 569–587). https://doi.org/10.1061/9780872621909.034

Battjes, J. A., & Labeur, R. J. (2021). *Unsteady flow in open channels*. Cambridge University Press.

Bayram, A., Larson, M., Miller, H. C., & Kraus, N. C. (2001). Cross-shore distribution of longshore sediment transport: Comparison between predictive formulas and field measurements. *Coastal Engineering*, *44*(2), 79–99. https://doi.org/https://doi.org/10.1016/S0378-3839(01)00023-0

Bijker, E. (1971). Longshore transport computations. *ASCE J Waterways Harbors Div*, *97*(WW4). https://doi.org/10.1061/awhcar.0000122

Booij, N., Ris, R. C., & Holthuijsen, L. H. (1999). A third-generation wave model for coastal regions: 1. model description and validation. *Journal of Geophysical Research Atmospheres*, *104*(C4), 7649–7666. https://doi.org/10.1029/98jc02622

Bosboom, J., & Stive, M. J. (2023). *Coastal dynamics*. TU Delft Open. https://doi.org/10.5074/T.2021.001

Bowen, A. J. (1980). Simple models of nearshore sedimentation: Beach profiles and long-shore bars. *The Coastline of Canada, edited by SB McCann, Pap*, 10–80. https://doi.org/10.4095/102213

Breusers, H. (1983). Lecture notes on sediment transport 1. https://resolver.tudelft.nl/uuid:7d021b46-0f6c-4660-a626-a0bd25539046

Bruun, P. (1954). Coast Erosion and the Development of Beach Profiles. *US Army Corps of Engineers*, (44).

Butt, T., & Russell, P. (1999). Suspended sediment transport mechanisms in high-energy swash. *Marine Geology*, *161*(2-4). https://doi.org/10.1016/S0025-3227(99)00043-2

Carter, T. G., Liu, P. L., & Mei, C. C. (1973). MASS TRANSPORT BY WAVES AND OFFSHORE SAND BEDFORMS. *ASCE J Waterw Harbors Coastal Eng Div*, *99*(WW2). https://doi.org/10.1061/awhcar.0000183

Cheng, N.-S., & Chen, X. (2014). Slope Correction for Calculation of Bedload Sediment Transport Rates in Steep Channels. *Journal of Hydraulic Engineering*, *140*(6). https://doi.org/10.1061/(asce)hy.1943-7900.0000843

Collins, J. I. (1972). Prediction of shallow-water spectra. *Journal of Geophysical Research*, *77*(15), 2693–2707. https://doi.org/10.1029/JC077i015p02693

Dam, G., Bliek, A. J., & Bruens, A. (2005). Band width analysis morphological predictions Haringvliet Estuary. *River, Coastal and Estuarine Morphodynamics*, 171–179. https://www.svasek.nl/wp-content/uploads/2017/04/con_pub_2005_Haringvliet.pdf

Dam, G., de Wit, L., van Leeuwen, B., Attema, Y., & Bom, S. (2018). *Technical manual FINEL2D version 7.29 Final* (tech. rep.). Svasek Hydraulics. www.svasek.com

Damgaard, J. S., Whitehouse, R. J. S., & Soulsby, R. L. (1997). Bed-Load Sediment Transport on Steep Longitudinal Slopes. *Journal of Hydraulic Engineering*, *123*(12). https://doi.org/10.1061/(asce)0733-9429(1997)123:12(1130)

Davies, A. G., Soulsby, R. L., & King, H. L. (1988). A numerical model of the combined wave and current bottom boundary layer. *Journal of Geophysical Research: Oceans*, *93*(C1). https://doi.org/10.1029/jc093ic01p00491

de Wit, F. (2016). *Tide-induced currents in a phase-resolving wave model* [Master's thesis, Delft University of Technology].

De Ridder, M. P., Smit, P. B., Van Dongeren, A. R., McCall, R. T., Nederhoff, K., & Reniers, A. J. (2020). Efficient two-layer non-hydrostatic wave model with accurate dispersive behaviour. *Coastal Engineering*, *164*, 103808. https://doi.org/10.1016/j.coastaleng.2020.103808

Dean, R. G. (1977, January). *Equilibrium beach profiles: U.S. Atlantic and Gulf Coasts* (tech. rep.). University of Delaware. Newark.

Deltares. (2025a). Welcome to delft3d. https://oss.deltares.nl/web/delft3d

Deltares. (2025b). *Xbeach*. https://oss.deltares.nl/web/xbeach/

Dorochinski, J. (2014). *A combination of swash and harberth to compute wave forces on moored ships* [Master's thesis, Delft University of Technology]. https://resolver.tudelft.nl/uuid:a0b269f8-6dc3-4de0-b1bd-918577f1456f

Dorrestein, R. (1960). Simplified method of determining refraction coefficients for sea waves. *Journal of Geophysical Research*, *65*(2), 637–642. https://doi.org/10.1029/JZ065i002p00637

Dusseljee, D., Klopman, G., van Vledder, G., & Riezebos, H. J. (2014). Impact of harbor navigation channel on waves: A numerical modelling guideline. *Coastal Engineering Proceedings*, *1*(34), 58. https://doi.org/10.9753/icce.v34.waves.58

Eckart, C. (1952). The propagation of gravity waves from deep to shallow water. *Gravity Waves*, 165.

Eikema, Attema, Talstra, Bliek, de Wit, & Dusseljee. (2018). *Spectral modeling of wave propagation in coastal areas with a harbor navigation channel* [congress paper] [online]. https://www.svasek.nl/wp-content/uploads/2017/04/con_pub_2018_Spectral_modeling_of_wave_propagation.pdf

Eikema, B. J. O., Attema, Y., Talstra, H., Bliek, A. J., De Wit, L., & Dusseljee, D. W. (2018). *Spectral modeling of wave propagation in coastal areas with a harbor navigation channel* (tech. rep.). https://www.svasek.nl/wp-content/uploads/2017/04/con_pub_2018_Spectral_modeling_of_wave_propagation.pdf

Eldeberky, Y., & Battjes, J. (1995). Nonlinear coupling in waves propagating over a bar. In *Coastal engineering 1994* (pp. 157–167). https://doi.org/10.1061/9780784400890.013

Engelund, F., & Hansen, E. (1967). *A monograph on sediment transport in alluvial streams*. Teknisk Forlag - Copenhagen. https://resolver.tudelft.nl/uuid:81101b08-04b5-4082-9121-861949c336c9

Fernandez Luque, R., & Van Beek, R. (1976). Erosion and transport of bed-load sediment. *Journal of hydraulic research*, *14*(2), 127–144.

Fredsøe, J. (1984). Turbulent Boundary Layer in Wave□current Motion. *Journal of Hydraulic Engineering*, *110*(8). https://doi.org/10.1061/(asce)0733-9429(1984)110:8(1103)

Goda, Y. (1986). Effect of wave tilting on zero-crossing wave heights and periods. *Coastal Engineering in Japan*, *29*(1), 79–90. https://doi.org/10.1080/05785634.1986.11924429

Grant, W. D., & Madsen, O. S. (1979). Combined wave and current interaction with a rough bottom. *Journal of Geophysical Research: Oceans*, *84*(C4). https://doi.org/10.1029/jc084ic04p01797

Groeneweg, J., Gent, M., Nieuwkoop, J., & Toledo, Y. (2015). Wave propagation into complex coastal systems and the role of nonlinear interactions. *Journal of Waterway Port Coastal and Ocean Engineering*, *141*. https://doi.org/10.1061/(ASCE)WW.1943-5460.0000300

Groeneweg, J., Van Nieuwkoop, J., & Toledo, Y. (2014). On the modelling of swell wave penetration into tidal inlet systems. *Coastal Engineering Proceedings*, *1*(34), 10. https://doi.org/10.9753/icce.v34.waves.10

Guzmán Mardones, C. (2011). *Impact of access channel geometry on wave penetration in harbours* [Master's thesis, Delft University of Technology]. https://resolver.tudelft.nl/uuid:1ba13e2e-ba4e-4802-9366-92f7fc00bdfa

Hanson, H. (1989). GENESIS - a generalized shoreline change numerical model. *Journal of Coastal Research*, *5*(1).

Hasselmann, K. (1974). On the spectral dissipation of ocean waves due to white capping. *Boundary-Layer Meteorology*, *6*, 107–127. https://doi.org/10.1007/BF00232479

Hasselmann, K., Barnett, T. P., Bouws, E., Carlson, H., Cartwright, D. E., Enke, K., Ewing, J., Gienapp, A., Hasselmann, D., Kruseman, P., et al. (1973). Measurements of wind-wave growth and swell decay during the joint north sea wave project (jonswap). *Ergaenzungsheft zur Deutschen Hydrographischen Zeitschrift, Reihe A*.

Holthuijsen, L. H. (2007, January 25). *Waves in oceanic and coastal waters*. Cambridge University Press. https://doi.org/10.1017/cbo9780511618536

Hughes, M. G., & Baldock, T. E. (2004). Eulerian flow velocities in the swash zone: Field data and model predictions. *Journal of Geophysical Research: Oceans*, *109*(8). https://doi.org/10.1029/2003JC002213

Hughes, T. (1987). *The Finite Element Method. Linear Static and Dynamic Finite Element Analysis* (Vol. 65).

Huynh-Thanh, S., & Temperville, A. (1991). Numerical model of the rough turbulent boundary layer in combined wave and current interaction. *Proceedings of the Coastal Engineering Conference*, *1*. https://doi.org/10.1061/9780872627765.067

ITTC. (2011). *Ittc – recommended procedures: Fresh water and seawater properties*. ITTC. https://ittc.info/media/4048/75-02-01-03.pdf

Komen, G. J., Cavaleri, L., Donelan, M., Hasselmann, K., Hasselmann, S., & Janssen, P. A. E. M. (1994). *Dynamics and modelling of ocean waves*. Cambridge University Press.

Kraus, N. C., & Larson, M. (2001). Mathematical Model for Rapid Estimation of Infilling and Sand By-passing at Inlet Entrance Channels. *Program*, (June).

Kubo, H., & Sunamura, T. (2001). Large-scale turbulence to facilitate sediment motion under spilling breakers. *Coastal Dynamics 2001*. https://doi.org/10.1061/40566(260)22

Li, Y., Liu, S., Wai, O., & Yu, Y. (2000). Wave concentration by a navigation channel. *Applied Ocean Research*, *22*(4), 199–213. https://doi.org/10.1016/s0141-1187(00)00013-4

Li, Y., Liu, S.-X., Yu, Y.-X., & Lai, G.-Z. (1999). Numerical modeling of boussinesq equations by finite element method. *Coastal Engineering*, *37*(2), 97–122. https://doi.org/https://doi.org/10.1016/S0378-3839(99)00014-9

Longuet-Higgins, M. S., & Stewart, R. W. (1962). Radiation stress and mass transport in gravity waves, with application to 'surf beats'. *Journal of Fluid Mechanics*, *13*(4). https://doi.org/10.1017/S0022112062000877

Longuet-Higgins, M. S. (1953). Mass transport in water waves. *Philosophical Transactions of the Royal Society of London. Series A, Mathematical and Physical Sciences*, *245*(903), 535–581. https://doi.org/10.1098/rsta.1953.0006

Madsen, O. S. (1991). Mechanics of cohesionless sediment transport in coastal waters. *Coastal Sediments '91*.

Madsen, O. S., Poon, Y.-K., & Graber, H. C. (1988). Spectral wave attenuation by bottom friction: Theory. In *Coastal engineering 1988* (pp. 492–504). https://doi.org/10.1061/9780872626874.035

Madsen, P. A., Fuhrman, D. R., & Wang, B. (2006). A boussinesq-type method for fully nonlinear waves interacting with a rapidly varying bathymetry. *Coastal Engineering*, *53*(5), 487–504. https://doi.org/https://doi.org/10.1016/j.coastaleng.2005.11.002

Magne, R., Belibassakis, K. A., Herbers, T. H. C., Ardhuin, F., O'Reilly, W. C., & Rey, V. (2007). Evolution of surface gravity waves over a submarine canyon. *Journal of Geophysical Research: Oceans*, *112*(C1). https://doi.org/https://doi.org/10.1029/2005JC003035

Mancini, G., Briganti, R., McCall, R., Dodd, N., & Zhu, F. (2021). Numerical modelling of intra-wave sediment transport on sandy beaches using a non-hydrostatic, wave-resolving model. *Ocean Dynamics*, *71*(1), 1–20.

Manning, R. (1891). *On the flow of water in open channels and pipes*. Transactions of the Institution of Civil Engineers of Ireland.

McCall, R., Quataert, E., Roelvink, D. J., de Bakker, A., de Goede, R., van Dongeren, A., de Ridder, M., de Vet, L., & van der Lugt, M. (2022). *Xbeach documentation: Release boi-phase3-5956* (tech. rep.). Deltares.

Mei, C. C. (1983). *The applied dynamics of ocean surface waves* (Vol. 1). World scientific. https://doi.org/10.1142/0752

Meyer-Peter, E., & Müller, R. (1948). Formulas for bed-load transport. *Proc IAHR, Stockholm*. https://resolver.tudelft.nl/uuid:4fda9b61-be28-4703-ab06-43cdc2a21bd7

Miles, J. W. (1957). On the generation of surface waves by shear flows. *Journal of Fluid Mechanics*, *3*(2), 185–204.

Misra, S. K., Driscoll, A. M., Kirby, J. T., Cornett, A., Lomonaco, P., Sayao, O., & Yavary, M. (2009). Surface gravity wave interactions with deep-draft navigation channels–physical and numerical modeling case studies. In *Coastal engineering 2008: (in 5 volumes)* (pp. 2786–2798). World Scientific. http://dx.doi.org/10.1142/9789814277426_0230

Munk, W., & Arthur, R. (1952). 13. wave intensity along a refracted ray. *Proceedings of NBS Semicentennial Symposium on Gravity Waves Held at the NBS on June 18-20, 1951*, *521*, 95.

Nairn, R. B., Roelvink, J. A., & Southgate, H. N. (1990). Transition zone width and implications for modelling surfzone hydrodynamics. *Proceedings of the Coastal Engineering Conference*, *1*. https://doi.org/10.1061/9780872627765.007

Neumann, B., Vafeidis, A. T., Zimmermann, J., & Nicholls, R. J. (2015). Future coastal population growth and exposure to sea-level rise and coastal flooding - A global assessment. *PLoS ONE*, *10*(3). https://doi.org/10.1371/journal.pone.0118571

Nielsen, P. (2006). Sheet flow sediment transport under waves with acceleration skewness and boundary layer streaming. *Coastal Engineering*, *53*(9), 749–758. https://doi.org/https://doi.org/10.1016/j.coastaleng.2006.03.006

Phillips, O. (1957). On the generation of waves by turbulent wind. *Journal of fluid mechanics*, *2*(5), 417–445.

Phillips, O. (1977). *The dynamics of the upper ocean*. Cambridge University Press. https://books.google.nl/books?id=tLRrAQAACAAJ

Pierson, W. J. (1955). *Practical methods for observing and forecasting ocean waves by means of wave spectra and statistics* (Vol. 603). US Government Printing Office.

Pokrajac, D., Finnigan, J. J., Manes, C., McEwan, I., & Nikora, V. (2006). On the definition of the shear velocity in rough bed open channel flows. *Proceedings of the International Conference on Fluvial Hydraulics - River Flow 2006*, *1*. https://doi.org/10.1201/9781439833865.ch7

Raubenheimer, B. (2002). Observations and predictions of fluid velocities in the surf and swash zones. *Journal of Geophysical Research: Oceans*, *107*(11). https://doi.org/10.1029/2001jc001264

Reniers, A. J. H. M., Gallagher, E. L., MacMahan, J. H., Brown, J. A., van Rooijen, A. A., van Thiel de Vries, J. S. M., & van Prooijen, B. C. (2013). Observations and modeling of steep-beach grain-size variability. *Journal of Geophysical Research: Oceans*, *118*(2), 577–591. https://doi.org/https://doi.org/10.1029/2012JC008073

Ribberink, J. S. (1998). Bed-load transport for steady flows and unsteady oscillatory flows. *Coastal Engineering*, *34*(1), 59–82. https://doi.org/https://doi.org/10.1016/S0378-3839(98)00013-1

Riezebos, H. J. (2014). Validation of swash for wave-channel interactions [Additional Thesis]. *Delft University of Technology*.

Roelvink, D. J., & Reniers, A. (2011, October). *A guide to modeling coastal morphology*. https://doi.org/10.1142/9789814304269_0006

Roelvink, D. J., Reniers, A., Van Dongeren, A., Van Thiel De Vries, J., McCall, R., & Lescinski, J. (2009). Modelling storm impacts on beaches, dunes and barrier islands. *Coastal Engineering*, *56*(11-12), 1133–1152. https://doi.org/10.1016/j.coastaleng.2009.08.006

Roelvink, D. J., & Stive, M. (1989). Bar-generating cross-shore flow mechanisms on a beach. *Journal of Geophysical Research*, *94*, 4785–4800. https://doi.org/10.1029/JC094iC04p04785

Ruessink, B. G., Ramaekers, G., & Van Rijn, L. C. (2012). On the parameterization of the free-stream non-linear wave orbital motion in nearshore morphodynamic models. *Coastal Engineering*, *65*. https://doi.org/10.1016/j.coastaleng.2012.03.006

Shields, A. (1936). *Application of similarity principles and turbulence research to bed-load movement* [Doctoral dissertation, Delft University of Technology]. https://resolver.tudelft.nl/uuid:a66ea380-ffa3-449b-b59f-38a35b2c6658

Smart, G. M. (1984). Sediment Transport Formula for Steep Channels. *Journal of Hydraulic Engineering*, *110*(3). https://doi.org/10.1061/(asce)0733-9429(1984)110:3(267)

Smit, P., Janssen, T., Holthuijsen, L., & Smith, J. (2014). Non-hydrostatic modeling of surf zone wave dynamics. *Coastal Engineering*, *83*, 36–48. https://doi.org/10.1016/j.coastaleng.2013.09.005

Smit, P., Stelling, G., Roelvink, D. J., Thiel de Vries, J., McCall, R., van Dongeren, A., Zwinkels, C., & Jacobs, R. (2010, January). *Xbeach: Non-hydrostatic model: Validation, verification and model description*.

Smit, P., Zijlema, M., & Stelling, G. (2013). Depth-induced wave breaking in a non-hydrostatic, near-shore wave model. *Coastal Engineering*, *76*, 1–16. https://doi.org/https://doi.org/10.1016/j.coastaleng.2013.01.008

Smolarkiewicz, P. K., & Pudykiewicz, J. A. (1992). A class of semi-lagrangian approximations for fluids. *Journal of Atmospheric Sciences*, *49*(22), 2082–2096. https://doi.org/10.1175/1520-0469(1992)049%3C2082:ACOSLA%3E2.0.CO;2

Soulsby, R. L. (1995). Bed shear-stresses due to combined waves and currents. In M. Stive, H. de Vriend, J. Fredsøe, L. Hamm, R. Soulsby, C. Teisson, & J. Winterwerp (Eds.), *Advances in coastal morphodynamics* (pp. 20–23). Delft Hydraulics.

Soulsby, R. L. (1997). *Dynamics of marine sands*. Emerald Publishing Limited. https://books.google.nl/books?id=c-1OAAAAMAAJ

Soulsby, R. L., Hamm, L., Klopman, G., Myrhaug, D., Simons, R. R., & Thomas, G. P. (1993). Wave-current interaction within and outside the bottom boundary layer. *Coastal Engineering*, *21*(1-3), 41–69. https://doi.org/10.1016/0378-3839(93)90045-A

Soulsby, R. L., & Whitehouse, R. J. (1997). Threshold of sediment motion in coastal environments. In *Pacific coasts and ports '97: Proceedings of the 13th australasian coastal and ocean engineering conference and the 6th australasian port and harbour conference; volume 1*. Centre for Advanced Engineering, University of Canterbury. https://search.informit.org/doi/10.3316/informit.929741720399033

Soulsby, R. L., & Damgaard, J. S. (2005). Bedload sediment transport in coastal waters. *Coastal Engineering*, *52*(8), 673–689.

Stockdon, H. F., Holman, R. A., Howd, P. A., & Sallenger, A. H. (2006). Empirical parameterization of setup, swash, and runup. *Coastal Engineering*, *53*(7), 573–588. https://doi.org/10.1016/J.COASTALENG.2005.12.005

Stokes, G. G. (1847). On the theory of oscillatory waves. *Trans. Cam. Philos. Soc.*, *8*, 441–455.

Svašek Hydraulics. (2020). *Welcome to finel*. http://www.finel.nl/

Svasek Hydraulics. (2016). *Lekki wave energy analysis* (tech. rep.). Svasek Hydraulics and CDR International.

Svendsen, I. A. (1984). Mass flux and undertow in a surf zone. *Coastal Engineering*, *8*(4), 347–365. https://doi.org/10.1016/0378-3839(84)90030-9

Svendsen, I. A., Madsen, P. A., & Buhr Hansen, J. (1979). Wave characteristics in the surf zone. *Proceedings of the Coastal Engineering Conference*, *1*. https://doi.org/10.9753/icce.v16.29

Sverdrup, H., & Munk, W. (1947). *Wind, sea, and swell: Theory of relations for forecasting*. United States Navy Department.

Swart, D. H. (1974). Offshore Sediment Transport and Equilibrium Beach Profiles. ((December, 1974)).

the SWAN team (Ed.). (2024). *Scientific and technical documentation swan cycle iii*. Version 41.51. https://swanmodel.sourceforge.io/online_doc/swantech/swantech.html

the SWASH team. (2025). *Swash user manual*. Version 11.01.

UNCTAD. (2024). *Review of maritime transport 2024: Overview* (Accessed: 2025-06-06). UNCTAD. https://unctad.org/system/files/official-document/rmt2024overview_en.pdf

van Rijn, L. C. (1984). Sediment Transport, Part I: Bed Load Transport. *Journal of Hydraulic Engineering*, *110*(10). https://doi.org/10.1061/(asce)0733-9429(1984)110:10(1431)

van Rijn, L. C. (2007). Unified view of sediment transport by currents and waves. ii: Suspended transport. *Journal of Hydraulic Engineering*, *6*, 668–689. https://doi.org/10.1061/ASCE0733-942920071 33:6668

van Rooijen, A. (2011). *Modelling sediment transport in the swash zone* [Master's thesis, Delft University of Technology]. https://resolver.tudelft.nl/uuid:632cd1ad-ca43-4289-a7d3-79b134459ed6

van Rooijen, A., Reniers, A. J. H. M., Thiel de Vries, J., Blenkinsopp, C., & McCall, R. (2012). Modeling swash zone sediment transport at truc vert beach. *Coastal Engineering Proceedings*, *1*. https://doi.org/10.9753/icce.v33.sediment.105

van der Westhuysen, A. J., Zijlema, M., & Battjes, J. A. (2007). Nonlinear saturation-based whitecapping dissipation in swan for deep and shallow water. *Coastal Engineering*, *54*(2), 151–170. https://doi.org/https://doi.org/10.1016/j.coastaleng.2006.08.006

van der Lugt, M. A., de Schipper, M. A., Reniers, A. J., & Ruessink, B. G. (2024). Parametrizing nonlinearity in orbital velocity at fetch-limited, low-energy beaches. *Coastal Engineering*, *194*, 104602. https://doi.org/10.1016/J.COASTALENG.2024.104602

van der Reijden, I. (2020). *Modelling refraction of waves over tidal channels: A numerical study focusing on the performance of spectral wave models with respect to bottom refraction* [Master's thesis, Delft University of Technology]. https://resolver.tudelft.nl/uuid:f89e52d0-009d-4a69-9b06-f4216cc065db

Van Rijn, L. C. (2007). Unified view of sediment transport by currents and waves. i: Initiation of motion, bed roughness, and bed-load transport. *Journal of Hydraulic engineering*, *133*(6), 649–667.

Vasarmidis, P., Klonaris, G., Zijlema, M., Stratigaki, V., & Troch, P. (2024). A study of the non-linear properties and wave generation of the multi-layer non-hydrostatic wave model swash. *Ocean Engineering*, *302*, 117633. https://doi.org/https://doi.org/10.1016/j.oceaneng.2024.117633

Wilson, K. C. (1966). Bed-load transport at high shear stress. *Journal of the hydraulics division*, *92*(6), 49–59.

Yap, W. Y., & Lam, J. S. L. (2013). 80 million-twenty-foot-equivalent-unit container port? Sustainability issues in port and coastal development. *Ocean & Coastal Management*, *71*, 13–25. https://doi.org/10.1016/J.OCECOAMAN.2012.10.011

Yoon, H. D., & Cox, D. T. (2010). Large-scale laboratory observations of wave breaking turbulence over an evolving beach. *Journal of Geophysical Research: Oceans*, *115*(10). https://doi.org/10.1029/2009JC005748

Yu, Y.-X., Liu, S.-X., Li, Y. S., & Wai, O. W. H. (2000). Refraction and diffraction of random waves through breakwater. *Ocean Engineering*, *27*(5), 489–509. https://doi.org/https://doi.org/10.1016/S0029-8018(99)00005-0

Zhou, Z., Hsu, T. J., Cox, D., & Liu, X. (2017). Large-eddy simulation of wave-breaking induced turbulent coherent structures and suspended sediment transport on a barred beach. *Journal of Geophysical Research: Oceans*, *122*(1). https://doi.org/10.1002/2016JC011884

Zijlema, M., & Stelling, G. S. (2008). Efficient computation of surf zone waves using the nonlinear shallow water equations with non-hydrostatic pressure. *Coastal Engineering*, *55*(10), 780–790. https://doi.org/10.1016/J.COASTALENG.2008.02.020

Zijlema, M., Stelling, G., & Smit, P. (2011). Swash: An operational public domain code for simulating wave fields and rapidly varied flows in coastal waters. *Coastal Engineering*, *58*(10), 992–1012. https://doi.org/10.1016/j.coastaleng.2011.05.015

Zwamborn, J., & Grieve, G. (1974). Wave attenuation and concentration associated with harbour approach channels. *Coastal Engineering 1984*. https://doi.org/10.1061/9780872621138.123

A Model input files

A.1. Taman case

Listed below are the XBeach input file (listing A.1) and the SWAN input file (listing A.2) for the final run in the Taman case.

Listing A.1: Taman: XBeach input file

```
%%%%%%%%%%%%%%%%%%%%%%%%%%%%%%%%%%%%%%%%%%%%%%%%%%%%%%%%%%%%%%%%
%%% XBeach parameter settings input file                     %%%
%%%                                                          %%%
%%% Date:     april 2025                                     %%%
%%% Delta-Shell XBeach plugin                                %%%
%%%%%%%%%%%%%%%%%%%%%%%%%%%%%%%%%%%%%%%%%%%%%%%%%%%%%%%%%%%%%%%%

%%% Physical processes %%%%%%%%%%%%%%%%%%%%%%%%%%%%%%%%%%%%%%%%%

wavemodel   = nonh
swave       = 0
lwave       = 1
flow        = 1
sedtrans    = 0
morphology  = 0

%%% Grid parameters %%%%%%%%%%%%%%%%%%%%%%%%%%%%%%%%%%%%%%%%%%%%

gridform    = xbeach
xori        = 920
yori        = 0
alfa        = 90
nx          = 2000
ny          = 920
posdwn      = 1
depfile     = bed.dep
vardx       = 0
dx          = 1
dy          = 1

%%% Model time parameters %%%%%%%%%%%%%%%%%%%%%%%%%%%%%%%%%%%%%%%%

tstop       = 3900

%%% Physical constants %%%%%%%%%%%%%%%%%%%%%%%%%%%%%%%%%%%%%%%%%%%

rho         = 1014
g           = 9.81

%%% Wave boundary condition parameters %%%%%%%%%%%%%%%%%%%%%%%%%%%%

wbctype     = swan
bcfile      = swan.txt

%%% Wave-spectrum boundary condition parameters: %%%%%%%%%%%%%%%%%%

dtbc        = 0.5

%%% Flow boundary condition parameters %%%%%%%%%%%%%%%%%%%%%%%%%%%%

front       = nonh_1d
left        = wall
right       = wall
back        = abs_2d

```

```
%%% Tide boundary conditions %%%%%%%%%%%%%%%%%%%%%%%%%%%%%%%%%%%%%%

tideloc     = 0
zs0         = 0.8

%%% Flow parameters %%%%%%%%%%%%%%%%%%%%%%%%%%%%%%%%%%%%%%%%%%%%%%%

bedfriction = manning
bedfriccoef = 0.02

%%% Non-hydrostatic correction parameters %%%%%%%%%%%%%%%%%%%%%%%%%

nonhq3d     = 1
maxbrsteep  = 0.6
reformsteep = 0.3

%%% Output variables %%%%%%%%%%%%%%%%%%%%%%%%%%%%%%%%%%%%%%%%%%%%%%

tstart      = 300
tintg       = 100
tintp       = .5
tintm       = 3600

nglobalvar  = 19
H
zs
zs0
zb
hh
u
v
ue
ve
urms
Fx
Fy
ccg
ceqsg
ceqbg
Susg
Svsg
E
R
D
DR

npoints     = 10
229.6000      616.9000
270.4000     1206.8000
447.3000     1489.4000
685.7000     1612.3000
798.8000     1415.7000
366.2000      993.0000
575.1000     1199.4000
484.2000     1415.7000
685.7000      941.3000
589.9000     1808.9000

npointvar   = 5
zs
u
v
ue
uv

nmeanvar    = 6
zs
u
v
ue
uv
```

```
E

%%% Output projection %%%%%%%%%%%%%%%%%%%%%%%%%%%%%%%%%%%%%%%%%%%%%

rotate      = 1

%%% Wave numerics parameters %%%%%%%%%%%%%%%%%%%%%%%%%%%%%%%%%%%%%%

snells      = 0
```

Listing A.2: Taman: SWAN input file (Dusseljee et al., 2014)

```

$***************************** HEADING *****************************
$
PROJECT  ' ' ' '
$
$************************************* GENERAL SETTINGS*************
$
SET LEVEL = 0.8   NOR =  90.00    DEPMIN =   0.001 _
        MAXMES = 1000   MAXERR = 2 _
        GRAV =    9.81  RHO =  1014.00  INRHOG =      0 _
        NAUT

MODE STATIONARY TWODIMENSIONAL
COORD CART

$************************************* MODEL SETUP********************
$ READ GRID
   CGRID REG 0 0 0 921 3501 307 1167 CIR 72 0.04 1.00

$ READ BATHYMETRY
        INPGRID BOT REG 0 0 0 184 600 5 5 EXC -99
        READINP BOT -1 'impbar_B.bot' 4 0 FREE

$ READ WIND
        WIND 5 180

$************************************* BOUNDARY CONDITIONS **********
BOUN SHAP JON PEAK DSPR DEGR
BOUN SIDE SOUTH CON FILE 'RP1_1D.spc'
$***************************** PHYSICS *****************************
GEN3 WESTH
WCAP AB cds2=5.0e-05 br=0.00175 CUR 0.8
QUAD iquad=2 lambda=0.25 Cnl4=3.0e+07
LIMITER ursell=10.0 qb=1.0
FRIC JONSWAP cfjon=0.0380000
BRE CONSTANT
TRIAD trfac=0.1 p=2.

NUM STOPC 0.00 0.02 0.01 101 STAT 50
$********************* OBSTACLES *********************************

$ Breakwater
OBST DAM DANGremond 5.8 33.7 16 REFL 0.42 LINE 924.92 1935.00 867.90 1898.04
OBST DAM DANGremond 5.8 33.7 16 REFL 0.42 LINE 867.90 1898.04 829.78 1874.29
OBST DAM DANGremond 5.8 33.7 16 REFL 0.42 LINE 829.78 1874.29 776.74 1842.52
OBST DAM DANGremond 5.8 33.7 16 REFL 0.42 LINE 776.74 1842.52 734.87 1818.69
OBST DAM DANGremond 5.8 33.7 16 REFL 0.42 LINE 734.87 1818.69 700.00 1799.25
OBST DAM DANGremond 5.8 33.7 16 REFL 0.42 LINE 700.00 1799.25 682.16 1789.53
OBST DAM DANGremond 5.8 33.7 16 REFL 0.42 LINE 682.16 1789.53 679.13 1788.59
OBST DAM DANGremond 5.8 33.7 16 REFL 0.42 LINE 679.13 1788.59 676.04 1788.42
OBST DAM DANGremond 5.8 33.7 16 REFL 0.42 LINE 676.04 1788.42 670.42 1788.41
OBST DAM DANGremond 5.8 33.7 16 REFL 0.42 LINE 670.42 1788.41 667.20 1787.59
OBST DAM DANGremond 5.8 33.7 16 REFL 0.42 LINE 667.20 1787.59 654.55 1780.75
OBST DAM DANGremond 5.8 33.7 16 REFL 0.42 LINE 654.55 1780.75 650.08 1778.40
OBST DAM DANGremond 5.8 33.7 16 REFL 0.42 LINE 650.08 1778.40 647.99 1775.80
OBST DAM DANGremond 5.8 33.7 16 REFL 0.42 LINE 647.99 1775.80 645.84 1772.95
OBST DAM DANGremond 5.8 33.7 16 REFL 0.42 LINE 645.84 1772.95 643.96 1770.36
OBST DAM DANGremond 5.8 33.7 16 REFL 0.42 LINE 643.96 1770.36 639.59 1766.92
OBST DAM DANGremond 5.8 33.7 16 REFL 0.42 LINE 639.59 1766.92 633.34 1762.85
```

```
OBST DAM DANGremond 5.8 33.7 16 REFL 0.42 LINE 633.34 1762.85 621.96 1755.24
OBST DAM DANGremond 5.8 33.7 16 REFL 0.42 LINE 621.96 1755.24 601.29 1742.26
OBST DAM DANGremond 5.8 33.7 16 REFL 0.42 LINE 601.29 1742.26 589.08 1735.91
OBST DAM DANGremond 5.8 33.7 16 REFL 0.42 LINE 589.08 1735.91 579.13 1731.32
OBST DAM DANGremond 5.8 33.7 16 REFL 0.42 LINE 579.13 1731.32 574.65 1729.07
OBST DAM DANGremond 5.8 33.7 16 REFL 0.42 LINE 574.65 1729.07 569.60 1725.59
OBST DAM DANGremond 5.8 33.7 16 REFL 0.42 LINE 569.60 1725.59 567.05 1722.73
OBST DAM DANGremond 5.8 33.7 16 REFL 0.42 LINE 567.05 1722.73 564.52 1718.84
OBST DAM DANGremond 5.8 33.7 16 REFL 0.42 LINE 564.52 1718.84 563.48 1715.70
OBST DAM DANGremond 5.8 33.7 16 REFL 0.42 LINE 563.48 1715.70 562.54 1712.04
OBST DAM DANGremond 5.8 33.7 16 REFL 0.42 LINE 562.54 1712.04 562.48 1708.19
OBST DAM DANGremond 5.8 33.7 16 REFL 0.42 LINE 562.48 1708.19 562.78 1704.56
OBST DAM DANGremond 5.8 33.7 16 REFL 0.42 LINE 562.78 1704.56 564.23 1699.97
OBST DAM DANGremond 5.8 33.7 16 REFL 0.42 LINE 564.23 1699.97 566.14 1696.10
OBST DAM DANGremond 5.8 33.7 16 REFL 0.42 LINE 566.14 1696.10 569.21 1692.33
OBST DAM DANGremond 5.8 33.7 16 REFL 0.42 LINE 569.21 1692.33 573.03 1689.35
OBST DAM DANGremond 5.8 33.7 16 REFL 0.42 LINE 573.03 1689.35 576.92 1687.67
OBST DAM DANGremond 5.8 33.7 16 REFL 0.42 LINE 576.92 1687.67 580.81 1686.45
OBST DAM DANGremond 5.8 33.7 16 REFL 0.42 LINE 580.81 1686.45 584.88 1685.91
OBST DAM DANGremond 5.8 33.7 16 REFL 0.42 LINE 584.88 1685.91 588.97 1686.08
OBST DAM DANGremond 5.8 33.7 16 REFL 0.42 LINE 588.97 1686.08 592.58 1686.89
OBST DAM DANGremond 5.8 33.7 16 REFL 0.42 LINE 592.58 1686.89 596.94 1688.83
OBST DAM DANGremond 5.8 33.7 16 REFL 0.42 LINE 596.94 1688.83 607.76 1694.73
OBST DAM DANGremond 5.8 33.7 16 REFL 0.42 LINE 607.76 1694.73 619.48 1700.92
OBST DAM DANGremond 5.8 33.7 16 REFL 0.42 LINE 619.48 1700.92 634.03 1708.05
OBST DAM DANGremond 5.8 33.7 16 REFL 0.42 LINE 634.03 1708.05 653.84 1718.10
OBST DAM DANGremond 5.8 33.7 16 REFL 0.42 LINE 653.84 1718.10 679.13 1731.08
OBST DAM DANGremond 5.8 33.7 16 REFL 0.42 LINE 679.13 1731.08 707.23 1746.27
OBST DAM DANGremond 5.8 33.7 16 REFL 0.42 LINE 707.23 1746.27 734.60 1761.04
OBST DAM DANGremond 5.8 33.7 16 REFL 0.42 LINE 734.60 1761.04 756.07 1772.97
OBST DAM DANGremond 5.8 33.7 16 REFL 0.42 LINE 756.07 1772.97 788.45 1791.31
OBST DAM DANGremond 5.8 33.7 16 REFL 0.42 LINE 788.45 1791.31 823.84 1812.09
OBST DAM DANGremond 5.8 33.7 16 REFL 0.42 LINE 823.84 1812.09 876.44 1844.31
OBST DAM DANGremond 5.8 33.7 16 REFL 0.42 LINE 876.44 1844.31 906.80 1863.45
OBST DAM DANGremond 5.8 33.7 16 REFL 0.42 LINE 906.80 1863.45 925.45 1875.49
OBST DAM DANGremond 5.8 33.7 16 REFL 0.42 LINE 925.45 1875.49 924.92 1935.00
$ NEW LDB
OBST DAM DANGremond 5.8 33.7 16 REFL 0.42 LINE   0.06 1621.93  73.92 1522.66
OBST DAM DANGremond 5.8 33.7 16 REFL 0.42 LINE  73.92 1522.66 100.68 1487.07
OBST DAM DANGremond 5.8 33.7 16 REFL 0.42 LINE 100.68 1487.07 140.46 1435.56
OBST DAM DANGremond 5.8 33.7 16 REFL 0.42 LINE 140.46 1435.56 175.29 1390.08
OBST DAM DANGremond 5.8 33.7 16 REFL 0.42 LINE 175.29 1390.08 218.95 1334.92
OBST DAM DANGremond 5.8 33.7 16 REFL 0.42 LINE 218.95 1334.92 248.77 1298.10
OBST DAM DANGremond 5.8 33.7 16 REFL 0.42 LINE 248.77 1298.10 257.62 1286.35
OBST DAM DANGremond 5.8 33.7 16 REFL 0.42 LINE 257.62 1286.35 260.30 1282.24
OBST DAM DANGremond 5.8 33.7 16 REFL 0.42 LINE 260.30 1282.24 263.45 1278.28
OBST DAM DANGremond 5.8 33.7 16 REFL 0.42 LINE 263.45 1278.28 265.56 1275.34
OBST DAM DANGremond 5.8 33.7 16 REFL 0.42 LINE 265.56 1275.34 268.53 1273.02
OBST DAM DANGremond 5.8 33.7 16 REFL 0.42 LINE 268.53 1273.02 271.21 1271.33
OBST DAM DANGremond 5.8 33.7 16 REFL 0.42 LINE 271.21 1271.33 274.52 1270.12
OBST DAM DANGremond 5.8 33.7 16 REFL 0.42 LINE 274.52 1270.12 277.21 1269.14
OBST DAM DANGremond 5.8 33.7 16 REFL 0.42 LINE 277.21 1269.14 279.92 1268.85
OBST DAM DANGremond 5.8 33.7 16 REFL 0.42 LINE 279.92 1268.85 282.58 1268.54
OBST DAM DANGremond 5.8 33.7 16 REFL 0.42 LINE 282.58 1268.54 287.14 1269.21
OBST DAM DANGremond 5.8 33.7 16 REFL 0.42 LINE 287.14 1269.21 292.47 1271.02
OBST DAM DANGremond 5.8 33.7 16 REFL 0.42 LINE 292.47 1271.02 296.02 1273.30
OBST DAM DANGremond 5.8 33.7 16 REFL 0.42 LINE 296.02 1273.30 299.12 1275.78
OBST DAM DANGremond 5.8 33.7 16 REFL 0.42 LINE 299.12 1275.78 301.07 1278.29
OBST DAM DANGremond 5.8 33.7 16 REFL 0.42 LINE 301.07 1278.29 302.58 1280.44
OBST DAM DANGremond 5.8 33.7 16 REFL 0.42 LINE 302.58 1280.44 303.31 1282.01
OBST DAM DANGremond 5.8 33.7 16 REFL 0.42 LINE 303.31 1282.01 304.30 1284.32
OBST DAM DANGremond 5.8 33.7 16 REFL 0.42 LINE 304.30 1284.32 305.09 1288.35
OBST DAM DANGremond 5.8 33.7 16 REFL 0.42 LINE 305.09 1288.35 305.36 1292.66
OBST DAM DANGremond 5.8 33.7 16 REFL 0.42 LINE 305.36 1292.66 304.78 1296.25
OBST DAM DANGremond 5.8 33.7 16 REFL 0.42 LINE 304.78 1296.25 304.02 1299.28
OBST DAM DANGremond 5.8 33.7 16 REFL 0.42 LINE 304.02 1299.28 302.49 1302.90
OBST DAM DANGremond 5.8 33.7 16 REFL 0.42 LINE 302.49 1302.90 300.02 1306.32
OBST DAM DANGremond 5.8 33.7 16 REFL 0.42 LINE 300.02 1306.32 294.49 1312.72
OBST DAM DANGremond 5.8 33.7 16 REFL 0.42 LINE 294.49 1312.72 287.44 1321.00
OBST DAM DANGremond 5.8 33.7 16 REFL 0.42 LINE 287.44 1321.00 282.04 1328.28
OBST DAM DANGremond 5.8 33.7 16 REFL 0.42 LINE 282.04 1328.28 273.64 1340.75
```

```
OBST DAM DANGremond 5.8 33.7 16 REFL 0.42 LINE 273.64 1340.75 268.34 1349.69
OBST DAM DANGremond 5.8 33.7 16 REFL 0.42 LINE 268.34 1349.69 262.91 1358.11
OBST DAM DANGremond 5.8 33.7 16 REFL 0.42 LINE 262.91 1358.11 257.24 1366.96
OBST DAM DANGremond 5.8 33.7 16 REFL 0.42 LINE 257.24 1366.96 255.17 1369.92
OBST DAM DANGremond 5.8 33.7 16 REFL 0.42 LINE 255.17 1369.92 254.24 1372.39
OBST DAM DANGremond 5.8 33.7 16 REFL 0.42 LINE 254.24 1372.39 253.84 1374.81
OBST DAM DANGremond 5.8 33.7 16 REFL 0.42 LINE 253.84 1374.81 252.62 1380.34
OBST DAM DANGremond 5.8 33.7 16 REFL 0.42 LINE 252.62 1380.34 251.88 1381.99
OBST DAM DANGremond 5.8 33.7 16 REFL 0.42 LINE 251.88 1381.99 251.03 1383.46
OBST DAM DANGremond 5.8 33.7 16 REFL 0.42 LINE 251.03 1383.46 238.82 1398.35
OBST DAM DANGremond 5.8 33.7 16 REFL 0.42 LINE 238.82 1398.35 237.44 1399.29
OBST DAM DANGremond 5.8 33.7 16 REFL 0.42 LINE 237.44 1399.29 235.89 1400.13
OBST DAM DANGremond 5.8 33.7 16 REFL 0.42 LINE 235.89 1400.13 232.07 1401.73
OBST DAM DANGremond 5.8 33.7 16 REFL 0.42 LINE 232.07 1401.73 229.80 1402.96
OBST DAM DANGremond 5.8 33.7 16 REFL 0.42 LINE 229.80 1402.96 228.06 1404.50
OBST DAM DANGremond 5.8 33.7 16 REFL 0.42 LINE 228.06 1404.50 221.99 1412.08
OBST DAM DANGremond 5.8 33.7 16 REFL 0.42 LINE 221.99 1412.08 214.19 1421.89
OBST DAM DANGremond 5.8 33.7 16 REFL 0.42 LINE 214.19 1421.89 203.58 1435.51
OBST DAM DANGremond 5.8 33.7 16 REFL 0.42 LINE 203.58 1435.51 184.22 1460.36
OBST DAM DANGremond 5.8 33.7 16 REFL 0.42 LINE 184.22 1460.36 166.37 1483.43
OBST DAM DANGremond 5.8 33.7 16 REFL 0.42 LINE 166.37 1483.43 147.53 1508.46
OBST DAM DANGremond 5.8 33.7 16 REFL 0.42 LINE 147.53 1508.46 135.86 1523.66
OBST DAM DANGremond 5.8 33.7 16 REFL 0.42 LINE 135.86 1523.66 124.29 1539.03
OBST DAM DANGremond 5.8 33.7 16 REFL 0.42 LINE 124.29 1539.03 111.15 1556.51
OBST DAM DANGremond 5.8 33.7 16 REFL 0.42 LINE 111.15 1556.51  98.84 1573.07
OBST DAM DANGremond 5.8 33.7 16 REFL 0.42 LINE  98.84 1573.07  83.80 1593.37
OBST DAM DANGremond 5.8 33.7 16 REFL 0.42 LINE  83.80 1593.37  65.26 1618.35
OBST DAM DANGremond 5.8 33.7 16 REFL 0.42 LINE  65.26 1618.35  43.82 1647.54
OBST DAM DANGremond 5.8 33.7 16 REFL 0.42 LINE  43.82 1647.54  25.82 1672.59
OBST DAM DANGremond 5.8 33.7 16 REFL 0.42 LINE  25.82 1672.59   1.23 1706.66
OBST DAM DANGremond 5.8 33.7 16 REFL 0.42 LINE   1.23 1706.66   0.06 1621.93

$ BOUNDARIES REFLECTIVE
OBST TRANS 0 REFL 0.85 LINE 1 0 1 3501
OBST TRANS 0 REFL 0.85 LINE 920 0 920 3501
$***************************** OUTPUT REQUEST ***********************
QUANT Hswell fswell = 0.13
OUTPUT OPTIONS '%' TABLE 16 BLOCK 9 1000 SPEC  8

POINTS 'Deltares'       FILE    'out_pnts/Dpoints.pnt'  $ Deltares' observation points
POINTS 'GRSM1'          FILE    'out_pnts/GRSM1.pnt'            $ points around GRSM1
POINTS 'GRSM2'          FILE    'out_pnts/GRSM2.pnt'            $ points around GRSM2
POINTS 'GRSM3'          FILE    'out_pnts/GRSM3.pnt'            $ points around GRSM3
POINTS 'GRSM4'          FILE    'out_pnts/GRSM4.pnt'            $ points around GRSM4
POINTS 'WHM01'          FILE    'out_pnts/WHM01.pnt'            $ points around WHM01
POINTS 'WHM02'          FILE    'out_pnts/WHM02.pnt'            $ points around WHM02
POINTS 'WHM03'          FILE    'out_pnts/WHM03.pnt'            $ points around WHM03
POINTS 'WHM04'          FILE    'out_pnts/WHM04.pnt'            $ points around WHM04
POINTS 'WHM05'          FILE    'out_pnts/WHM05.pnt'            $ points around WHM05
POINTS 'WHM07'          FILE    'out_pnts/WHM07.pnt'            $ points around WHM07
POINTS 'channel'        FILE 'out_pnts/chnlaxis.pnt'            $ points along channel axis
POINTS 'WBWtrans'       FILE 'out_pnts/WBWcross.pnt'            $ transmission trough west BW
POINTS 'EBWtrans'       FILE 'out_pnts/EBWcross.pnt'            $ transmission trough west EW
$
BLOCK 'COMPGRID'        NOHEAD 'total.mat'              XP YP HSIGN DIR TPS PDIR BOTLEV DHSIGN TM02 TMM10 TM01 QB DSPR WATLEV
$
TABLE 'Deltares'        NOHEAD 'Deltares.tbl'   XP YP HSIGN HSWELL DIR TPS PDIR DEPTH BOTLEV DHSIGN TM02 TMM10 TM01 &
                                            QB DSPR FSPR WLEN STEEPNESS URMS UBOT TMBOT WATLEV
TABLE 'GRSM1'           NOHEAD 'GRSM1.tbl'              XP YP HSIGN DIR TPS PDIR DEPTH BOTLEV DHSIGN TM02 TMM10 TM01 &
                                            QB DSPR FSPR WLEN STEEPNESS WIND URMS UBOT TMBOT WATLEV
TABLE 'GRSM2'           NOHEAD 'GRSM2.tbl'              XP YP HSIGN DIR TPS PDIR DEPTH BOTLEV DHSIGN TM02 TMM10 TM01 &
                                            QB DSPR FSPR WLEN STEEPNESS WIND URMS UBOT TMBOT WATLEV
TABLE 'GRSM3'           NOHEAD 'GRSM3.tbl'              XP YP HSIGN DIR TPS PDIR DEPTH BOTLEV DHSIGN TM02 TMM10 TM01 &
```

```
                                            QB DSPR FSPR WLEN STEEPNESS WIND URMS UBOT TMBOT WATLEV
TABLE 'GRSM4'           NOHEAD 'GRSM4.tbl'              XP YP HSIGN DIR TPS PDIR DEPTH BOTLEV DHSIGN TM02 TMM10 TM01 &
                                            QB DSPR FSPR WLEN STEEPNESS WIND URMS UBOT TMBOT WATLEV
TABLE 'WHM01'           NOHEAD 'WHM01.tbl'              XP YP HSIGN DIR TPS PDIR DEPTH BOTLEV DHSIGN TM02 TMM10 TM01 &
                                            QB DSPR FSPR WLEN STEEPNESS WIND URMS UBOT TMBOT WATLEV
TABLE 'WHM02'           NOHEAD 'WHM02.tbl'              XP YP HSIGN DIR TPS PDIR DEPTH BOTLEV DHSIGN TM02 TMM10 TM01 &
                                            QB DSPR FSPR WLEN STEEPNESS WIND URMS UBOT TMBOT WATLEV
TABLE 'WHM03'           NOHEAD 'WHM03.tbl'              XP YP HSIGN DIR TPS PDIR DEPTH BOTLEV DHSIGN TM02 TMM10 TM01 &
                                            QB DSPR FSPR WLEN STEEPNESS WIND URMS UBOT TMBOT WATLEV
TABLE 'WHM04'           NOHEAD 'WHM04.tbl'              XP YP HSIGN DIR TPS PDIR DEPTH BOTLEV DHSIGN TM02 TMM10 TM01 &
                                            QB DSPR FSPR WLEN STEEPNESS WIND URMS UBOT TMBOT WATLEV
TABLE 'WHM05'           NOHEAD 'WHM05.tbl'              XP YP HSIGN DIR TPS PDIR DEPTH BOTLEV DHSIGN TM02 TMM10 TM01 &
                                            QB DSPR FSPR WLEN STEEPNESS WIND URMS UBOT TMBOT WATLEV
TABLE 'WHM07'           NOHEAD 'WHM07.tbl'              XP YP HSIGN DIR TPS PDIR DEPTH BOTLEV DHSIGN TM02 TMM10 TM01 &
                                            QB DSPR FSPR WLEN STEEPNESS WIND URMS UBOT TMBOT WATLEV
TABLE 'channel'         NOHEAD 'channel.tbl'    XP YP HSIGN DIR TPS PDIR DEPTH BOTLEV DHSIGN TM02 TMM10 TM01 &
                                            QB DSPR FSPR WLEN STEEPNESS WIND URMS UBOT TMBOT WATLEV
TABLE 'WBWtrans'        NOHEAD 'westBW.tbl'     XP YP HSIGN DIR TPS PDIR DEPTH BOTLEV DHSIGN TM02 TMM10 TM01 &
                                            QB DSPR FSPR WLEN STEEPNESS WIND URMS UBOT TMBOT WATLEV
TABLE 'EBWtrans'        NOHEAD 'eastBW.tbl'     XP YP HSIGN DIR TPS PDIR DEPTH BOTLEV DHSIGN TM02 TMM10 TM01 &
                                            QB DSPR FSPR WLEN STEEPNESS WIND URMS UBOT TMBOT WATLEV

SPECOUT 'Deltares' SPEC1D ABS 'spec1D.s1d'
SPECOUT 'Deltares' SPEC2D ABS 'spec2D.s2d'

TEST 1 0

$****************************** START COMPUTE **************************

COMPUTE STATIONARY

STOP
```

A.2. Synthetic case

Listed below are the XBeach input file (listing A.3), the FINEL input file (listing A.4), and the SWAN file with which it is coupled (listing A.5) for the model runs with the synthetic case.

Listing A.3: Syntetic case: XBeach input file

```
%%%%%%%%%%%%%%%%%%%%%%%%%%%%%%%%%%%%%%%%%%%%%%%%%%%%%%%%%%%%%%%%
%%% XBeach parameter settings input file                     %%%
%%%                                                          %%%
%%% Date:  june 2025                                         %%%
%%% Delta-Shell XBeach plugin                                %%%
%%%%%%%%%%%%%%%%%%%%%%%%%%%%%%%%%%%%%%%%%%%%%%%%%%%%%%%%%%%%%%%%

%%% Physical processes %%%%%%%%%%%%%%%%%%%%%%%%%%%%%%%%%%%%%%%%%

```

```
wavemodel   = nonh
swave       = 0
lwave       = 1
flow        = 1
sedtrans    = 0
morphology  = 0

%%% Grid parameters %%%%%%%%%%%%%%%%%%%%%%%%%%%%%%%%%%%%%%%%%%%%

gridform    = xbeach
xori        = 0
yori        = 0
alfa        = 0
nx          = 2000
ny          = 1500
dx          = 1
dy          = 2
posdwn      = 1
depfile     = bed.dep
vardx       = 0

%%% Model time parameters %%%%%%%%%%%%%%%%%%%%%%%%%%%%%%%%%%%%%%%%

tstop       = 6000

%%% Physical constants %%%%%%%%%%%%%%%%%%%%%%%%%%%%%%%%%%%%%%%%%%%

rho         = 1014
g           = 9.81

%%% Wave boundary condition parameters %%%%%%%%%%%%%%%%%%%%%%%%%%%%

wbctype     = jonstable
bcfile      = jonswap.txt

%%% Wave-spectrum boundary condition parameters: %%%%%%%%%%%%%%%%%%

dtbc        = 0.5

%%% Flow boundary condition parameters %%%%%%%%%%%%%%%%%%%%%%%%%%%%

front       = nonh_1d
left        = neumann
right       = neumann
back        = abs_2d
cyclic      = 1

%%% Tide boundary conditions %%%%%%%%%%%%%%%%%%%%%%%%%%%%%%%%%%%%%%

tideloc     = 0
zs0         = 0

%%% Flow parameters %%%%%%%%%%%%%%%%%%%%%%%%%%%%%%%%%%%%%%%%%%%%%%%

bedfriction = manning
bedfriccoef = 0.02

%%% Non-hydrostatic correction parameters %%%%%%%%%%%%%%%%%%%%%%%%%

nonhq3d     = 1
maxbrsteep  = 0.6
reformsteep = 0.3

%%% Bed composition parameter %%%%%%%%%%%%%%%%%%%%%%%%%%%%%%%%%%%%%

d50         = 0.001
d90         = 0.002

%%% Output variables %%%%%%%%%%%%%%%%%%%%%%%%%%%%%%%%%%%%%%%%%%%%%%

outputformat= fortran
```

```

tstart      = 2400
tintg       = 1
tintm       = 3600
tintp       = 0.5

nglobalvar  = 3
zs
taubx
tauby

npoints     = 10
10.     500.
1000.   500.
1300.   500.
1400.   500.
1500.   500.
1550.   500.
1600.   500.
1650.   500.
1700.   500.
1750.   500.

npointvar = 1
zs

nmeanvar    = 5
zs
ue
ve
taubx
tauby

%%% Output projection %%%%%%%%%%%%%%%%%%%%%%%%%%%%%%%%%%%%%%%%%%%%%

rotate      = 1

%%% Wave numerics parameters %%%%%%%%%%%%%%%%%%%%%%%%%%%%%%%%%%%%%%

snells      = 0
```

Listing A.4: Synthetic case: FINEL input file

```
!=======================================================================
!= FINEL 2D INPUT FILE: fininp.Nxx
!= proj: channel refraction
!= june 2025
!=======================================================================
!  (c) Svasek Hydraulics
!  P.O. Box 91
!  3000 AB Rotterdam
!  The Netherlands
!
!
!  website: http://www.svasek.com
!
!=======================================================================

&runinfo ! general run info
! place a short description of the run here
comment=''
status='draft' ! status of the run: test/draft/final
/

&modtype
modeltype=3
runswan='on'
!1=flow,2=flow+silt,3=flow+sand,4=flow+silt+sand (no interaction),5=flow+silt-sand interaction
/

```

```
&general
meshfname='./Inputfiles/Run_1_exp.out'
depthfname='./Inputfiles/Run_1_exp.bot'
roughnesstype='manning'
globalroughness=0.02
number_of_processors=16
list_timestep_info='off'
flowmap_outputname='datestring'
/

&times
year=2020
month=01
day=1
hour=0
min=0
sec=0
tbeg=0
tend=7200
tmap=0,120, 7200
this=0,60, 7200
/

&flowconstants
gravity=9.81 ! [m/s2]
drycrit=0.05 ! critical waterdepth for drying [m]
rho_water=1014 ! water density [kg/m3]
temperature=13
latitude=0
/

&meteo
windsp_x=0
windsp_y=0
/

&morphology
morfstart=10000
xmin    = 0
xmax    = 2000
ymin    = 0
ymax    = 4500
/

&sedimenttransport
formula = 'meyer_peter_mueller'
wave_stokes_drift ='on'
wave_form='ruessink_vanrijn'
facAs=0.20
facSk=0.15
/

&sedimentfractions
fract(1)%fractype=1
fract(1)%d50=0.001
fract(1)%d90=0.002
fract(1)%rho_sand=2650
fract(1)%eps = 0.40
/

&multilayer_parameters
/

&swan
nomatlab = 'on'
swantemplate= './Inputfiles/T01_vFDW_varboun.swn'
xpc=0.0         ! x-origin of SWAN grid
ypc=0.0         ! y-origin of SWAN grid
xlenc=2000      ! x-length of SWAN grid
ylenc=4500      ! y-length of SWAN grid
mxc=1000        ! no of grid cells in x direction
```

```
myc=900         ! no of grid cells in y direction
alpc=0.0        ! angle of SWAN grid (grid will be rotated counter clockwise)
roller_model = 'on'


wavecondition(1).varinput1 = 1.50
wavecondition(1).varinput2 = 10.00
wavecondition(1).varinput3 = 290.00
wavecondition(1).varinput4 = 20.00
wavecondition(1).varinput5 = Run_5
wavecondition(1).tbeg =         0
wavecondition(1).tend =       600

wavecondition(2).varinput1 = 1.50
wavecondition(2).varinput2 = 10.00
wavecondition(2).varinput3 = 290.00
wavecondition(2).varinput4 = 20.00
wavecondition(2).varinput5 = Run_5
wavecondition(2).tbeg =       600
wavecondition(2).tend =      1200

wavecondition(3).varinput1 = 1.50
wavecondition(3).varinput2 = 10.00
wavecondition(3).varinput3 = 290.00
wavecondition(3).varinput4 = 20.00
wavecondition(3).varinput5 = Run_5
wavecondition(3).tbeg =      1200
wavecondition(3).tend =      1800

wavecondition(4).varinput1 = 1.50
wavecondition(4).varinput2 = 10.00
wavecondition(4).varinput3 = 290.00
wavecondition(4).varinput4 = 20.00
wavecondition(4).varinput5 = Run_5
wavecondition(4).tbeg =      1800
wavecondition(4).tend =      2400

wavecondition(5).varinput1 = 1.50
wavecondition(5).varinput2 = 10.00
wavecondition(5).varinput3 = 290.00
wavecondition(5).varinput4 = 20.00
wavecondition(5).varinput5 = Run_5
wavecondition(5).tbeg =      2400
wavecondition(5).tend =      3000

wavecondition(6).varinput1 = 1.50
wavecondition(6).varinput2 = 10.00
wavecondition(6).varinput3 = 290.00
wavecondition(6).varinput4 = 20.00
wavecondition(6).varinput5 = Run_5
wavecondition(6).tbeg =      3000
wavecondition(6).tend =      3600

wavecondition(7).varinput1 = 1.50
wavecondition(7).varinput2 = 10.00
wavecondition(7).varinput3 = 290.00
wavecondition(7).varinput4 = 20.00
wavecondition(7).varinput5 = Run_5
wavecondition(7).tbeg =      3600
wavecondition(7).tend =      4200

wavecondition(8).varinput1 = 1.50
wavecondition(8).varinput2 = 10.00
wavecondition(8).varinput3 = 290.00
wavecondition(8).varinput4 = 20.00
wavecondition(8).varinput5 = Run_5
wavecondition(8).tbeg =      4200
wavecondition(8).tend =      4800

wavecondition(9).varinput1 = 1.50
wavecondition(9).varinput2 = 10.00
```

```
wavecondition(9).varinput3 = 290.00
wavecondition(9).varinput4 = 20.00
wavecondition(9).varinput5 = Run_5
wavecondition(9).tbeg =       4800
wavecondition(9).tend =       5400

wavecondition(10).varinput1 = 1.50
wavecondition(10).varinput2 = 10.00
wavecondition(10).varinput3 = 290.00
wavecondition(10).varinput4 = 20.00
wavecondition(10).varinput5 = Run_5
wavecondition(10).tbeg =       5400
wavecondition(10).tend =       6000

wavecondition(11).varinput1 = 1.50
wavecondition(11).varinput2 = 10.00
wavecondition(11).varinput3 = 290.00
wavecondition(11).varinput4 = 20.00
wavecondition(11).varinput5 = Run_5
wavecondition(11).tbeg =       6000
wavecondition(11).tend =       6600

wavecondition(12).varinput1 = 1.50
wavecondition(12).varinput2 = 10.00
wavecondition(12).varinput3 = 290.00
wavecondition(12).varinput4 = 20.00
wavecondition(12).varinput5 = Run_5
wavecondition(12).tbeg =       6600
wavecondition(12).tend =       7200



/

&sandsiltinteraction
/

&wavefields
/

&roughfields
/

&initcond
! initial conditions are only used when no restart file is supplied
hinit=0
uinit=0
vinit=0
/

&histories
/

&boundcond
bc(1)%cnr=4
bc(1)%btype= 'neumann'

bc(2)%cnr=1
bc(2)%btype= 'neumann'

bc(3)%cnr=2
bc(3)%btype= 'neumann'
/
```

Listing A.5: Synthetic case: SWAN input file

```

$***************************** HEADING *****************************
$
PROJECT  ' ' ' '
$
```

```
$************************************* GENERAL SETTINGS*************
$
SET NOR =  90.00    DEPMIN =   0.001 _
        MAXMES = 1000   MAXERR = 2 _
        GRAV =    9.81  RHO =  1014.00  INRHOG =      0 _
        NAUT

MODE STATIONARY TWODIMENSIONAL
COORD CART

$************************************* MODEL SETUP********************
$ READ GRID
   CGRID REG 0 0 0 2000 4500 1000 900 CIR 72 0.04 1.00

$ READ BATHYMETRY
    INPGRID BOT REG 0 0 0 1000 900 2 5
    READINP BOT 1 'swan.bot' IDLA=3  NHEDF=0 FREE

$ READ WATER LEVEL
    INP   WLEVEL REG 0 0 0 1000 900 2 5
    READ  WLEVEL 1.  'swan.lev'   IDLA=3  NHEDF=0 FREE

$ READ WIND
$       WIND 5 270

$************************************* BOUNDARY CONDITIONS **********
BOUN SHAP JON PEAK DSPR POWER
BOU SIDE W CON PAR                  1.5 10. 290 20
BOU SIDE N CLOCKWISE VAR PAR 0.     1.5 10. 290 20 &
                             1000.  1.5 10. 290 20 &
                             1300.  0.  10. 290 20

$***************************** PHYSICS *****************************
OFF WINDG
OFF WCAP
OFF QUAD
LIMITER ursell=10.0 qb=1.0
FRIC JONSWAP cfjon=0.0380000
BRE CONSTANT
TRIAD

NUM STOPC 0.00 0.02 0.01 99 STAT 50

$
BLOCK 'COMPGRID' NOHEAD  'XP.mat'     LAY-OUT 3 XP
BLOCK 'COMPGRID' NOHEAD  'YP.mat'     LAY-OUT 3 YP
BLOCK 'COMPGRID' NOHEAD  'DE.mat'     LAY-OUT 3 DEPTH
BLOCK 'COMPGRID' NOHEAD  'HS.mat'     LAY-OUT 3 HSIGN
BLOCK 'COMPGRID' NOHEAD  'TPS.mat'    LAY-OUT 3 TPS
BLOCK 'COMPGRID' NOHEAD  'DIR.mat'    LAY-OUT 3 DIR
BLOCK 'COMPGRID' NOHEAD  'FO.mat'     LAY-OUT 3 FORCE
BLOCK 'COMPGRID' NOHEAD  'UBOT.mat'   LAY-OUT 3 UBOT
BLOCK 'COMPGRID' NOHEAD  'TP.mat'     LAY-OUT 3 RTP
BLOCK 'COMPGRID' NOHEAD  'WL.mat'     LAY-OUT 3 WATLEV
BLOCK 'COMPGRID' NOHEAD  'VE.mat'     LAY-OUT 3 VEL
BLOCK 'COMPGRID' NOHEAD  'URMS.mat'     LAY-OUT 3 URMS
BLOCK 'COMPGRID' NOHEAD  'DISSURF.mat'  LAY-OUT 3 DISSURF
BLOCK 'COMPGRID' NOHEAD  'TM01.mat'     LAY-OUT 3 TM01
BLOCK 'COMPGRID' NOHEAD  'WLEN.mat'     LAY-OUT 3 WLEN
BLOCK 'COMPGRID' NOHEAD  'DSPR.mat'     LAY-OUT 3 DSPR

$***************************** START COMPUTE **************************

COMPUTE

STOP
```

B Python scripts

This appendix displays the Python scripts used for the sediment transport models and computing the bed level changes based on the Exner equation

B.1. Sediment transport modeling

Listing B.1: Compuation of the critical Shields parameter in Python

```python
import numpy as np

def theta_c(D50, nu=1.05e-6, s=2.65, g=9.81):
    """
    Computes the critical Shields parameter θ(_c) for the initiation of sediment motion.

    Based on the —SoulsbyWhitehouse (1997) formula, which gives a smooth fit across a wide range
    of grain sizes via the dimensionless grain size D_*.

    Parameters:
        D50 : float or array-like
            Median sediment grain diameter (m).
        nu : float
            Kinematic viscosity of water (m²/s, default = 1.05e-6).
        s : float
            Relative density of sediment: s = ρ_s / ρ_w (default = 2.65).
        g : float
            Gravitational acceleration (m/s², default = 9.81).

    Returns:
        theta_cr : float or array-like
            Critical Shields parameter.
    """
    # Compute dimensionless grain size D_*
    D_star = (g * (s - 1) / nu**2)**(1/3) * D50

    # Empirical formula for critical Shields parameter
    theta_cr = 0.3 / (1 + 1.2 * D_star) + 0.055 * (1 - np.exp(-0.02 * D_star))

    return theta_cr
```

Listing B.2: Meyer-Peter-Müller (1948) sediment transport formula in Python

```python
import numpy as np

def mpm(taubx, tauby, D50=0.0002, A2=8, rho_s=2650, rho_w=1025, g=9.81):
    """
    Computes sediment transport rate using the basic Meyer-Peter-Müller (MPM) formulation.

    Parameters:
        taubx, tauby : array-like
            Bed shear stress components in x and y directions. Shape: [t, y, x]
        D50 : float
            Median grain diameter (m).
        A2 : float
            Empirical coefficient for transport intensity.
        rho_s : float
            Sediment density (kg/m³).
        rho_w : float
            Water density (kg/m³).
        g : float
            Gravitational acceleration (m/s²).

    Returns:
        Phi_x, Phi_y : array-like
            Sediment transport fluxes in x and y directions. Shape: [t, y, x]
    """
    # Compute critical Shields parameter
    theta_cr = theta_c(D50)

    # Stack the bed shear stress vectors: shape [t, 2, y, x]
    taub_vector = np.stack([taubx, tauby], axis=1)

```

```python
    # Compute Shields parameter vector: θ = τ / ρ[(_s - ρ_w) * g * D50]
    shields = taub_vector / ((rho_s - rho_w) * g * D50)  # shape: [t, 2, y, x]

    # Magnitude of Shields parameter: θ||||
    shields_mag = np.linalg.norm(shields, axis=1)  # shape: [t, y, x]

    # Compute unit vector in transport direction (avoid division by zero)
    direction_unit = np.divide(
        shields,
        shields_mag[:, np.newaxis],
        where=shields_mag[:, np.newaxis] != 0
    )

    # Transport intensity: only where Shields > critical Shields
    transport_intensity = shields_mag**0.5 * np.maximum(shields_mag - theta_cr, 0)

    # Flux vectors: intensity * direction, scaled by empirical A2
    flux_vectors = A2 * transport_intensity[:, np.newaxis] * direction_unit  # shape: [t, 2, y, x]

    # Split into components
    Phi_x = flux_vectors[:, 0]
    Phi_y = flux_vectors[:, 1]

    return Phi_x, Phi_y
```

Listing B.3: Soulsby (1997) sediment transport formula in Python

```python
import numpy as np

def mpm_soulsby(tau_cx, tau_cy, tau_wx, tau_wy, A2=8, d=0.001, rho_w=1025, rho_s=2650, g=9.81):
    """
    Computes sediment transport rates Φ(_x and Φ_y) using the Soulsby (1997) transport formulation,
    incorporating the effect of combined current and waves.

    Parameters:
        tau_cx, tau_cy : float or array-like
            Current-induced shear stresses in x and y directions.
        tau_wx, tau_wy : float or array-like
            Wave-induced shear stresses in x and y directions.
        A2 : float
            Empirical coefficient for transport formula.
        d : float
            Sediment grain diameter (m).
        rho_w : float
            Water density (kg/m³).
        rho_s : float
            Sediment density (kg/m³).
        g : float
            Gravitational acceleration (m/s²).

    Returns:
        Phi_X, Phi_Y : float or array-like
            Sediment transport rates in x and y directions.
    """
    theta_cr = theta_c(d)  # critical Shields parameter
    s = rho_s / rho_w      # relative density

    # Compute angle of current direction
    angle_current = np.arctan2(tau_cy, tau_cx)

    # Compute magnitudes of shear stress vectors
    tau_c = np.hypot(tau_cx, tau_cy)
    tau_w = np.hypot(tau_wx, tau_wy)

    # Compute angle between current and wave vectors
    dot_product = tau_cx * tau_wx + tau_cy * tau_wy
    cos_phi = dot_product / (tau_c * tau_w + 1e-12)  # avoid division by zero
    cos_phi = np.clip(cos_phi, -1.0, 1.0)
    phi = np.arccos(cos_phi)  # radians

    # Mean shear stress combining current and wave components
    tau_m = tau_c * (1 + 1.2 * (tau_w / (tau_c + tau_w))**3.2)

    # Compute Shields parameters
    factor = g * rho_w * (s - 1) * d
    theta_m = tau_m / factor
    theta_w = np.maximum(tau_w / factor, 0)  # ensure non-negative

    # Combined Shields parameter
    theta_max = np.sqrt((theta_m + theta_w * np.cos(phi))**2 + (theta_w * np.sin(phi))**2)

    # Two alternative formulations for Φ_x
    Phi_x1 = A2 * theta_m**0.5 * (theta_m - theta_cr)
```

```python
    Phi_x2 = A2 * (0.9543 + 0.1907 * np.cos(2 * phi)) * theta_w**0.5 * theta_m

    # Select the larger Φ_x component
    use_x1 = Phi_x1 >= Phi_x2
    Phi_x = np.where(use_x1, Phi_x1, Phi_x2)

    # Cross-shore transport component Φ_y (always same formulation)
    Phi_y = A2 * (0.1907 * theta_m * theta_w**2 * np.sin(2 * phi)) / (
        theta_w**1.5 + 1.5 * theta_m**1.5
    )

    # Apply threshold: transport only if θ_max > θ_cr
    mask = theta_max > theta_cr
    Phi_x *= mask
    Phi_y *= mask

    # Rotate back to global coordinate system
    Phi_X = Phi_x * np.cos(angle_current) - Phi_y * np.sin(angle_current)
    Phi_Y = Phi_x * np.sin(angle_current) + Phi_y * np.cos(angle_current)

    return Phi_X, Phi_Y
```

B.2. Bed updating

Listing B.4: Exner-type equation for computing bed level changes

```python
import numpy as np

def compute_exner_2d(q_sx, q_sy, dx, dy, porosity=0.4):
    """
    Compute the bed level change rate ∂z_b∂/t using the 2D Exner equation.

    Parameters:
    -----------
    q_sx : 2D np.ndarray
        Time-averaged sediment transport in x-direction [m²/s]
    q_sy : 2D np.ndarray
        Time-averaged sediment transport in y-direction [m²/s]
    dx : float
        Grid spacing in x-direction [m]
    dy : float
        Grid spacing in y-direction [m]
    porosity : float
        Bed porosity (default 0.4)

    Returns:
    --------
    dzb_dt : 2D np.ndarray
        Rate of bed level change [m/s]
    """

    if q_sx.shape != q_sy.shape:
        raise ValueError("q_sx and q_sy must have the same shape")

    # Compute divergence of sediment flux
    dqsdx = np.gradient(q_sx, dx, axis=1)
    dqsdy = np.gradient(q_sy, dy, axis=0)
    div_qs = dqsdx + dqsdy

    # Apply Exner equation
    dzb_dt = -div_qs / (1 - porosity)

    return dzb_dt
```

B.3. Wave nonlinearity

Listing B.5: Compuation of wave skewness and asymmetry (Ruessink et al., 2012)

```python
import numpy as np
from scipy.optimize import root_scalar

def b_from_r(r):
    return r / (1 + np.sqrt(1 - r**2))

def B_from_r(r):
    b = b_from_r(r)
    return 3 * b / np.sqrt(2 * (1 - b**2))

def solve_r_from_B(B_target):
```

```python
    def eq(r):
        if r <= 0 or r >= 1:
            return np.inf
        return B_from_r(r) - B_target

    result = root_scalar(eq, bracket=[1e-6, 0.999], method='brentq')
    if result.converged:
        return result.root
    else:
        raise ValueError("Root-finding did not converge.")

def compute_skewness(Ur, p1=0, p2=0.857, p3=-0.471, p4=0.297, p5=0.815, p6=0.672):
    """
    Compute wave skewness (Sk), asymmetry (As), skewness parameter r, and phase ψ from Ursell number.
    Optionally uses inverse formulation to compute r from B.

    Parameters:
        Ur : Ursell number (scalar or array)

    Returns:
        Sk  : Skewness [-]
        As  : Asymmetry [-]
        r   : Skewness parameter [-]
        psi : Phase angle [rad]
    """
    Ur_safe = np.where(Ur <= 0, 1e-6, Ur)

    # Empirical Ruessink (2012) B and psi
    B = p1 + p2 / (1 + np.exp((p3 - np.log(Ur_safe)) / p4))
    psi = -np.deg2rad(90) + np.deg2rad(90) * np.tanh(p5 / Ur_safe**p6)

    Sk = B * np.cos(psi)
    As = B * np.sin(psi)

    # r from B using numerical inversion
    r = solve_r_from_B(B)
    phi = -psi - np.pi / 2

    return Sk, As, r, phi
```

Listing B.6: Computation of bed shear stress including wave skewness and asymmetry

```python
import numpy as np

def mpm_soulsby_skewed(
    tau_mx, tau_my, Uw_x, Uw_y, fw, d=0.001, rho_w=1025, rho_s=2650, g=9.81, A2=12
):
    """
    Compute bed load transport using skewed wave orbital velocities.

    Inputs:
        tau_mx, tau_my: mean current shear stress [N/m^2]
        Uw_x, Uw_y: skewed wave orbital velocity components, shape (nt, ny, nx)
        fw: wave friction factor (scalar or 2D)
        d: grain size [m]
        A2: MPM empirical constant
    Returns:
        Phi_x, Phi_y: dimensionless bed load transport fluxes
    """
    nt = Uw_x.shape[0]
    dt = 1.0 / nt  # assume t spans [0, 1] over one wave cycle

    s = rho_s / rho_w
    theta_cr = theta_c(d)  # your critical Shields parameter function

    # Prepare arrays
    integrand_x = np.zeros_like(tau_mx)
    integrand_y = np.zeros_like(tau_my)

    for i in range(nt):
        # Instantaneous wave shear stress
        Uw_mag = np.sqrt(Uw_x[i]**2 + Uw_y[i]**2)  # |Uw|
        tau_wx = 0.5 * rho_w * fw * Uw_mag * Uw_x[i]
        tau_wy = 0.5 * rho_w * fw * Uw_mag * Uw_y[i]

        # Total instantaneous shear stress
        tau_x = tau_mx + tau_wx
        tau_y = tau_my + tau_wy

        # Instantaneous Shields stress
        theta_x = tau_x / (rho_w * g * (s - 1) * d)
        theta_y = tau_y / (rho_w * g * (s - 1) * d)
        theta = np.sqrt(theta_x**2 + theta_y**2)
```

```
        theta_safe = np.where(theta == 0, 1e-12, theta)

        # Bed load transport integrand
        mask = theta > theta_cr
        factor = np.where(mask, theta**0.5 * (theta - theta_cr), 0)
        integrand_x += factor * (theta_x / theta_safe) * dt
        integrand_y += factor * (theta_y / theta_safe) * dt

    Phi_x = A2 * integrand_x
    Phi_y = A2 * integrand_y

    return Phi_x, Phi_y
```

C Physical model

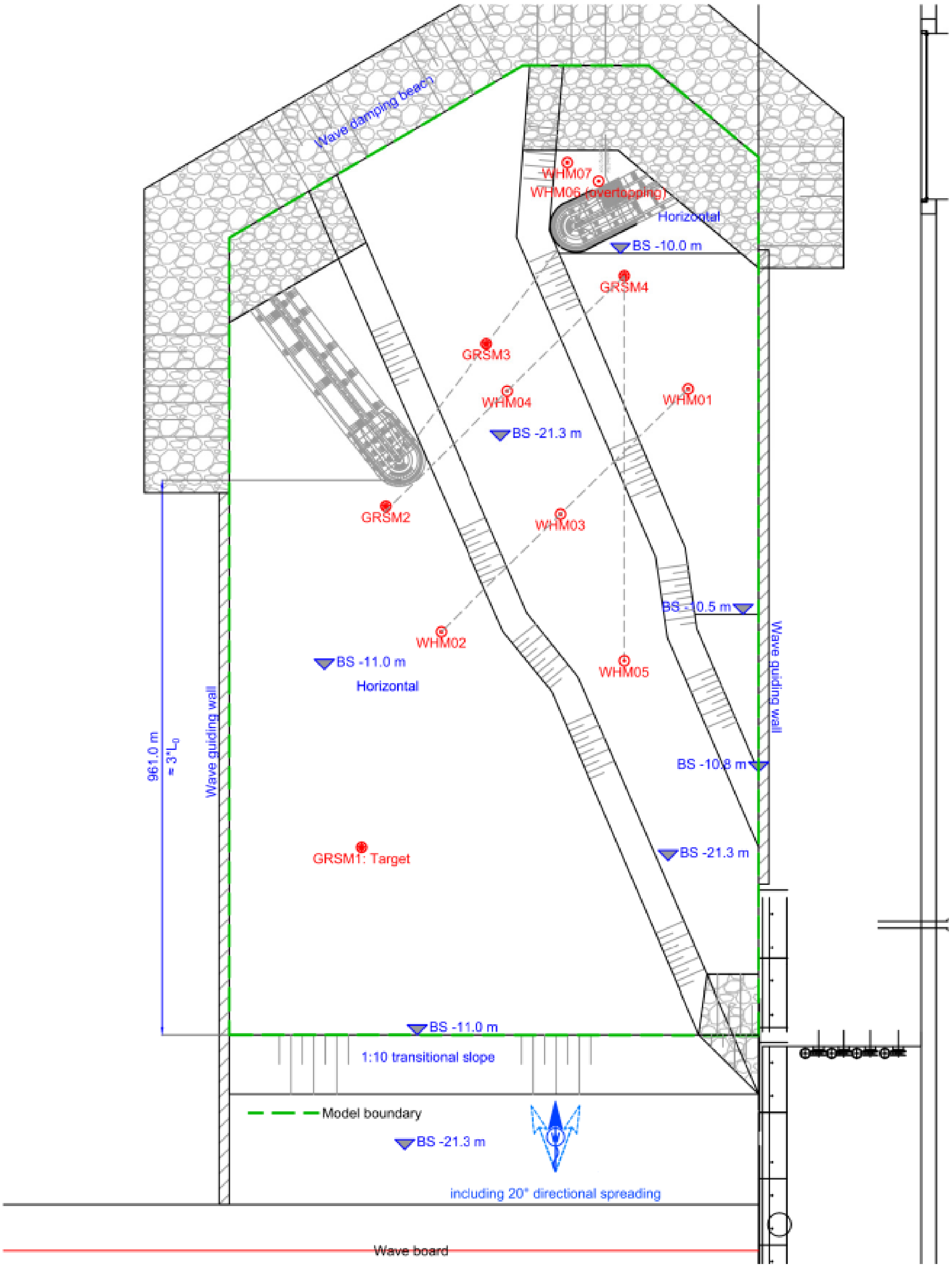

Figure C.1: Full-sized map of the physical model (Riezebos, 2014)

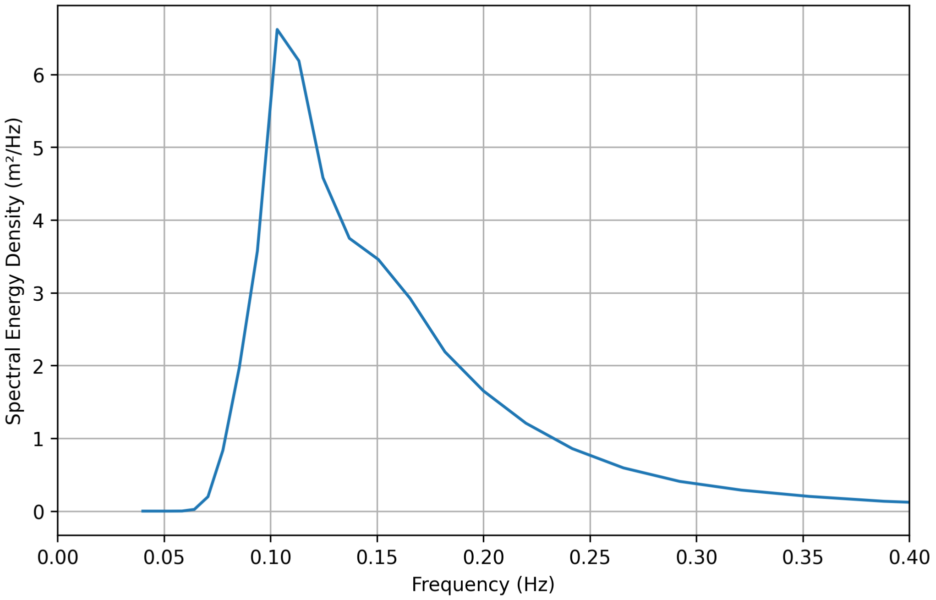

Figure C.2: 1D spectrum for T01

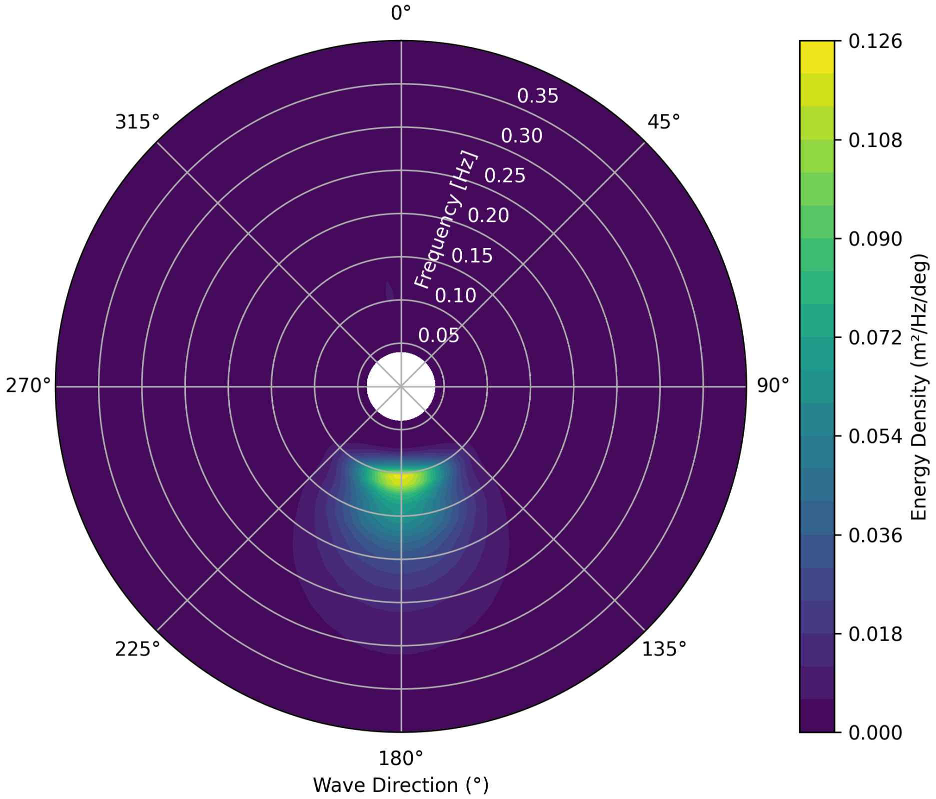

Figure C.3: 2D spectrum for T01

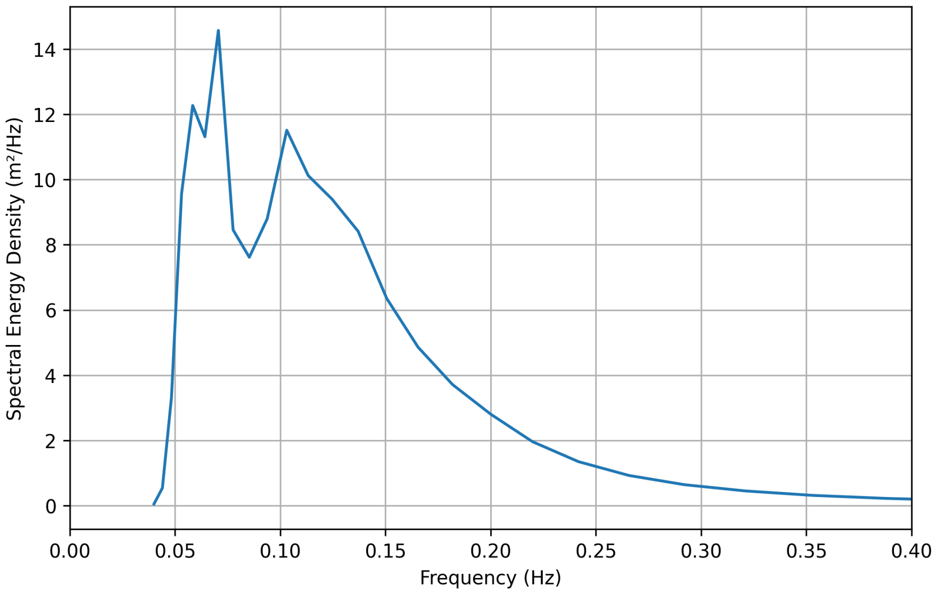

Figure C.4: 1D spectrum for T03

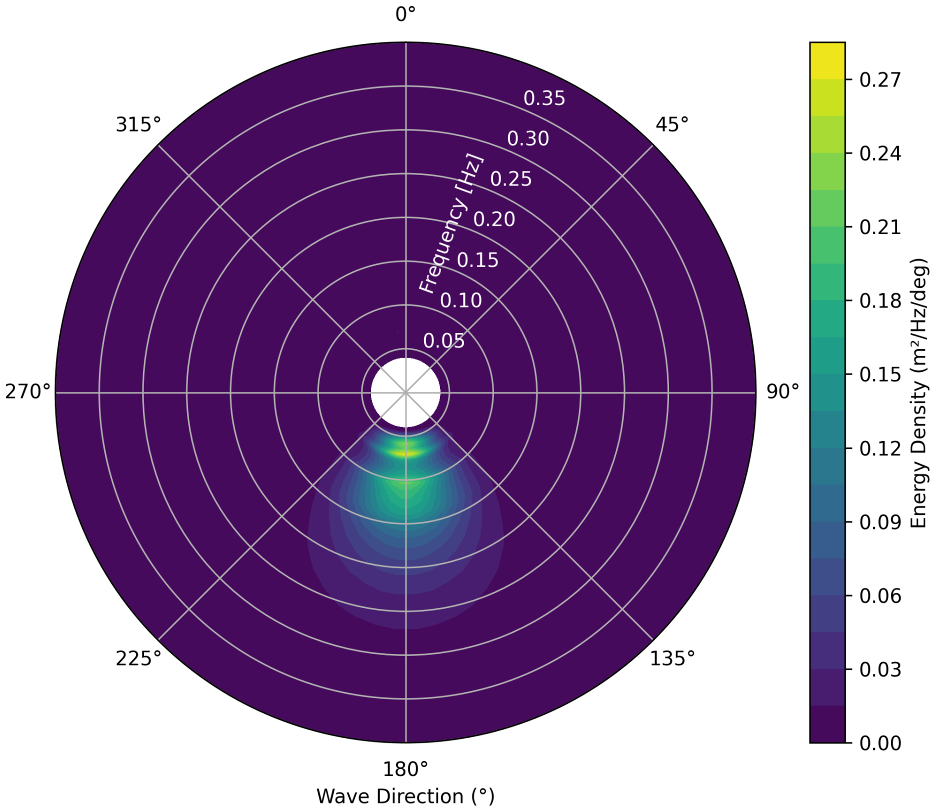

Figure C.5: 2D spectrum for T03

D Potential for inclusion of wave skewness and asymmetry in MPM SWAN-FINEL bed load

To account for the effects of non-linear wave transformation on bed load transport, the classical Soulsby–MPM transport framework was extended to include wave skewness and asymmetry in orbital velocity based on local wave shape parameters.

The addition of skewness and asymmetry is based on the idea of integrating the bed load transport computed with the Meyer-Peter and Müller (1948) formula over one wave cycle (Soulsby & Damgaard, 2005). However, instead of assuming a sinusoidal wave, the integral is taken of a nonlinear wave with skewness and asymmetry based on the wave form parameterization by Ruessink et al. (2012) and the representative near-bed velocity formula by Abreu et al. (2010).

D.1. Wave shape parametrization

The wave non-linearity was characterized using the Ursell number:

$$\mathsf{Ur} = \frac{3}{8}\frac{H_s k}{(kd)^3} \tag{D.1}$$

Where H_s is the significant wave height, k is the local wave number, and d is the water depth. From the Ursell number, the local wave skewness (S_u) and asymmetry (A_u) were obtained using an empirical parameterization based on Ruessink et al. (2012):

$$B = p_1 + \frac{p_2}{1 + \exp\left(\frac{p_3 - \ln(\mathsf{Ur})}{p_4}\right)} \tag{D.2}$$

$$\psi = -\frac{\pi}{2} - \frac{\pi}{2}\tanh\left(\frac{p_5}{\mathsf{Ur}^{p_6}}\right) \tag{D.3}$$

$$S_u = B\cos(\psi), \quad A_u = B\sin(\psi) \tag{D.4}$$

where B is a non-dimensional shape parameter and ψ is the phase shift governing the skewness–asymmetry relationship. The free parameters p_1 through p_6 follow values fitted by Ruessink et al. (2012).

The horizontal wave motion can be expressed with the following formula (Abreu et al., 2010):

$$u(t) = U_w f \frac{\sin(\omega t) + \frac{r\sin\phi}{1+f}}{1 - r\cos(\omega t + \phi)} \tag{D.5}$$

Where $f = \sqrt{1 - r^2}$. The skewness coefficient r used for the computation of the near-bed velocity can be related to B through:

$$B = \frac{3b}{\sqrt{2(1 - b^2)}}$$

$$b = \frac{r}{1 + \sqrt{1 - r^2}}$$

And ϕ is related to ψ with:

$$\phi = -\psi - \frac{\pi}{2}$$

ϕ and r can be computed with a numerical routine (listing B.5).

Figure D.1 displays the result of applying the wave shape parametrization by Abreu et al. (2010) and Ruessink et al. (2012) to the results from Chapter 5. The normalized velocity $(u(\omega t)/U_w)$ is plotted in four different locations at the transect of y=500 over one wave period. Moving onshore, the wave is becoming more skewed and asymmetric.

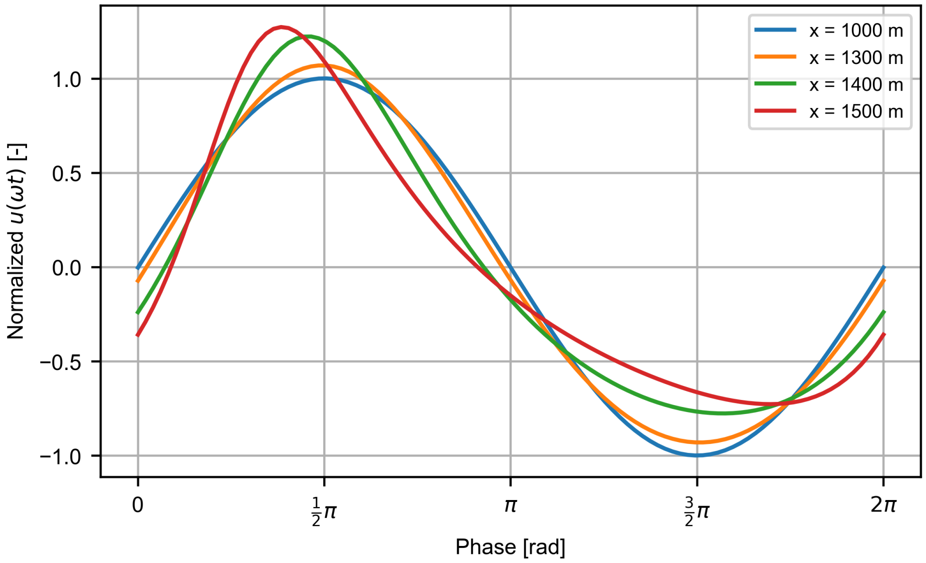

Figure D.1: Normalized near-bed velocity of one wave phase in different locations at y=500. Skewness and asymmetry are included with the waveform parametrization by Ruessink et al. (2012).

D.2. Modified bed load model

From the near-bottom velocity time series, the time-varying representative bed shear stress and Shield's parameter can be computed:

$$\tau_w(t) = \frac{1}{2} f_w \rho |u(t)| u(t) \tag{D.6}$$

$$\theta_w(t) = \frac{\tau_w(t)}{(\rho_s - \rho) g D_{50}} \tag{D.7}$$

Where f_w is the skin friction under waves, assumed independent of time, computed with the formulation of Swart (1974). The time-averaged bed load flux can then be computed with the following integral (Soulsby & Damgaard, 2005):

$$\langle \vec{\Phi} \rangle = \frac{A_2}{2\pi} \int_0^{2\pi} \theta^{1/2} (\theta - \theta_{cr}) \frac{\vec{\theta}}{\theta} d(\omega t) \tag{D.8}$$

Where θ is a time series of the bed shear stress of one representative wave phase $\theta(\omega t)$ as computed in Equation (D.7). Equation (D.8) can be evaluated numerically (listing B.6).

D.3. Effect on bed load transport

This extension of the model was applied to the results from Chapter 5, and a comparison between the original results, the results with the inclusion of this skewness and asymmetry parametrization, and the XBeach results is displayed in Figures D.2 to D.6.

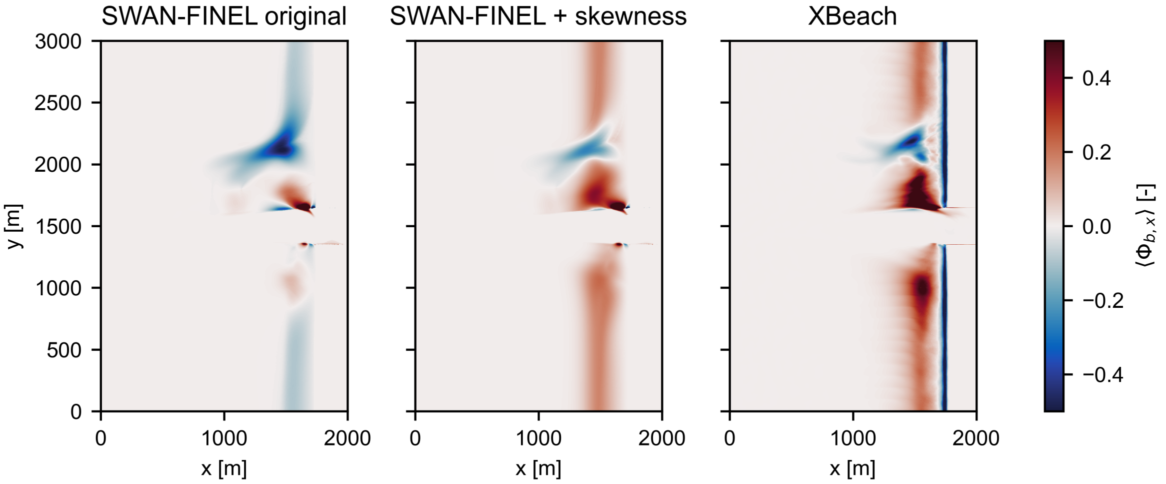

Figure D.2: Spatial distribution of the dimensionless bed-load sediment flux in the x-direction ($\Phi_{b,x}$), comparing: (1) The SWAN-FINEL results from the original sediment transport model in Chapter 5, (2) The SWAN-FINEL results with the nonlinear wave extension, (3) The XBeach non-hydrostatic results from Chapter 5.

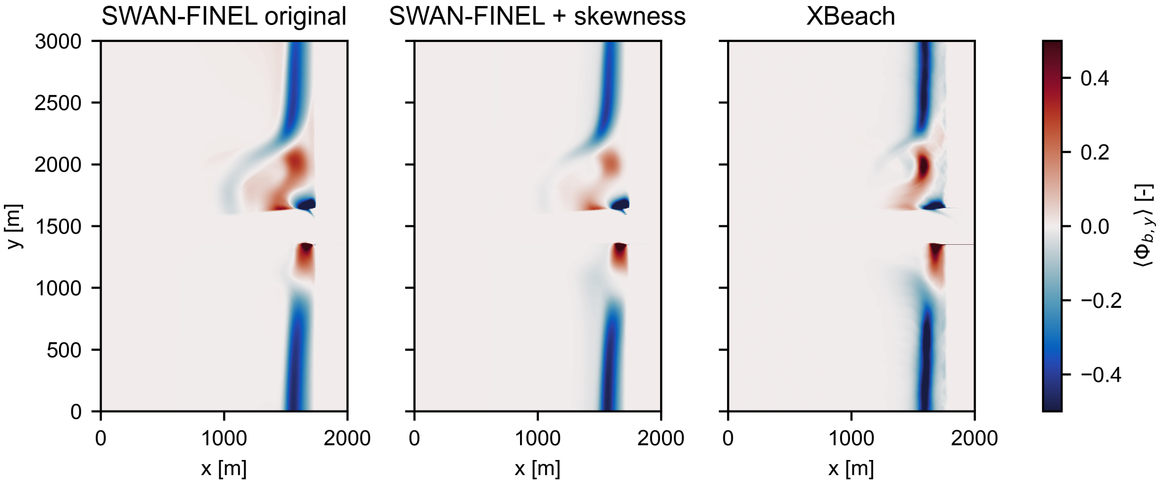

Figure D.3: Spatial distribution of the dimensionless bed-load sediment flux in the y-direction ($\Phi_{b,y}$), comparing: (1) The SWAN-FINEL results from the original sediment transport model in Chapter 5, (2) The SWAN-FINEL results with the nonlinear wave extension, (3) The XBeach non-hydrostatic results from Chapter 5.

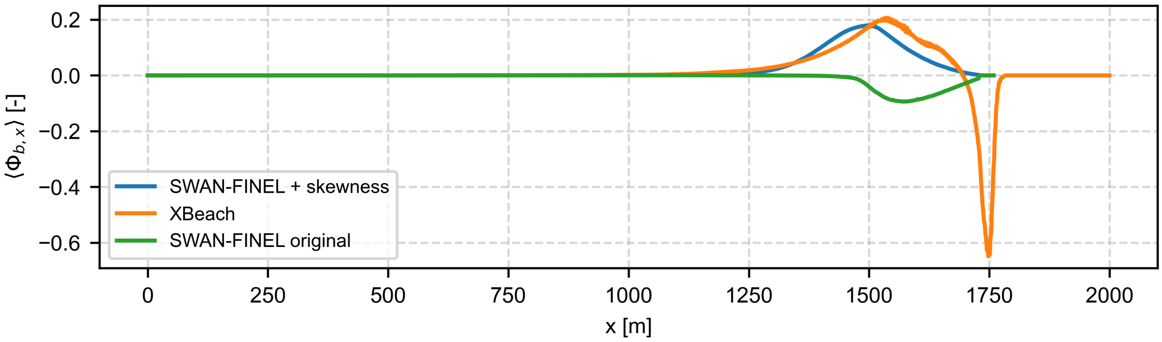

Figure D.4: Cross-shore transect of the dimensionless sediment bed-load flux $\Phi_{b,x}$ at $y = 500$ m, comparing: (1) The SWAN-FINEL results with the nonlinear wave extension, (2) The XBeach non-hydrostatic results from Chapter 5, (3) The SWAN-FINEL results from the original sediment transport model in Chapter 5.

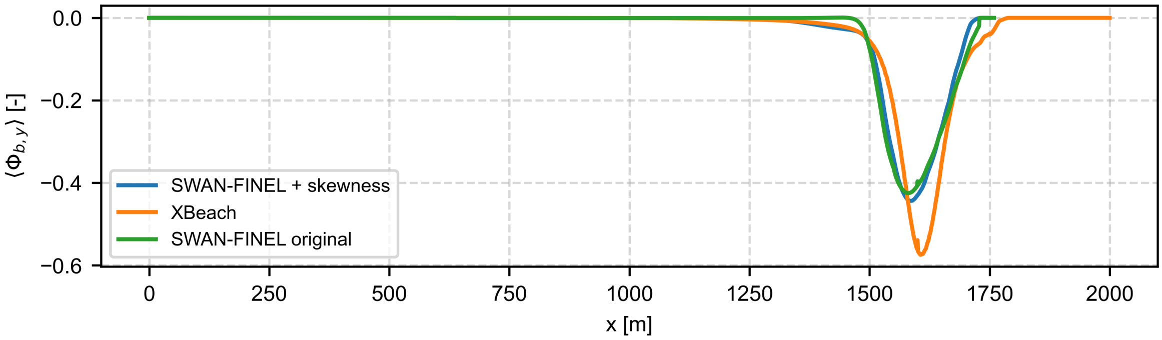

Figure D.5: Cross-shore transect of the dimensionless sediment bed-load flux $\Phi_{b,y}$ at $y = 500$ m, comparing: (1) The SWAN-FINEL results with the nonlinear wave extension, (2) The XBeach non-hydrostatic results from Chapter 5, (3) The SWAN-FINEL results from the original sediment transport model in Chapter 5.

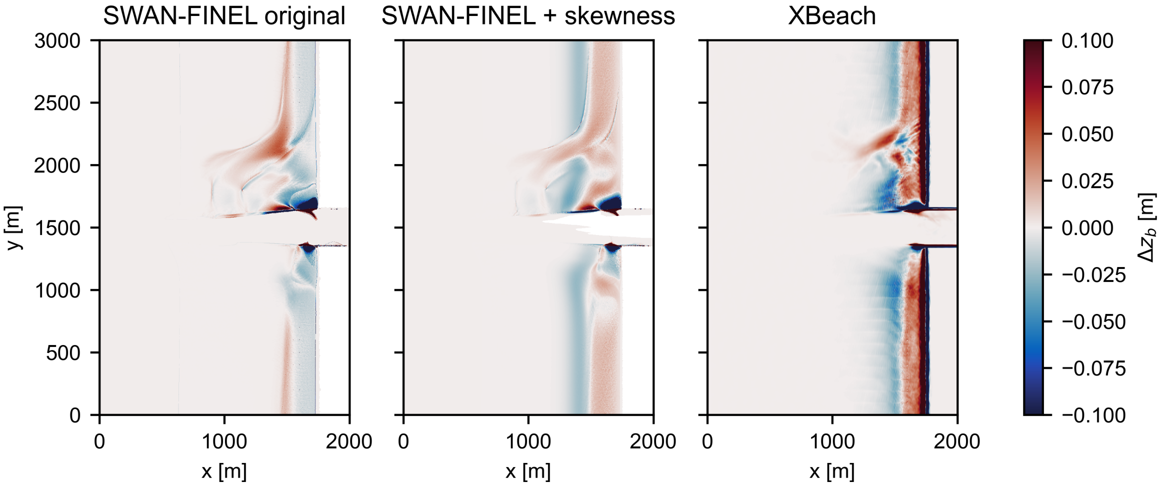

Figure D.6: Initial bed level change Δz_b after one day based on sediment flux gradients, comparing: (1) The SWAN-FINEL results from the original sediment transport model in Chapter 5, (2) The SWAN-FINEL results with the nonlinear wave extension, (3) The XBeach non-hydrostatic results from Chapter 5.

E Taman: additional tables

See in Tables E.1 and E.2 the comparison between the observed and modeled T_p in the Taman case.

Point	**Physical Model**	**SWAN**		**XBeach**	
	T_p [s]	T_p [s]		T_p [s]	
GRSM1	9.72	9.70	(0%)	9.14	(-6%)
GRSM2	9.14	9.70	(+6%)	9.14	(0%)
GRSM3	9.72	8.83	(-9%)	8.00	(-18%)
GRSM4	10.36	9.70	(-6%)	8.53	(-18%)
WHM01	10.36	9.70	(-6%)	9.85	(-5%)
WHM02	9.72	9.70	(0%)	9.14	(-6%)
WHM03	9.14	9.70	(+6%)	9.14	(0%)
WHM04	9.14	9.70	(+6%)	8.53	(-7%)
WHM05	6.76	8.83	(+31%)	9.14	(+35%)
WHM07	9.14	9.70	(+6%)	8.53	(-7%)
RMSE	–	**0.85**		**1.17**	

Table E.1: T01: Comparison of peak period T_p between the physical model, SWAN, and XBeach.

Point	**Physical Model**	**SWAN**		**XBeach**	
	T_p [s]	T_p [s]		T_p [s]	
GRSM1	14.12	14.16	(+0%)	14.22	(+1%)
GRSM2	14.12	14.16	(+0%)	14.22	(+1%)
GRSM3	9.72	14.16	(+46%)	14.22	(+46%)
GRSM4	17.27	14.16	(-18%)	14.22	(-18%)
WHM01	15.55	14.16	(-9%)	14.22	(-9%)
WHM02	15.55	14.16	(-9%)	14.22	(-9%)
WHM03	15.55	14.16	(-9%)	14.22	(-9%)
WHM04	15.55	14.16	(-9%)	14.22	(-9%)
WHM05	9.14	14.16	(+55%)	9.85	(+8%)
WHM07	9.14	14.16	(+55%)	14.22	(+56%)
RMSE	–	**2.96**		**2.51**	

Table E.2: T03: Comparison of peak wave period T_p between the physical model, SWAN, and XBeach.

F Synthetic case: additional plots and tables

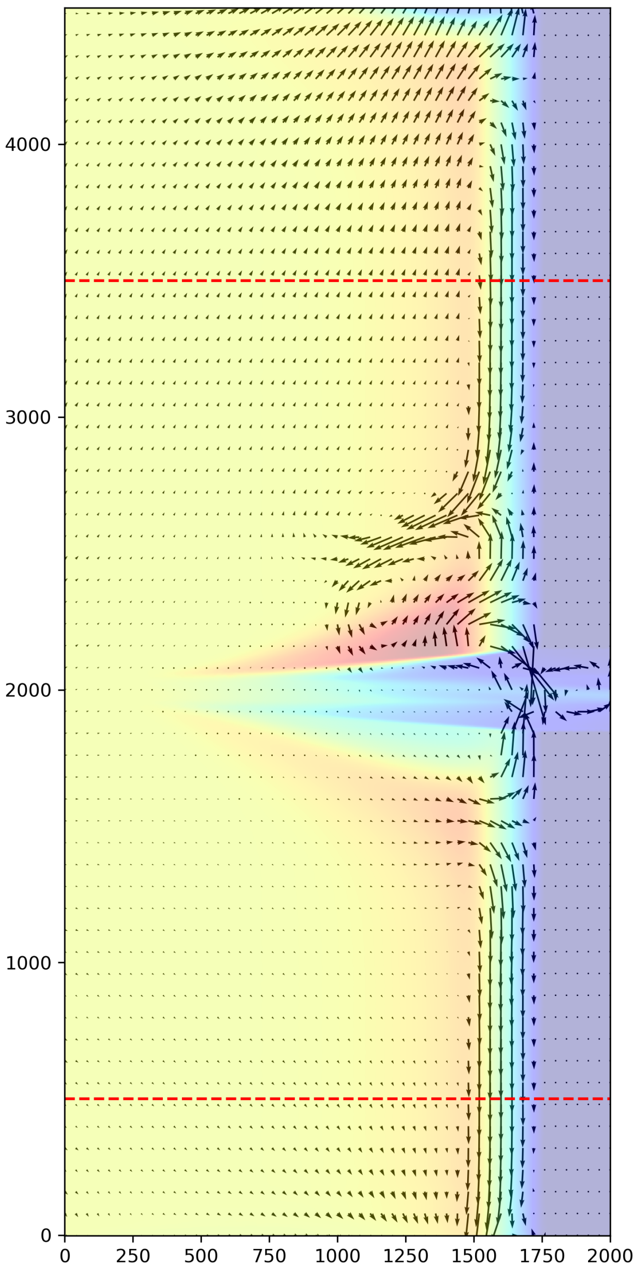

Figure F.1: Plot of flow velocities from FINEL within the complete model domain. Waves are imposed on the northern boundary up to x=1000 m. This causes a current to exist near the northern domain towards the north.